AD-A130 659 AXIAL COMPRESSOR MIDDLE STAGE SECONDARY FLOW STUDY(U) 1/2
UNITED TECHNOLOGIES RESEARCH CENTER EAST HARTFORD CT
J H WAGNER ET AL. JUL 83 NASA-CR-3701 NAS3-23157

UNCLASSIFIED F/G 21/5 NL

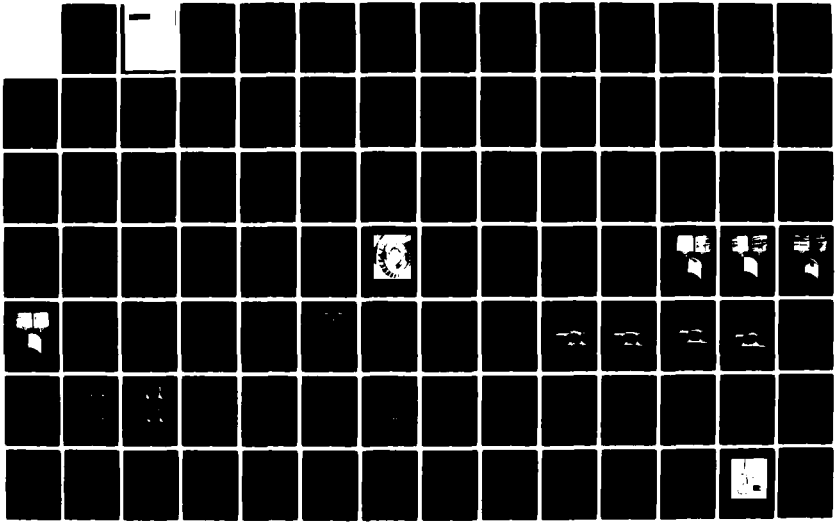

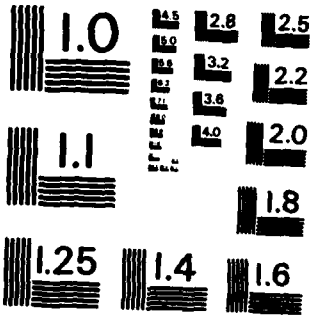

MICROCOPY RESOLUTION TEST CHART
NATIONAL BUREAU OF STANDARDS-1963-A

AD A130659

NASA Contractor Report 3701

Axial Compressor Middle Stage Secondary Flow Study

Joel H. Wagner, Robert P. Dring,
and H. David Joslyn
United Technologies Research Center
East Hartford, Connecticut

Accession For
NTIS GRA&I ☑
DTIC TAB ☐
Unannounced ☐
Justification
Distribution/
Availability Codes
Dist | Avail and/or Special
A

DTIC COPY INSPECTED

Prepared for
U.S. Army Research & Technology Laboratories
(AVRADCOM), Propulsion Laboratory
and NASA Lewis Research Center
under Contract NAS3-23157

National Aeronautics
and Space Administration

Scientific and Technical
Information Branch

1983

This document has been approved for public release and sale; its distribution is unlimited.

CONTENTS

	Page
SUMMARY	1
INTRODUCTION	3
LIST OF SYMBOLS	5
PRESENT STUDY	7
Objectives	7
Approach	7
EXPERIMENTAL FACILITY	9
BACKGROUND	12
Data Presentation	12
Magnetic tape data format	12
Data summary format	12
Data comparison	12
Inlet Documentation	13
Velocity profiles	13
Trace gas concentration profiles	13
RESULTS AND DISCUSSION	14
Rotor Performance	14
Surface Flow Visualization	14
Aerodynamic Traverse Results	16
Total and static pressures	16
Flow field velocities	18
Pitch averaged results	19
Airfoil Pressure Distributions	23
Midspan pressure distributions	23
Fullspan pressure distributions	24
Airfoil pressure force	25
Trace Gas Traverse Results	25
Concentration contours	25
Pitch averaged results	27
SUMMARY OF RESULTS	28

CONTENTS
(Continued)

	Page
CONCLUSIONS	30
APPENDIX A - 5-HOLE/COBRA PROBE CALIBRATION	31
APPENDIX B - MAGNETIC TAPE DATA FORMAT	33
REFERENCES	35
TABLE I - ROTOR AIRFOIL GEOMETRY	37
FIGURES	38

AXIAL COMPRESSOR MIDDLE STAGE SECONDARY FLOW STUDY

By
Joel H. Wagner
Robert P. Dring
H. David Joslyn

SUMMARY

An experimental program was performed in the United Technologies Research Center's Large Scale Rotating Rig (LSRR2) to provide a set of detailed middle stage axial compressor rotor data for the purpose of understanding the effects of secondary flow and how this understanding may be applied to engine design. This resulted in the acquisition of pneumatic probe and surface static pressure data in addition to surface flow visualization and trace gas concentration traverse data to precisely determine the nature of the rotor passage and exit plane secondary flow effects.

The present program was complementary to a previous benchmark study to obtain detailed flow field measurements within and behind an isolated compressor rotor which had been conducted earlier at the United Technologies Research Center under contract to the Air Force (Contract No. F33615-77-C-2083). The test rotor was typical of a mid-compressor rotor and the test conditions were varied over a wide range of blade loading (incidence). This previous program had relatively thin inlet boundary layers on the annulus hub and tip.

The objective of the present study was to extend this earlier work by investigating the three-dimensional flow field for the same rotor but with much thicker hub and tip inlet boundary layers. The approach was to use the existing well-documented isolated rotor model and to operate this rotor at identical average inlet flow coefficients, with thick hub and tip inlet boundary layers typical of the inlet to a middle stage rotor. By repeating pneumatic and flow visualization tests, differences in the secondary flow phenomena between an imbedded rotor and an isolated rotor could be determined. Additional information about radial redistribution or displacement of rotor passage flow was obtained from trace gas results.

The airfoil chord was 6 in. (0.15 m) and was constant with span. This resulted in an airfoil aspect ratio of 1.0 and a Reynolds number range (based on the average inlet flow speed) of 4.3×10^5 to 5.0×10^5. Boundary layer profiles which extended to approximately 37 percent of the rotor span from the

hub and tip were generated by a boundary layer thickening device installed upstream of the rotor. In addition to the boundary layer thickening device, three annular rings for trace gas injection were installed in the flowpath. Surface flow visualization and fullspan surface pressure measurements were made on the rotor airfoil and fullspan surveys of the velocity and pressure fields aft of the rotor were obtained.

The results were analyzed and compared with those of the previous program with thin inlet boundary layers and with a potential flow calculation. It was determined from the results that the relative unloading of the midspan region of the airfoil (due to the thicker endwall boundary layers) inhibited a fullspan separation at high loading, preventing high loss fluid in the hub corner stall from being centrifuged to the tip region. Radial redistribution of high and low total pressure fluid influenced the magnitude of the spanwise distribution of loss such that there was a general decrease in loss near the hub to the extent that for the least loaded case a negative loss (increase in total pressure) was observed. The ability to determine the spanwise distribution of blockage was demonstrated. In general, there was large blockage in the endwall regions due to the hub corner stall and tip leakage and little blockage in the core flow. Hub blockage was found to increase rapidly with loading.

INTRODUCTION

Many of the complex flow phenomena that occur within and behind the axial compressor rotating blade rows are not fully understood at the present time. One major factor that contributes to the complexity of the highly three-dimensional flow field is the existence of thick boundary layers on the hub and tip of the annulus. Under some situations, such as the inlet stages of a multistage compressor, the annulus boundary layer represents only a small fraction of the total incoming flow field. However, as that fraction increases to the point where the boundary layer represents a major portion of the flow field, as is the case with middle and exit stage groups, there is a major impact due to the effects of the three-dimensional flows that are generated.

The importance of these three-dimensional flows from a design viewpoint is inherently related to the through-flow analysis of multistage design. An understanding of the mechanisms is necessary in order to predict the losses through blade rows generated by tip leakage flows, flow passage vortices, and endwall boundary layer phenomena.

A large amount of data has been obtained from cascade studies of these effects. Secondary flow effects in compressor cascades resulting from tip leakage and inlet skewing have been studied, for example, by Lakshminarayana and Horlock (Ref. 1) and by Moore and Richardson (Ref. 2), respectively. Three-dimensional flow in a turbine cascade was studied by Langston, et al. (Ref. 3) and also its effect on surface heat transfer by Graziani, et al. (Ref. 4). Cascade studies have included measurement of three-dimensional secondary flow effects as well as flow visualization results. More recently, detailed studies have also been done in rotating test rigs. Tip leakage flow visualization results were obtained in an axial flow compressor by Phillips and Head (Ref. 5). High response measurements downstream of axial compressor blade rows have been performed by many noted investigators including Schmidt and Okiishi (Ref. 6), Reynolds and Lakshminaraya (Ref. 7) and Kool et al. (Ref. 8). High response relative and absolute frame surface pressure and velocity data has also been obtained in a turbine test rig by Dring, et al. (Ref. 9). Adkins and Smith (Ref. 10) have presented an approximate method for inclusion of the secondary flow effects of endwall boundary layers, tip clearance, shrouding, airfoil surface boundary layers, and wake transport in a compressor through-flow analysis. Their predictions of the radial distributions of various flow parameters and loss agree quite well with many investigators' results. Even with this large body of data, the need for determining the cause and effect of endwall and secondary flow still exists. Evidence of this need can be seen in the long and costly development process most new compressor designs require in order to attain their design objectives of flow, pressure rise, and efficiency.

The methodology most desirable to gain this better understanding is to use a similar facility for all testing thus accumulating an extensive, directly comparable body of results for detailed analysis. A benchmark study to obtain detailed flow measurements within and behind an isolated mid-compressor type rotor has already been conducted at the United Technologies Research Center (Ref. 11) which was based on data taken under contract to the Air Force (Contract No. F33615-77-C-2083, Ref. 12). The test rotor was typical of a mid-compressor rotor and the test conditions were varied over a wide range of blade loading (incidence) with relatively thin inlet boundary layers on the annulus hub and tip. The objectives of this study were to document the effects of blade loading on the generation of the detailed three-dimensional flow field in the rotor blade-to-blade passage and in the flow downstream of the rotor, and to compare the results with various analytical predictions.

The objective of the present study was to extend this earlier work by investigating the three-dimensional flow field for the same rotor but with much thicker hub and tip inlet boundary layers. The bulk of the present data was acquired in the rotating frame of reference of the rotor. Surface flow visualization and fullspan surface pressure measurements were made on the rotor airfoil and fullspan surveys of the velocity and pressure fields aft of the rotor were obtained. The data was acquired over a range of rotor incidence and for inlet hub and tip boundary layer thicknesses typical of a middle stage rotor.

It was determined from the results that the relative unloading of the midspan region of the airfoil (due to the thicker endwall boundary layers) inhibited a fullspan separation at high loading preventing high loss fluid in the hub corner stall from being centrifuged to the tip region. Radial redistribution of high and low total pressure fluid influenced the magnitude of the spanwise distribution of loss, such that, there was a general decrease in loss near the hub to the extent that for the least loaded case a negative loss (increase in total pressure) was observed. Of specific interest to the through-flow analyst, the spanwise distributions of blockage were determined for the present results and for those of Ref. 11.

LIST OF SYMBOLS

Symbol

B	Airfoil true chord
B_x	Airfoil axial chord
C_p	Pressure coefficient: $(P_{T1} - P)/Q_{U_m}$
C	Absolute flow velocity
h_2/h_1	Contraction ratio
H	Boundary layer shape parameter
$\bar{K}$	Blockage
P	Pressure
P_{T1}	Inlet absolute total pressure
Q_{U_m}	Dynamic pressure based on midspan wheel speed: $\left(1/2\ \rho U_m^2\right)$
r	Radial position
t	Airfoil thickness
U_m	Wheel speed at midspan
V, W	Flow velocity in the rotating frame
X	Axial distance
θ^*	Airfoil metal angle (measured from axial)
δ^*	Boundary layer displacement thickness
θ	Boundary layer momentum thickness
Θ	Yaw (from axial direction, positive in direction of rotation)
ϕ	Pitch (positive away from rig axis)
ϕ	Flow coefficient: $\bar{C}_x/U_m$
ρ	Fluid density
ζ	Vorticity
ω	Rotational speed
τ	Pitch

Subscripts

m	Midspan

LIST OF SYMBOLS
(Continued)

r	Radial component (positive away from rig axis)
S	Static
T	Total
x	Axial component
θ	Tangential component (positive in direction of rotation)
1, 2	Station number

Superscripts

—a	Area average
—m	Mass average
—	Pitch average

PRESENT STUDY

Objectives

The objective of the present study was to provide a set of detailed middle stage axial compressor rotor data for the ultimate purpose of producing better compressors by reducing the time and cost of compressor development. This could be accomplished with a more refined initial design based on an improved physical understanding of the three-dimensional flow present in axial flow compressors. This objective was predicated upon the necessary acquisition of pneumatic probe and surface static pressure data in addition to surface flow visualization and trace gas concentration traverse data to precisely determine the nature of the rotor passage and exit plane secondary flow effects.

Approach

The approach was to use an existing well-documented isolated rotor model, which had been used in previous investigations with relatively thin inlet boundary layers, and to operate this rotor model, at identical average inlet flow coefficients, with thick hub and tip inlet boundary layers typical of the inlet to a middle stage rotor. By repeating pneumatic and flow visualization tests, differences in the secondary flow phenomena between an imbedded rotor and an isolated rotor could be determined. Additional information regarding radial redistribution or displacement of rotor passage flow could be obtained from the trace gas results. Therefore, to this end, the following program sections were completed.

(1) An axisymmetric boundary layer thickening and trace gas injection system was developed prior to the test. This consisted of designing and evaluating the performance of the boundary layer thickening screen and the trace gas injection and concentration measurement system.

(2) The final test configuration was documented in the United Technologies Research Center Large Scale Rotating Rig (LSRR2). The documentation consisted of measuring inlet velocity and trace gas concentration profiles at the expected test flow coefficients and at various circumferential locations.

(3) Rotor static pressure rise was documented for comparison to previous isolated rotor results.

(4) Flow visualization tests were performed in the rotor passage to observe airfoil and hub endwall surface secondary flow phenomena and ultimately to help assimilate the traverse results.

(5) Airfoil pressure distribution and flowpath endwall static pressure data were acquired for documentation and to help explain the blade-to-blade rotor passage secondary flow effects.

(6) Pneumatic traverse data consisting of exit plane relative frame flow field traverse data was acquired to completely define the rotor exit relative flow field by determining total and static pressure, flow speed, and direction.

(7) Trace gas concentration measurements were made for the hub, midspan, and tip injectors and for each flow coefficient for the purpose of determining the radial redistribution or displacement of the rotor passage flow by tracking the hub, midspan, and tip seeded stream surfaces.

(8) These results were analyzed and compared with those of a previous program with thin inlet boundary layers and with a potential flow calculation for the purpose of understanding the effects of secondary flow and how this understanding may be applied to engine design through improvements in the initial design process.

EXPERIMENTAL FACILITY

The experimental program was performed in the United Technologies Research Center's Large Scale Rotating Rig (LSRR2). The rotor is 5 ft (1.52 m) in diameter and is shown with the 0.8 hub/tip ratio isolated compressor rotor installed in Fig. 1. The rotating frame radial-circumferential traverse system and the traverse probe can also be seen. For the present program the rotor shaft speed was 510 rpm. The range of flow coefficient based on area averaged C_x ($\bar{\phi}$) was 0.65 to 0.95 which corresponds to an average axial flow velocity ($\bar{C}_x$) range of 78 ft/s (24 m/s) to 114 ft/s (35 m/s).

The airfoil true chord was 6 in. (0.15 m) and was constant with span. This resulted in an airfoil aspect ratio of 1.0 and a Reynolds number range (based on the average inlet flow speed) of 4.3×10^5 to 5.0×10^5. Details of the airfoil geometry are tabulated in Table I. Axial chord (B_x) at midspan was 5 in. (0.13 m). Rotor tip clearance varied from 2.3 percent span at the leading edge to 1.0 percent span at midchord to 3.3 percent span at the trailing edge (Fig. 2).

A cross-section of the flowpath is shown in Fig. 2. Upstream and downstream static pressures were measred at Sta. 1 and 3, respectively. The rig flow was based on the static pressure and midspan total pressure at Sta. 1. Documentation of inlet velocity and trace gas concentration profiles was also performed at Sta. 1. The difference between the midspan total pressure and static pressure (midspan inlet dynamic pressure) was corrected based on the hub and tip velocity profiles to obtain the area average inlet flow speed ($\bar{C}_x$). The rotor exit traverse plane was located at Sta. 2 which was a distance 30 percent of the axial chord aft of the rotor trailing edge at midspan. This particular traverse location was chosen because back flow (due to hub corner stall) was not present at this plane, as determined from the results of Ref. 11, but the strong effects of secondary flow were still present.

The traverse device located inside the rotor hub (Fig. 1) was used to position the two probes used in this program. Each probe could be traversed circumferentially over 25.7° (two rotor blade pitches) and radially from hub to tip. The probes could also be rotated in yaw over ± 90° from axial. The probe used for aerodynamic measurements was a five-hole probe which had been modified to include a cobra probe for acquiring data near the hub. The five-hole probe diameter was small relative to the blade pitch (1.5 percent of τ_m). The five-hole probe was used to measure total pressure, static pressure, flow yaw, and flow pitch angle from 12.5 percent to 97 percent span. The cobra probe was used to measure total pressure, static pressure, and yaw down to 5 percent span. A description of the probe calibration procedure and a set of typical calibration results are provided in Appendix A. Switching from the five-hole probe to the cobra probe, calibration of onboard transducers, and operation of the rotating

frame multiport scanning valve could all be carried out remotely while the rotor was turning. The trace gas sampling probe was a standard 0.125 in. (0.3 cm) kiel probe used to sample the flow for the trace gas concentration. Carbon dioxide (CO_2) was used as the trace gas. A NDIR gas analyzer with zero and span (2000 ppm) calibration gases was used to determine the trace gas (CO_2) concentration of the flow in parts per million (ppm). The analyzer was calibrated periodically with the calibration gases. Typical local maximum concentrations were approximately 0.1 percent with typical background concentration levels of 0.03 percent.

Two of the rotor airfoils were instrumented to acquire surface static pressures. Pressure taps were installed at alternating chordwise positions on each airfoil at locations from 2 percent to 90 percent chord and from 4 percent to 95 percent span. This permitted a complete mapping of the spanwise variation of pressure force on the rotor airfoil. The instrumented airfoils were also used for surface flow visualization using an ammonia/Ozalid technique developed by Ruden (Ref. 13) and demonstrated in Refs. 11, 14, and 15. The technique consists of attaching Ozalid paper to the surface of the airfoil and seeping a small amount of ammonia gas out of selected surface pressure taps. The ammonia produces a dark blue streak-line on the Ozalid paper showing the direction of the flow on the airfoil surface.

Boundary layer profiles which extended to approxiamtely 35 percent of the rotor span from the hub and tip were desired to effectively model the incoming flow of a middle stage rotor. To generate the thick boundary layer required for this program a boundary layer thickening device was installed upstream of Sta. 0 (see Fig. 2). The boundary layer profiles were created with a combination of screens of varying wire diameter and spacing designed and demonstrated in a small scale wind tunnel. The measured pretest developed profiles duplicated the design. The most upstream profile clearly showed a stepped behavior caused by the discrete differences in the screen porosity and the blockage of the trace gas injector, however, the remaining downstream profiles showed only minor variations with streamwise distances. The details of the screen geometry are as follows.

Span	Open Area (%)	Mesh (in.$^{-1}$)	Wire Diameter (in.)
0-10 and 90-100	50	16	0.015
10-20 and 80-90	80	3	0.035
20-30 and 70-80	90	2 1/2	0.020

In addition to the boundary layer thickening device, three annular rings for trace gas injection were installed in the flowpath. The hub and tip injection rings were located immediately downstream of the screen supports (see Fig. 2). The third ring was located approximately 2 ft upstream of Sta. 0 at the midspan

streamtube radius. Details of the injector geometry are as follows.

Tube Outside Diameter	0.375 in. (0.95 cm)
Injector Orifice Diameter	0.015 in. (0.04 cm)
Injector Orifice Spacing	1.00 in. (2.54 cm)

As expected, the measured pretest trace gas concentration profiles showed a marked difference in shape with streamwise distance due to mixing. Near the injector the absolute gas concentration was high and concentrated near the end-wall diffusing outward to only 20 percent span. As streamwise distance increased the high peak near the wall diminished and the profile assumed a more linear shape extending out to 35 percent span. During testing, each trace gas injector was used separately.

The rig was operated by a computerized automatic control, data acquisition, and data reduction system. The system precisely maintained the desired flow coefficient ($\bar{\phi}$) to within ± 1/2 percent, calibrated all the pressure transducers in the rotating and stationary frames, controlled probe radial-circumferential positioning, acquired all pneumatic data, and reduced this data (on-line) to engineering units and to convenient dimensionless parameters. The accuracy of the pressure measurement system was typically ± 2 percent or reading. Since all pressure measurements were referenced to the midspan absolute inlet total pressure the uncertainty is ± 2 percent of C_p. The yaw zero was determined in the rig while the rotor was stationary with an axially directed air jet. This technique insured consistent yaw angle results and was an improvement over the methods used in previous work which required a mechanical flag on the probe stem.

BACKGROUND

Data Presentation

Magnetic Tape Data Format - The magnitude of the amount of data as well as the ease of accessibility for other investigators warrants the systematic storage of all the traverse data, pneumatic as well as trace gas concentration, to be organized on magnetic tape. For this reason, only a summary of the results is presented in this report. All of the traverse data, however, is available (from either NASA/LeRC or UTRC) on magnetic tape with the tape format described in Appendix B.

Data Summary Format - The pneumatic data is presented in the form of dimensionless pressure coefficients, normalized velocity components and flow angles. Both the total and static pressures were referenced to the inlet absolute total pressure at midspan and the difference normalized by a dynamic pressure based on midspan wheel speed (QU_m). All of the velocity components were normalized with midspan sheel speed (U_m). Tangential velocity and yaw were taken as positive in the direction of rotor rotation (Fig. 2) and radial velocity and pitch were taken as positive in the radially outward direction. Circumferential location was increasing in the direction opposite to rotor rotation, i.e., from the pressure surface to the suction surface side of the wake (Fig. 2).

Cobra probe data presented in the spanwise distributions has been distinguished from the five-hole probe data by solid symbols compared to open symbols for five-hole data. The airfoil pressure distributions were presented in terms of a pressure coefficient based on the inlet relative total pressure and inlet relative dynamic pressure, both determined at the radius at which the airfoil pressure distributions were measured. Relative inlet total pressures and flow angles were determined from the average inlet axial velocity profile at Sta. 1. The total pressure contour plots are presented in terms of rotary total pressure which has the total pressure variation due to radial position (i.e., local wheel speed) removed.

The trace gas concentration data is presented as percent concentration between the local maximum concentration (~ 1000 ppm, 100%) and the background level (~ 300 ppm, 0%).

Data Comparison - Much of the data presented in this report has been compared with data taken previously on this rotor with thin inlet boundary layers (Ref. 11). Unless specified, results from Ref. 11 are presented as lines with the symbols representing data from the present program. Careful attention must be paid to the different methods of describing the test flow coefficients. For the present program the area average inlet axial velocity was used to

define the flow coefficient, whereas, the midspan velocity was used in the previous program (Ref. 11). The area average inlet normalized velocity ($\bar{C}/C_m$) for the present program was 0.84 while for the previous program (Ref. 11) it was 0.98 due to the relatively thin inlet boundary layers. Because the flow coefficient based on the midspan flow speed for the previous work is very close to the area average flow coefficient, the difference will not be distinguished during the discussion of the results.

Inlet Documentation

Velocity Profiles - The inlet velocity profiles were measured at Sta. 1 (Fig. 2) at three equally-spaced circumferential locations around the annulus for the four test flow coefficients ($\bar{\phi}$ = 0.65, 0.75, 0.85 and 0.95). The C_x profiles were essentially invariant with flow coefficient and had only small variations for the three circumferential locations. The standard deviation of the displacement and momentum thicknesses was typically 5 and 3 percent, respectively. The standard deviation of the shape factors was typically 2 percent. These deviations were almost entirely due to the nonaxisymmetry of the measured velocity profiles at the three circumferential locations. The average of the twelve inlet velocity profiles and integral parameters (displacement thickness, momentum thickness, and shape factor) are shown in Fig. 3. Symmetry about midspan is evident in the shape as well as in the integral results. This can be seen by the nearly identical values of integral thicknesses at the hub and tip. The displacement and momentum thicknesses were approximately 8 and 5 percent of the airfoil span and boundary layer thicknesses for both the hub and tip were approximately 37 percent of the span. This was a substantial increase in boundary layer thickness compared to the inlet conditions for the previous program (Ref. 11) where integral thicknesses were about 1 to 2 percent and boundary layer thicknesses were only 5 to 10 percent of the airfoil span. The average inlet C_x was 84 percent of the midspan flow and compared to 98 percent from the previous isolated rotor test. Shape factors presented (H = 1.47 to 1.50) are fairly typical of turbulent boundary layers.

Trace Gas Profiles - The inlet trace gas concentration profiles at the hub, midspan, and tip were also measured at Sta. 1 and are shown in Fig. 4. Each injector was operated separately. As with the inlet velocity profiles, gas concentration traverse data were acquired at three equally spaced circumferential locations for the four flow coefficients. As mentioned previously, gas concentration was presented as percent concentration above background, normalized with the maximum difference. The hub and tip concentration profiles extend to approximately 40 percent of the airfoil span which is close to the velocity boundary layer thickness. The midspan profile width extends over approximately 60 percent of the airfoil span with the majority of the high concentration gas in the core flow region between 30 and 70 percent span.

RESULTS AND DISCUSSION

Rotor Performance

The rotor static pressure rise characteristic is shown in Fig. 5. The static pressure rise from Sta. 1 to Sta. 3 has been normalized with a dynamic pressure based on midspan wheel speed. The flow coefficient is based on the area averaged inlet axial velocity at Sta. 1. Hub and tip data are shown for the present thick inlet boundary layer case (as the symbols). The midspan reuslts shown have been deduced from the hub and tip data assuming a free-vortex exit swirl distribution. For free-vortex swirl with a 0.8 hub/tip ratio the midspan static pressure rise is 58.3 percent of the way from the hub value to the tip value. The upper limit of flow coefficient for the present data was dictated by the maximum rig flow capacity.

In addition to the present data, two curves are included indicating the hub and tip static pressure rise across the rotor measured in a previous program (Ref. 11) with thin inlet boundary layers. This previous data has been corrected slightly due to the different inlet reference plane locations (Sta. 1 for the present program and Sta. 0 for the previous program, Ref. 11). The previous data has been raised by (0.015) ϕ^2 to account for the boundary layer growth between Sta. 0 and Sta. 1. The flow coefficient (ϕ) from the previous work was also corrected for flow speed based on average inlet velocity, i.e., $\bar{\phi} = 0.98\ \phi$.

Thickening the hub and tip inlet boundary layers has increased the static pressure rise by typically 6 percent with the most pronounced increase at the higher flow coefficients. Stall occurred at a slightly higher flow coefficient with a more abrupt drop in pressure rise near stall. Effects of rotating stall were observed (back flow seen with tufts mounted on the hub and case between Sta. 0 and 1) for any flow coefficient below 0.57.

Surface Flow Visualization

The airfoil and endwall flow visualization (FV) results will be discussed in detail in order to help explain many of the results that can be seen in the traverse data and in the airfoil pressure distributions. FV tests were performed at four values of flow coefficient ranging from $\bar{\phi} = 0.65$ to 0.95. Results are shown in Figs. 6 through 9.

The pressure surface FV traces for $\bar{\phi} = 0.95$ (Fig. 6) show a slight radial outflow over most of the airfoil and especially near the hub and near the trailing edge/tip region. Tip leakage effects are not significant at this high flow coefficient. Localized leading edge separation occurred at midspan due to the

negative incidence. This can be seen in the lack of distinct streak-lines in the midspan region. The suction surface results for $\bar{\phi}$ = 0.95 show a hub corner stall region (with back flow) extending from midchord to the trailing edge at the hub and from the hub radially outward to midspan at the trailing edge. The corner stall caused a displacement of the suction surface flow.

As flow coefficient was decreased to $\bar{\phi}$ = 0.85 and 0.75 (Figs. 7 and 8), several changes in the flow field can be seen. The suction surface hub corner stall increased in both axial and radial extent which caused increased radial displacement of the suction surface boundary layer flow. The impact of tip leakage on both the suction and pressure surface tip regions increased with increased loading. The pressure side boundary layer is being drawn into the tip clearance region causing a relatively high velocity jet on the suction side of the airfoil which draws the suction surface tip region boundary layer radially outward.

In addition to these changes a new streakline became apparent at the aftmost midspan tap location on the suction surface. This is a very narrow streakline with a slight radially inward deflection (shown by "*" in Fig. 8). This streakline can also be seen in results from the previous program (see Ref. 11, Fig. 7). It may be related to a time variant bistable flow shift related to the corner stall with a low intermittency factor, possibly on the order of 5 to 10 percent. The narrowness of the streakline suggests that the flow direction transfer time is very small relative to the time spent at the dominant directions (primary direction-radially outward, secondary direction-radially inward). This effect becomes stronger with decreasing flow coefficient and occurs typically near the forward edge of the back-flow region near midspan.

The flow visualization results for the lowest flow coefficient (highest loading, $\bar{\phi}$ = 0.65, Fig. 9) show strong tip leakage flow on both the pressure and suction surfaces of the airfoil with the most pronounced radial outflow on the pressure side. Suction side results show two back-flow regions, one near the hub, due to the hub corner stall, extending from midchord aft to the trailing edge and out to 75 percent span and one locally near the trailing edge tip region. Radial displacement effects on the suction surface due to the corner stall blockage can be seen to extend forward to the 30 percent chord location near the hub and out to the tip at the trailing edge. Large pitch angles, up to 45°, can be seen on the suction surface near the stalled/back-flow region.

The endwall FV results did show slight circumferential boundary layer displacement due to secondary flow from the pressure surface to the suction surface. No evidence of a scraping vortex or horseshoe vortex could be seen on the airfoil surface or endwall FV results.

From the FV results it can be seen that the airfoil passage flow is extremely three dimensional and strongly affected by loading. On the pressure

surface, effects of the large back-flow/hub corner stall present at the high flow coefficient ($\bar{\phi}$ = 0.95) extend from 50 percent chord to the trailing edge and out to 50 percent span at the trailing edge. As flow coefficient decreases the extent of the back-flow/hub corner stall increases to 30 percent chord to the trailing edge near the hub and out to the tip at the trailing edge.

Many similarities exist between the FV results of the present program and those of previous programs with thin hub and tip inlet boundary layers. From these results it has been observed that both tests had, in general, little radial displacement of the airfoil surface boundary layer when not in the vicinity of the corner stall back-flow region or the tip. The main difference in the flow visualization results between the two programs was at the lowest flow coefficient ($\bar{\phi}$ = 0.65). The effect of the thick inlet boundary layer profiles was to reduce the spanwise extent of the corner stall region by preventing a fullspan separation at the trailing edge. This reduction in extent was caused by the relative unloading at midspan due to the higher than average midspan axial flow speed (see Fig. 3). Finally, due to the negative incidence at midspan, a leading edge pressure surface separation occurred at midspan for the highest flow coefficient ($\bar{\phi}$ = 0.95), whereas, no separation was observed during previous investigations for this flow coefficient.

Therefore, it can be expected, due to the magnitude of the three-dimensional flow present, that the effects seen in the FV results will also be seen in the traverse data as well as in the pressure distribution results. The traverse data should be expected to show large regions of high loss flow present in the airfoil wake below midspan and near the tip for all flow coefficients. It would also be expected that there would not be a decrease in the spanwise loss in the hub region as flow coefficient decreased as was seen in the previous program with thin inlet boundary layers. Pressure distribution results can be expected to show the effects of the suction surface corner separated region at all flow coefficients for radial positions near the hub. In addition, the pressure surface leading edge separation at midspan for flow coefficients at and above $\bar{\phi}$ = 0.95 should show some evidence of negative incidence stall as did the previous pressure distributions at ϕ = 1.06.

Aerodynamic Traverse Results

Total and Static Pressures - In light of the flow visualization (FV) results, a detailed analysis of therotor exit flow in regards to relative total pressure, static pressure, and flow direction (yaw and pitch) is desirable. Contour plots of the total and static pressure results for the four flow coefficients (0.65, 0.75, 0.85 and 0.95) are shown in Figs. 10 through 13. Some of the data for the previous thin inlet boundary layer test is shown in Figs. 14 through 17. All pressures were measured relative to the inlet absolute total pressure at midspan and normalized with a dynamic pressure based on midspan wheel speed. The total pressure is presented in the form of rotary total pressure

$$P_{T,ROT} = P_s + 1/2\ P\ (W^2 - U^2)$$

instead of relative total pressure. Rotary total pressure was chosen for several reasons. First, rotary total pressure is the primary parameter leading to the growth of the streamwise component of vorticity in the rotating frame of reference. Second, it is constant in the region between wakes for the thin boundary layer results (Figs. 14 through 17). Lastly, by eliminating the radial variation of relative total pressure due to radial position, the contours in between wakes for the present program (Figs. 10 through 13) are due solely to the inlet C_x profile.

All traverse data for the present program were acquired at a distance of 30 percent axial chord aft of the rotor trailing edge plane. This distance was chosen because the axial decay of the airfoil wakes was well documented from the previous work ($\Delta X/B_x$ = 0.1, 0.3, 0.5, 1.1) and the corner stall region from the previous program had not closed by 10 percent aft but had closed by the 30 percent aft location.

The results at the highest flow coefficient ($\bar{\phi}$ = 0.95, Fig. 10) show the presence of a relatively thick midspan wake, due to the pressure side leading edge separation. A large high loss (low rotary total pressure) region is present between the wakes at the tip. A smaller high loss region is present in the airfoil wake at the hub due to the corner stall. Generally speaking, the contour lines in the core flow region reflect the inlet total pressure profile.

As loading was increased ($\bar{\phi}$ = 0.85 and 0.75, Figs. 11 and 12) the midspan wake width decreased ($\bar{\phi}$ = 0.85) because of the disappearance of the leading edge pressure surface separation and then increased again ($\bar{\phi}$ = 0.75) due to the effects of the increasing radial extent of the hub corner stall.

The hub corner stall for the lowest flow coefficient ($\bar{\phi}$ = 0.65, Fig. 13) extends out to about 75 percent span. Evidence of weak secondary flow near the hub can be seen as higher total pressure fluid moves down to the hub on the pressure surface side of the airfoil wake. The midpitch tip loss region affects the core flow from the tip down to 75 percent span with the core of the loss region slightly removed from the endwall casing.

Although it appears the magnitudes of the loss regions are decreasing (i.e., fewer contour lines); this is only because of the normalizing parameter (QU_m). When the data are normalized with a dynamic pressure based on some typical exit flow speed, the increase of loss magnitude with flow coefficient is readily apparent.

Static pressure contour results presented with the rotary total pressure results (Figs. 10 through 13) in general reflect the higher pressures at the tip and lower pressures at the hub due to the swirl in the rotor exit flow. The wake center line shows the location of minimum total pressure in the airfoil

wake. As loading increases the static pressure contour lines around the hub corner stall become more distorted. A relatively low static pressure region is present in the wake downstream of the hub corner stall. This low pressure region is due to the displacement of flow around the blockage caused by the stalled region.

The rotary total and static pressure results from Ref. 11 with clean inlet flow are presented in Figs. 14 through 17 for comparison with the present results. Except for the uniform rotary total pressure region between wakes, the results from both test programs show many similarities (tip leakage and hub corner stall). The major difference can be seen at the lowest flow coefficient ($\bar{\phi}$ = 0.65) where the hub corner stall fluid of the clean inflow case was centrifuged to the tip along the fullspan boundary layer separation. This caused a redistribution of low rotary total pressure fluid from the hub to the tip. This did not happen in the present program since, as seen in the FV, the airfoil never experienced fullspan boundary layer separation (due to a more negative incidence at midspan for the same area average flow coefficient). A low static pressure region located near the hub corner stall was present even when the high loss fluid had been centrifuged to the tip and its effect was felt over the entire fullspan wake. Finally, the wide midspan wake present for $\bar{\phi}$ = 0.95 of the present program was not apparent during the previous program since negative incidence stall did not occur until ~ 1.06.

Summarizing the results presented so far, the effect of the thicker inlet boundary layers was to prevent the massive removal of high loss fluid from the hub corner stall to the tip at $\bar{\phi}$ = 0.65 due to more negative incidence for the same area average flow coefficient in the midspan region. There was a monotonic increase in the size of the hub corner stall region as loading increased. Thus, for the lower flow coefficients ($\bar{\phi}$ = 0.65 and 0.75) the tip loss of the present program should be less than that of the previous work, with a possible increase in hub loss depending on the amount of radial displacement flow.

Flow Field Velocities - Flow field velocities and direction (yaw and pitch) were determined from the 5-hole/cobra traverse results. The cobra probe could not sense pitch, therefore, no pitch angle results are shown below 12.5 percent span and velocity vectors shown have no radial component. Relative total flow speed contours and secondary flow vectors are presented in Figs. 18 through 21 and pitch and relative yaw angle contours in Figs. 26 through 29. Because of the relatively small changes in static presusre, shown in the contour plots (Figs. 10-13), the flow speed contours are very similar to the rotary total pressure contours and therefore, many of the same observations can be made.

As expected, based on the FV results, large radial flows in the vicinity of the airfoil wakes (airfoil surface boundary layer fluid) are present in the vector plots (Figs. 18-21). Generally, the wake flow is outward for span locations greater than 50 percent and inward for locations less than 50 percent span.

The relative eddy due to the rotating coordinate system and the axial inlet flow is readily apparent in the core flow region between wakes. The irregularities of the relative eddy, especially near the endwalls are due to shed vorticity and secondary flow due to the tip leakage and the hub corner stall.

Yaw angle contour results (Figs. 22b through 29B) show little circumferential variation except near the airfoil wakes. Some of the variation in the wake is due to the finite probe tip size which makes the probe sensitive to flow shear as well as direction. Significant changes of flow angle with flow coefficient around the hub corner stall can be seen. With increased loading the yaw angle gradients near the corner stall increased dramatically.

Pitch angle results (Figs. 22a through 25a) reflect the presence of the relative eddy with increasing pitch angles from the pressure surface to the suction surface, relatively invariant with radius in the core flow region. Strong pitch angle gradients are present on the pressure surface side of the wake and in the hub corner stall region. Large negative (inward) pitch angles are present in the hub corner stall region for all flow coefficients (see also Figs. 18b through 21b). Large positive (outward) pitch angles are present near the tip especially for $\bar{\phi}$ = 0.65 (Fig. 25) because of the increasingly strong effect of tip leakage.

Pitch Averaged Results - Pitch averaged spanwise results including relative total and static pressure, blockage, exit relative yaw angle, loss and height ratios are shown in Figs. 26 through 36. Results from the 5-hole probe are shown as open symbols while cobra probe results are shown as solid symbols. Except for the loss data, ΔCp_T(rel), in Figs. 33 through 36, which are mass averaged, all results are area averages. Except for loss, there was never any significant difference between mass averaging and area averaging.

Pitch averaged relative total and static pressure results are shown in Fig. 26. The solid lines shown with the results were based on the inlet C_X profile. The differences between the inlet total pressures (lines) and the exit values (symbols) are representative of the rotor relative total pressure loss. The results show a decrease in area averaged total pressure for all flow coefficients with the greatest decrease in total pressure for $\bar{\phi}$ = 0.65 from 20 to 60 percent span and locally near the tip. Midspan loss is generally increasing with decreasing flow coefficient. The decrease in relative total pressure is surprisingly small near the hub considering the presence of the large hub corner stall. This low loss at the hub is due to radial redistribution of the inlet profiles especially at low flow coefficients. This radial transport effect is only possible in those cases where the inlet rotary total pressure is not constant; thus, the radial redistribution which occurred during the previous program with thin inlet boundary layers had minimal effect on the loss distribution. Even though the transport for the present program decreased the pitch area average "loss" in total pressure near the hub and possibly near

the tip, the regions contributing this low loss fluid will have increased loss due to the infusion of high loss fluid from the surrounding flow. Thus, the result of this radial transport mechanism is to reshape the rotary total pressure profile.

Traverse probe static pressure results (Fig. 26) are shown along with the flowpath wall static pressures measured at Sta. 2 and 3. As expected, the traverse results extrapolated well to the tip static measured at Sta. 2 (Fig. 2) but fall slightly below the results at Sta. 3. The hub flowpath static designated as Sta. 2 was actually located 1.50 ins. (3.8 cm) aft of the rotating frame traverse axial loation (30% aft of the trailing edge) making it 60 percent aft of the trailing edge plane which explains the agreement of the Sta. 2 and 3 hub results. As observed in the previous programs, a substantial static pressure rise occurs between the travese plane location and Sta. 3 due to the decrease in wake displacement thickness (blockage).

The static pressure rise due to wake mixing is illustrated in more detail with the static pressure results from Ref. 11 (with thin inlet boundary layers) in Figs. 27. At traverse locations further aft relative to the rotor trailing edge, there is a general increase in static pressure and the extrapolation of the spanwise distribution of static pressure approaches the downstream (Sta. 3) (mixed out) flowpath static pressure. From these results (Fig. 27), the static pressure from even the most severe case of back-flow in the rotor passage approaches the mixed out value between 50 and 110 percent axial chord aft of the rotor trailing edge plane which is substantiated by the excellent agreement between the $\Delta X/B_X = 1.1$ traverse results and the Sta. 3 flowpath results.

It is interesting to note that even in this earlier data there was a static pressure depression associated with the high loss hub corner stall region. When this corner stall was eliminated (at $\bar{\phi} = 0.65$) by the fullspan boundary layer separation the low static pressure region moved to the tip along with the high loss concentration (Figs. 17 and 27).

The concept of "blockage" is an empirical attempt of the compressor analyst to account for the differences in a through-flow calculation between mass averaged quantities, such as work, and area averaged quantities, such as mass flow. Historically, blockage has been based on estimates derived from past experience and from little direct physical measurement. The detailed results of the present program, however, allow one to calculate blockage directly from the measured flow quantities. Blockage may be defined as the ratio of the area averaged mass flow ($\overline{Cx}^a$) to the mass flow calculated from the mass averaged total and static pressures and the mass averaged flow angles. Blockage ($\bar{K}$) may then be calculated as follows (for incompressible flow).

$$\bar{K} = \frac{\overline{C_X}^a}{\overline{C_X}^{PT}}$$

where $\bar{C}_x^{P_T} = \left(2\sqrt{\overline{P_T}^m - \overline{P_s}^m}/P\right) \cos \bar{\theta}^m \cos \bar{\phi}^m$

Note that $\bar{K}$ is a function of radius and that all of these area and mass averages can be calculated directly from the measured data at each radius. As mentioned above, there is a significant difference between the area and mass averaged total pressure but the differences for the static pressure, yaw, and pitch are very small (for the data presented here).

Results from the present program as well as those from the previous program (Ref. 11) for the traverse plane at $\Delta X/B_x = 0.30$ are shown in Fig. 28a and 28b respectively. Additional results from the previous program for two flow coefficients ($\phi = 0.85$ and 0.65) for the traverse locations ($\Delta X/B_x = 0.1$, 0.3, 0.5 and 1.1) are shown in Figs. 29 and 30.

Blockage due to the hub corner stall for the present program (Fig. 28a) shows a large increase in magnitude and spanwise extent as loading is increased. This is consistent with the rotary total pressure results (Figs. 10-13) as well as with the FV results (Figs. 6-9). Blockage extends from the hub to 25 percent span for $\bar{\phi} = 0.95$ and to 60 percent span for $\bar{\phi} = 0.65$. Blockage at the tip for all flow coefficients is high but localized to the uttermost 15 to 20 percent span with a slight increase in blockage magnitude with loading. Blockage from the previous program in Fig. 28b shows that as loading was increased the blockage near the hub increased as the flow coefficient dropped from 0.95 to 0.85 and then decreased at 0.75 and 0.65 when the fullspan boundary layer separation allowed radial redistribution of the high loss flow from the hub to the tip. This decreased the hub blockage but substantially increased the tip blockage (primarily for $\bar{\phi} = 0.65$).

As Figs. 29 and 30 show, blockage drops rapidly due to mixing with increasing distance downstream of the airfoil trailing edge. Figure 29 also shows that even for relatively high flow coefficients, large blockage can be present close to the airfoil trailing edge because of back-flow in the corner stall near wake. This back-flow in the traverse plane 10 percent aft of the trailing edge prevented data acquisition in the hub region. At the low flow coefficient the blockage in the near wake ($\Delta X/B_x = 0.10$, $\bar{\phi} = 0.65$, Fig. 30) is more dramatic, characterized by large fullspan blockage with larger local blockages near the hub and tip. The back-flow region did not reach the traverse plane at this low flow coefficient and data was acquired all the way to the hub.

Area averaged exit axial velocity profiles are presented along with the inlet axial velocity profiles (solid lines) in Fig. 31. The exit profiles show substantial radial displacement of flow from the 20 to 50 percent span region to surrounding areas, namely, 0 to 20 percent span and 60 to 80 percent span with more pronounced displacement occurring for the two lower flow coefficients ($\bar{\phi} = 0.65$ and 0.75). These results generally agree with preceeding results

relating to large amounts of flow displacement due to the large blockage resulting from the hub corner stall.

Pitch averaged rotor exit relative yaw angles (Fig. 32) are shown with the leading and trailing edge metal angles (θ^*) calculated relative inlet yaw angles. Included with the present data are inlet and exit yaw angles from the previous program with thin inlet boundary layers (constant rotary total pressure). From the figure, differences in incidence, deviation, and turning between the two inlet conditions can be seen. From the inlet angles it can be seen that the rotor in the present program was more heavily loaded at the hub and tip and less heavily loaded in the midspan region than the previous program. The flow in the present program had much more turning at the hub and tip with decreased turning at midspan. This has much to do with the substantially different spanwise performance of the rotor in the two programs. At the low flow coefficient ($\bar{\phi}$ = 0.65) the lower midspan loading in the present program prevented a fullspan trailing edge separation which allowed the low total pressure fluid in the hub corner stall of the previous program to be centrifuged out to the tip (Fig. 17). This outward migration of the high loss low momentum fluid in the hub corner stall region produced a well behaved (high turning low loss) flow condition near the hub for the low flow coefficient $\bar{\phi}$ = 0.65 (see Fig. 17 and 32). In the present program, however, the unseparated suction surface boundary layer at $\bar{\phi}$ = 0.65 prevented the centrifuging of the corner stall, causing the flow at this condition to be qualitatively similar to the flow at higher flow coefficients but with a more severe corner stall with higher deviation. Exit relative yaw angles are generally in good agreement with the previous data except for the lowest flow coefficient ($\bar{\phi}$ = 0.65) where there was a radial redistribution of deviation (due to the radial redistribution of low total pressure fluid. In the previous results this did not occur. The effect was that at this flow coefficient ($\bar{\phi}$ = 0.65) the data of the present program indicated more deviation below midspan and less above midspan than did the data of the previous program.

Spanwise distribution of mass average loss (ΔC_{PT}(rel)), contraction ratio (h_2/h_1) and exit relative yaw angle (θ) for the four flow coefficients are shown in Figs. 32 through 36. These data along with the inlet relative yaw angle are the input parameters required for any potential flow calculation (e.g., Caspar et al., Ref. 16). The lines shown with the data are from the previous isolated rotor work (thin inlet boundary layers). For all flow coefficients, the present program had higher loss in the midspan region (15 to 80% span) with lower loss at the hub and tip. As one might expect the tip loss increased with increased loading. However, the near hub net loss was unusually low. This is somewhat surprising in light of the monotonically increasing corner stall seen in the rotary total pressure contours (Figs. 10 through 13). The radial displacement of low loss flow has significantly affected the fullspan nature of the spanwise variation of loss. Generally, the hub and tip loss have been substantaially reduced by radial displacement of high

total pressure fluid into those areas with increased loss in the lower and upper midspan region (see Fig. 26). This effect is most pronounced at the lowest flow coefficient ($\bar{\phi}$ = 0.65, Fig. 36) but is also apparent at $\bar{\phi}$ = 0.95 where at the hub a slightly negative loss was determined because of a combination of low loading, thus smaller hub corner stall, and radial displacement of flow. This slightly negative loss (implying a total pressure increase at this radius) was the result of enough high total pressure fluid being displaced radially into the hub region such that the mass averaged total pressure increased to a value above the inlet total pressure at the same radius.

Contraction ratio (h_2/h_1) results are also shown in Figs. 33 through 36. The highest flow coefficient case ($\bar{\phi}$ = 0.95, Fig. 33) shows little expansion or contraction over the center 80 percent of the span with only minor variations from a value of 1.0 near the endwalls. At lower flow coefficients ($\bar{\phi}$ = 0.85 and 0.75) there was increased contraction in the hub region (h - ratio less than 1.0) with expansion occurring from 15 to 35 percent span and from 90 percent outward. At the lowest flow coefficient ($\bar{\phi}$ = 0.65, Fig. 36) the effect of the severe hub corner stall, characterized by low loss at the hub and higher loss in the lower midspan region, can be seen as a region of expansion for spanwise locations between 20 and 60 percent while tip loss only affects the outer 10 percent. Generally speaking, regions of higher net loss are characterized by streamtube expansion (h - ratios greater than 1.0) and surrounding low loss regions by streamtube contraction (h - ratios less than 1.0).

Summarizing these aerodynamic results, one can see that the total pressure contour results do not present the total picture in regards to net mass averaged loss when the inlet rotary total pressure is as severely distorted as it is in the present program (Fig. 26). The radial displacement of the high total pressure fluid significantly affects the spanwise distributions of net loss and contraction ratio. Significant amounts of pressure rise occur aft of the traverse plane as is evidenced by the difference in static pressure results from the fullspan traverse data and from the flowpath static pressures further downstream (Sta. 3). The FV (flow visualization) results were extremely helpful in explaining many of the secondary flow effects observed in the traverse data.

Airfoil Pressure Distributions

Midspan Pressure Distributions - Airfoil pressure distributions at midspan flow coefficients varying from $\bar{\phi}$ = 0.60 (near stall, Fig. 5) to $\bar{\phi}$ = 1.00 are shown in Fig.37. Included with the measured results (symbols) are the measured Sta. 2 traverse static pressures (the symbol at X/B_X = 1.0) and computed potential flow distributions based on the measured aerodynamic input data (shown in Figs. 33-36) and on extrapolations of this data where necessary. Pressure distributions from previous results with clean inlet flow, for comparison, can

be found in Ref. 11, Fig. 38. In both cases the computed distribution was by the method of Caspar et al. (Ref. 12).

At the highest flow coefficient (1.0) a strong leading edge pressure surface overspeed was predicted when in fact, as the data indicates, a leading edge separation occurred. Good agreement between the measured and computed results is seen over the rest of the airfoil surface, particularly on the suction surface. This indicates that the separated region was rather small in extent. As loading is increased the effects of the pressure surface leading edge separation become smaller and are gone by $\bar{\phi}$ = 0.90. Excellent agreement can be seen between the measured and computed results for all flow coefficients from 0.90 to 0.70. As loading is increased further ($\bar{\phi}$ = 0.65 and 0.60) the effects of the hub corner stall can be seen at midspan to be affecting the suction surface trailing edge pressure from about midchord aft to the trailing edge. This is evident by the nearly constant static pressures in that region. Pressure surface results are in excellent agreement even down to the lowest flow ($\bar{\phi}$ = 0.60). In general, there is excellent agreement between the computed downstream static pressure and the value computed from the traverse results at Sta. 2 (plotted at X/B_X = 1.0). The smoothness of the point to point data (taken on two different airfoils) indicates excellent periodicity in the flow. This high degree of periodicity is also evident in the traverse results taken over two pitches (Figs. 10-25).

Fullspan Pressure Distributions - Fullspan airfoil pressure distributions for the four flow coefficients ($\bar{\phi}$ = 0.95, 0.85, 0.75 and 0.65) are shown in Figs. 38 through 41. Station 2 traverse static pressure data as well as computed potential flow results (based upon measured inlet and exit data) are shown with the measured pressure distributions data. Pressure distributions from the previous program with clean inlet flow, for comparison can be found in Ref. 11, Figs. 39 and 40.

The data at 75 percent span were the only results, for all flow coefficients, not significantly affected by either the hub corner stall or the tip flow. This is seen in the excellent agreement between the measured and computed results at the four flow coefficients. Agreement between the measured and computed results for 87.5 and 95 percent span were less than ideal due to the complicated nature of the tip flow. Tip leakage and endwall effects caused less than computed pressure surface leading edge and suction surface trailing edge measured pressures which were the result of the localized flow overspeed caused by the tip blockage effects. Better agreement between the measured and computed results is seen in the tip region as flow coefficient is decreased. From 50 percent span inward, the effects of the hub corner stall are clearly seen (especially at the lower flow coefficients). For $\bar{\phi}$ = 0.95 (Fig. 38) the stall strongly affects the suction surface flow out to 25 percent span and at the hub (4 percent span) from midchord to the trailing edge. As flow coefficient is decreased to $\bar{\phi}$ = 0.65 (Fig. 41) the effect of the hub corner

stall extends to midspan (affecting the last 40 percent chord). At 4 percent span the impact of the corner stall can be seen in the pressure distribution from midchord aft to the trailing edge. Slightly lower surface pressures were measured near the hub (4% and 12.5% span) than were computed due to the blockage of the corner stall. Again, better agreement is seen between the measured and computed results as loading is increased from $\bar{\phi}$ = 0.95 to 0.65. In general, the airfoil surface pressure distributions reflect the observations made from the FV results.

Airfoil Pressure Force - The forces exerted on the rotor airfoil at various flow conditions have been calculated from the measured airfoil pressure distribution data and are shown in Fig. 42. The forces are normalized with QU_m and τ_m such that spanwise variations are solely due to changes in airfoil force and not the normalizing parameters. Forces were calculated by integrating around the surface of the airfoil and by linearly interpolating between measured data points. Skin friction force was estimated to be typically 2 percent of the pressure force. Thus, the calculated forces account for essentially all of the total force on the airfoil. Calculated airfoil forces for this airfoil in the previous program with clean inlet flow can be found for comparison in Ref. 11, Fig. 41.

The pressure force data from the present program was generally well behaved and similar to the results of the previous program. Small differences do exist in the hub and tip regions. The hub and tip forces did not exhibit the same drop off in force as in the previous program due to the increased loading at the hub and tip (i.e., increased incidence, Fig. 32).

Trace Gas Traverse Results

Concentration Contours - Tip and hub data, although measured separately, are presented together in Figs. 43a through 46a. Midspan results are presented in Figs. 43b through 50b. Contour levels were determined at 10 percent intervals between the measured minimum (background) and maximum concentration levels. Radial displacement effects are more easily seen where the concentration gradient is the largest as at the 50 percent contours (see inlet profiles in Fig. 4). Due to the axisymmetric nature of the inlet profiles, any radial displacement of the contour lines are directly related to the radial displacement of the flow between the injection site upstream of the rotor and the downstream traverse plane at Sta. 2 (Fig. 2). The wake center line has been included to help in the understanding of the origin of displaced fluid.

The radial transport is most clearly evident in the region around the airfoil wake ($\bar{\phi}$ = 0.95, Fig. 43). At this flow coefficient, radial transport is generally away from midspan on the suction surface side of the wake and toward midspan on the pressure surface side of the wake. This is consistent with

the secondary flow vectors in Fig. 18. There is a general migration of fluid toward the suction side of the wake in the midspan region causing the strong displacement of flow away from midspan with fluid being drawn away from the pressure surface of the adjacent airfoil. This caused a weak displacement toward midspan near the pressure surface side of the wake. The amount of rotation of the contour lines in the midspan region (due to the relative eddy) and in the endwall regions (due to the secondary flow) was very slight. The contribution of the relative eddy was estimated from the traverse data (Fig. 18). The relative eddy is due to the axial component of vorticity being -2Ω in the rotating frame of reference (when the inlet flow is irrotational as in the midspan region, Fig. 3). The relative vorticity is expressed in terms of gradients in the relative tangential and radial velocity components as follows.

$$\delta_x = \frac{1}{r}\left[\frac{\partial(rW_\theta)}{\partial} - \frac{\partial W_r}{\partial\theta}\right] = -2\Omega$$

Radial transport due to the relative eddy will occur due to the term involving W_r (which is zero in free-vortex flow). At a flow coefficient of 0.95 this term accounts for roughly 10 percent of the total and this would lead to a stream surface rotation (in the midspan region) of only about 1°. Thus the negligible rotation at midspan due to the relative eddy evident in Fig. 43 is consistent with the velocity vector (vorticity) data of Fig. 18.

As the loading was increased ($\bar{\phi}$ = 0.85 and 0.75, Figs. 44 and 45) midspan wake transport increased. This is more easily seen in the midspan data for $\bar{\phi}$ = 0.75 at the contours where midspan wake flow has a normalized concentration of from 70 to 80 percent (Fig. 45). Displacement effects between the wake in the tip region appear to be moving fluid away from the tip endwall. This is evident by the tip 90 percent contour line moving toward the tip and the 70 and 60 percent contours toward midspan as loading increases. Although it appears that lesser amounts of flow are being radially transported below midspan compared to the flow above midspan, the same amount of transport is not necessary below midspan to give the same total pressure change effect as above midspan. This is because the gradient of the spanwise relative total pressure is much stronger near the hub compared to the tip (see Fig. 26), thus for the same total pressure change roughly 2/3 of the amount of flow displacement necessary near the tip is needed to produce the same change near the hub.

At the lowest flow condition ($\bar{\phi}$ = 0.65, Fig. 46) large amounts of radial transport in the airfoil wake are apparent. Large increases in radial displacement on the suction surface occur as can be seen most clearly in the tip and hub contour results (Fig. 46). For this flow coefficient the core of the tip loss flow has clearly lifted from the rotor endwall casing as can be seen by the large gap between the 70 and 80 percent contours at the tip, between the wakes.

Pitch Averaged Results - Pitch averaged results of the normalized concentration data are shown in Fig. 47 with the measured inlet concentration profiles and the estimated Sta. 2 profiles determined from the pretest results acquired during the development of the injection system. These estimated profiles are what would have resulted for axial flow in the annulus without the rotor present. The pitch averaged data at Sta. 2 do not go to 1.0 at the highest concentration level because the normalizing parameters were based on the local minimum and maximum measured concentrations for a particular set of traverse results. The agreement between the pitch averaged data and the Sta. 2 estimates is good with the greatest difference being in the tip region. In particular, for the lowest and highest flow coefficients ($\bar{\phi}$ = 0.65 and 0.95) there is considerable difference from 80 percent span outward. For these two flow coefficients the near tip pitch averaged concentration is affected by the infusion of high concentration trace gas flow, in regard to the midspan profile (causing an increase in concentration), and by the infusion of low concentration trace gas for the tip profile (causing a decrease in concentration). Except for these two differences, there is little dependence on flow coefficient in the results.

Summarizing the trace gas concentration results, the concentration contours generally reflect the same results as those of the FV, secondary flow vectors, and pitch angle contour results (Figs. 6 through 9, 18 through 21, and 22 through 25). There was a general accumulation due to cross-flow migration of midspan fluid on the suction surface side of the airfoil wake. The rotation of the Bernoulli surfaces was slight because only a small fraction of the axial component of vorticity was related to the gradient of the radial component of velocity in the tangential direction. There was a general increase in radial displacement of airfoil passage and wake flow with decreasing flow coefficient. The core of the tip loss region eventually, with increased loading, lifted from the tip endwall.

SUMMARY OF RESULTS

1. The effects ofthe increasingly severe hub corner stall with increased loading could be seen in the flow visualization, the rotary total pressure, the airfoil surface pressure distribution, and in the blockage results.

2. For all loadings there was increased loss in the midspan region and decreased loss near the hub and tip regions relative to previous results with clean inlet flow.

3. The trace gas concentration contours indicated a general increase in radial displacement of flow with increased loading.

4. Static pressure rise was increased by approximately 6 percent at the design flow coefficient compared to previous results with clean inlet flow.

5. Effects of a pressure surface leading edge separation were seen in the flow visualization results and airfoil surface pressure distributions in the midspan region for the highest flow coefficients ($\bar{\phi}$ = 0.95 and 1.00).

6. The rotation of the rotor passage flow due to the relative eddy was small because of the relatively small contribution of the circumferential derivative of the radial component of velocity to the axial component of relative vorticity.

7. Significant amounts of pressure rise occurred aft of the traverse plane due to wake mixing and the subsequent decay of the wake displacement thickness. This could be seen in the difference between the traverse static pressures and those from far downstream.

8. Low static pressure regions were located immediately aft of the hub corner stall with large yaw angle gradients in the circumferential direction.

9. The effects of tip loss on the airfoil pressure distribution and on the rotary total pressure results became stronger as loading was increased with an eventual lifting of the center of the low total pressure region from the tip endwall.

10. The large blockages that were present in the hub and tip regions increased with loading.

11. Airfoil forces in the hub and tip region were increased due to the increased loading (incidence) in the endwall region compared to previous results with clean inlet flow.

12. Exit relative flow angles were only weakly affected by the presence of the thick inlet boundary layer profiles unlike the previous program which, for the lowest flow coefficient, reflected the effects of the massive transport of the hub corner stall to the tip.

13. Contraction ratio spanwise profiles were very similar in shape to the spanwise profiles of net mass averaged loss in both the present program and in the previous isolated rotor work.

CONCLUSIONS

An extensive body of experimental results has been presented which provides detailed information as to the nature of the flow over an isolated axial compressor rotor with thick hub and tip inlet boundary layers. By simulating the incoming flow of a middle stage compressor rotor, secondary flow effects could be determined for comparison with a benchmark study which had thin inlet boundary layers. This additional data will be most useful in improving present through-flow analyses used in the design and diagnostic phases of compressor development. Major specific conclusions are as follows.

1) The relative unloading of the midspan portion of the airfoil inhibited a fullspan separation which prevented the hub corner stall high loss flow from centrifuging to the tip and had occurred with the thin inlet boundary layer at the lowest flow coefficient.

2) The radial redistribution of mass averaged loss was the direct result of the radial displacement of rotor passage flow. Specifically, the radial redistribution consisted of the exchange of high total pressure fluid in the midspan region with low total pressure fluid near the hub.

3) Regions of high net mass averaged loss are characterized by a flow expansion (h - ratios greater than 1.0) surrounded by low loss regions characterized by a flow contraction (h - ratios less than 1.0), due to the effects of the large blockage present in the high loss regions.

4) The ability to determine blockage has been demonstrated. Large blockage has been found to be present in the endwall regions, due to the corner stall and tip leakage, with relatively little blockage in the core flow region. Hub blockage was found to increase rapidly with loading.

APPENDIX A

5-Hole/Cobra Probe Calibration

Since the probe was such a key feature of the program, its design and calibration are described in detail. The combination 5-Hole/Cobra probe is shown in Fig. 48. The tip of the 5-Hole sensor (lower sensor) was on the shaft axis so that as the probe was rotated in yaw the sensor location would be fixed. The tip of the Cobra sensor (upper sensor) was also on the shaft axis for the same reason. The 5-Hole sensor could be positioned radially from a location very close to the outer case of the compressor (97% span) to a location approximately 3/4 inch from the rotor hub (13% span). The Cobra sensor was added in order to provide additional data down to approximately 1/4 inch from the rotor hub (4% span). The yaw and pitch angles for the probe are shown in the figure. This notation was used in the calibration results presented in Figs. 49 and 50. In the actual test, however, with the probe shaft coming radially out from the rotor hub (Fig. 1) the directions of yaw and pitch were of opposite sign. Pitch was positive in the radially outward direction and yaw was positive in the direction of rotor motion. These sign conventions were included in the data reduction calculation.

The notation for the total of eight sensor pressure taps is shown in Fig. 48. For the Cobra sensor, tap 1 was impact pressure while taps 2 and 3 were for yaw nulling and dynamic pressure. For the 5-Hole sensor, tap 5 was for impact pressure while taps 7 and 8 were for yaw nulling and taps 4 and 6 were for dynamic pressure and pitch.

Probe calibration was carried out in an air jet issuing from a 1.5 inch diameter nozzle. The jet was sufficiently large such that both the 5-Hole and Cobra sensors could be calibrated simultaneously. Calibration was carried out at a typical flow speed of 125 ft/sec. This relatively high speed was used in order to reduce the effect of the fixed manometer reading errors (approximately ± 0.01 inches of water). This method was permissible owing to the insensitivity of the probe calibration parameters to flow speed. The calibration was performed by setting the probe at a particular pitch, nulling the Cobra taps 2 and 3 in yaw, reading the yaw position relative to a flag mounted on the shaft and reading the pressures on taps 1 and 3. The 5-Hole sensor was then yawed until taps 7 and 8 balanced (null) and then the probe yaw angle and the pressures on taps 4 through 8 were recorded.

Typical calibration results are presented in Figs. 49 and 50 in terms of the various dimensionless coefficients that were used in the data reduction calculation. For the 5-Hole sensor the pitch parameter (Fig. 49a) was monotonic and nearly linear over a broad range. The dynamic pressure parameter (Fig. 49b) and the total pressure parameter (Fig. 49c) were smooth and well

behaved. The variation in the yaw angle at which null occurs (Fig. 49d) varied nearly linearly and by less than 6° over the entire range of pitch. Finally, the symmetry about a pitch of 0° indicated little or no interaction between the 5-Hole and Cobra sensors. The Cobra sensor results are shown in Fig. 50 as a function of pitch to indicate that over a wide range (± 15°) they are insensitive to pitch. This was importnat since the Cobra did not sense pitch. Only the constant values of the various dimensionless parameters at zero pitch were used in the data reduction.

APPENDIX B

Magnetic Tape Data Format

Card Type	Format
Index cards	80A1
Control card	for UTRC use
Title card	80A1
Data cards	1X, 2I4, 2F6.2, 5F8.3

Aerodynamic Traverse Data	Trace Gas Concentration Data
Run number	
Point number	
Circ. sequence number	
Radial position, ins. from center line	
Circumferential position	
Total pressure coefficient	(Trace Gas Conc., ppm)
Static pressure coefficient	(N/A)
C_x/U_m	(N/A)
Yaw, degrees	(N/A)
Pitch, degrees	(N/A)
Control card	

A sample of the data format is provided on the following page where the first 84 lines of aerodynamic traverse data have been listed. Lines 1 through 7 are the Index cards describing the location of the various planes of data for each axial location and for each value of C_x/U_m. Line 8 is a Control card. Line 9 is a Title card. Lines 10 through 50 are Data cards for the first 41 circumferential locations at which data was obtained at a radius of 24.30 ins. (0.30 ins. from the hub). This is Cobra probe data and hence the pitch angle (listed in the right hand column) is zero. Line 51 is a Control card. Lines 52 through 84 are the data cards for the 24.45 in. radial position. This sequence continues with increasing radius down to line number 990 (as indicated in line 3 of the indes). At line 991 the data for a different $\bar{\phi}$ begins.

The trace gas concentration data uses the same format with differences noted in parentheses next to aerodynamic data nomenclature.

```
1:C      INDEX
2:C
3:C      CX/U = 0.65, LINES    8- 990
4:C      CX/U = 0.75, LINES  991-1906
5:C      CX/U = 0.85, LINES 1907-2832
6:C      CX/U = 0.95, LINES 2833-3764
7:C
8:    2   1   0   1   0.     12.857        .000
9:   NASA THICK BOUNDARY LAYER  -  REL. FRAME  -   CX/U= 0.65
10:  76   6   1 24.30    .00   -.421   -.028    .648 -10.402    .000
11:  76   6   2 24.30    .99   -.465   -.026    .651 -13.230    .000
12:  76   6   3 24.30   2.00   -.514   -.038    .651 -15.477    .000
13:  76   6   4 24.30   3.00   -.537   -.014    .654 -18.268    .000
14:  76   6   5 24.30   4.00   -.483    .030    .652 -24.685    .000
15:  76   6   6 24.30   4.50   -.279    .119    .651  32.333    .000
16:  76   6   7 24.30   5.00   -.049    .080    .649 -41.686    .000
17:  76   6   8 24.30   5.50    .046    .047    .649 -45.746    .000
18:  76   6   9 24.30   6.00    .026    .087    .650 -21.893    .000
19:  76   6  10 24.30   6.50   -.067    .073    .650   6.200    .000
20:  76   6  11 24.30   6.99   -.133    .081    .652  11.958    .000
21:  76   6  12 24.30   7.50   -.153    .013    .652   6.708    .000
22:  76   6  13 24.30   7.99   -.264    .020    .651   3.808    .000
23:  76   6  14 24.30   8.50   -.300   -.018    .651    .618    .000
24:  76   6  15 24.30   9.00   -.317    .016    .650  -1.920    .000
25:  76   6  16 24.30   9.50   -.332    .027    .652  -4.022    .000
26:  76   6  17 24.30  10.00   -.345    .009    .651  -5.581    .000
27:  76   6  18 24.30  10.49   -.362   -.031    .651  -7.067    .000
28:  76   6  19 24.30  11.00   -.373   -.010    .652  -7.756    .000
29:  76   6  20 24.30  11.99   -.384   -.024    .651  -9.351    .000
30:  76   6  21 24.30  12.99   -.431   -.033    .650 -10.438    .000
31:  76   6  22 24.30  13.99   -.478   -.041    .648 -12.577    .000
32:  76   6  23 24.30  15.00   -.511   -.034    .649 -14.643    .000
33:  76   6  24 24.30  15.99   -.534   -.033    .649 -17.181    .000
34:  76   6  25 24.30  16.50   -.505   -.002    .648 -20.371    .000
35:  76   6  26 24.30  16.99   -.326   -.011    .651 -26.678    .000
36:  76   6  27 24.30  17.49   -.115    .033    .652 -32.116    .000
37:  76   6  28 24.30  17.99    .002    .027    .652 -27.911    .000
38:  76   6  29 24.30  18.49   -.052    .073    .651  -3.515    .000
39:  76   6  30 24.30  18.99   -.143    .116    .649   7.723    .000
40:  76   6  31 24.30  19.50   -.189   -.059    .651   8.412    .000
41:  76   6  32 24.30  20.00   -.257   -.033    .647   4.207    .000
42:  76   6  33 24.30  20.51   -.281   -.030    .649   1.307    .000
43:  76   6  34 24.30  20.99   -.309   -.024    .653  -1.702    .000
44:  76   6  35 24.30  21.49   -.332    .008    .651  -3.515    .000
45:  76   6  36 24.30  22.00   -.339   -.020    .648  -5.001    .000
46:  76   6  37 24.30  22.50   -.333   -.019    .652  -6.451    .000
47:  76   6  38 24.30  23.00   -.341   -.008    .650  -7.538    .000
48:  76   6  39 24.30  23.90   -.370    .004    .648  -8.845    .000
49:  76   6  40 24.30  24.81   -.383   -.023    .650  -8.952    .000
50:  76   6  41 24.30  25.71   -.421   -.028    .648 -10.402    .000
51:1
52:  76   5   1 24.45    .00   -.486    .001    .649 -15.803    .000
53:  76   5   2 24.45    .99   -.512   -.043    .651 -17.543    .000
54:  76   5   3 24.45   2.00   -.540   -.022    .651 -18.667    .000
55:  76   5   4 24.45   3.00   -.564   -.030    .650 -20.081    .000
56:  76   5   5 24.45   3.99   -.511    .008    .654 -23.561    .000
57:  76   5   6 24.45   4.50   -.332    .104    .648 -30.412    .000
58:  76   5   7 24.45   5.00   -.055    .064    .652 -36.864    .000
59:  76   5   8 24.45   5.50    .029    .056    .650 -38.133    .000
60:  76   5   9 24.45   6.00   -.002    .070    .648 -12.795    .000
61:  76   5  10 24.45   6.50   -.076   -.024    .650   9.825    .000
62:  76   5  11 24.45   7.00   -.183    .111    .648   7.542    .000
63:  76   5  12 24.45   7.49   -.244   -.011    .649   3.228    .000
64:  76   5  13 24.45   8.00   -.318    .062    .651  -1.312    .000
65:  76   5  14 24.45   8.50   -.374    .060    .649  -4.348    .000
66:  76   5  15 24.45   9.00   -.409    .025    .647  -8.009    .000
67:  76   5  16 24.45   9.50   -.445   -.019    .651  -9.242    .000
68:  76   5  17 24.45  10.00   -.439   -.002    .651 -11.634    .000
69:  76   5  18 24.45  10.49   -.462   -.011    .650 -12.795    .000
70:  76   5  19 24.45  11.00   -.450   -.029    .649 -13.846    .000
71:  76   5  20 24.45  11.99   -.468   -.028    .649 -15.259    .000
72:  76   5  21 24.45  12.99   -.496   -.027    .651 -15.885    .000
73:  76   5  22 24.45  14.00   -.513   -.034    .653 -16.742    .000
74:  76   5  23 24.45  15.00   -.548   -.029    .649 -17.471    .000
75:  76   5  24 24.45  15.99   -.566   -.036    .649 -18.595    .000
76:  76   5  25 24.45  16.50   -.551   -.030    .648 -20.045    .000
77:  76   5  26 24.45  16.99   -.391    .028    .650 -23.847    .000
78:  76   5  27 24.45  17.49   -.123    .029    .648 -28.890    .000
79:  76   5  28 24.45  17.99   -.010    .005    .651 -22.256    .000
80:  76   5  29 24.45  18.49   -.076    .010    .647   -.614    .000
81:  76   5  30 24.45  18.99   -.144    .041    .649   3.590    .000
82:  76   5  31 24.45  19.50   -.286    .067    .649   1.887    .000
83:  76   5  32 24.45  19.99   -.345    .035    .651  -1.122    .000
84:  76   5  33 24.45  20.51   -.367   -.026    .650  -4.638    .000
```

AERODYNAMIC TRAV. DATA | TRACE GAS CONC. DATA

- LINE NO.
- RUN NO.
- POINT NO.
- CIRC SEQUENCE NO.
- RADIAL POSITION
- CIRCUMFERENTIAL POSITION
- C_{PT} (CONCENTRATION, ppm)
- C_{PS} (NA)
- C_x/U_m (NA)
- YAW (NA)
- PITCH (NA)

REFERENCES

L. Lakshminarayana, B. and J. H. Horlock: Leakage and Secondary Flows in Compressor Cascades. A.R.C.R. & M. No. 3483, March 1965.

2. Moore, R. W., Jr., and D. L. Richardson: Skewed Boundary Layer Flow Near the End Walls of a Compressor Cascade. ASME Paper No. 56-A-131, July 1956.

3. Langston, L. S., M. S. Nice and R. M. Hooper: Three-Dimensional Flow Within a Turbine Cascade Passage. Trans. ASME, J. Eng. for Power, Vol. 99, January 1977.

4. Graziani, R. A., M. F. Blair, J. R. Taylor and R. M. Mayle: An Experimental Study of Endwall and Airfoil Surface Heat Transfer in a Large Scale Turbine Blade Cascade. ASME Paper No. 79/GT/99, March 1979.

5. Phillips, W. R. C. and M. R. Head: Flow Visualization in the Tip Region of a Rotating Blade Row. Int. J. Mech. Sci., Vol. 22, pp. 495-521, January 1980.

6. Schmidt, D. P. and T. H. Okiishi: Multistage Axial-Flow Turbomachine Wake Production, Transport and Interaction, AIAA Journal, Vol. 15, 1977, pp. 1138-1145.

7. Reynolds, B. and B. Lakshminarayana: Blade Loading and Spanwise Effects on the Near and Far Wake Characteristics of a Compressor Rotor Blade. AIAA Paper No. AIAA-80-0201, 18th Aerospace Sciences Meeting, January 14-16, 1980, Pasadena, CA.

8. Kool, P., J. DeRuyck and C. Hirsch: The Three-Dimensional Flow and Blade Wake in an Axial Plane Downstream of an Axial Flow Compressor Rotor. ASME Paper No. 78-GT-66, March 1978.

9. Dring, R. P., H. D. Joslyn, L. W. Hardin and J. H. Wagner: Research on Turbine Rotor-Stator Aerodynamic Interaction and Rotor Negative Incidence Stall. J. of Eng. for P., Vol. 104, October 1982.

10. Adkins, G. G. and L. H. Smith, Jr.: Spanwise Mixing in Axial-Flow Turbomachines. ASME Paper No. 81-GT-57, March 1981.

11. Dring, R. P., H. D. Joslyn and L. W. Hardin: Compressor Rotor Aerodynamics - An Analytical and Experimental Investigation. UTRC Report No. UTRC80-15, 1980.

12. Dring, R. P., H. D. Joslyn and L. W. Hardin: Experimental Investigation of Compressor Rotor Wakes, AFAPL-TR-79-2107, Air Force Aero Propulsion Laboratory, Technology Branch, Turbine Engine Division (TBX), Wright-Patterson Air Force Base, OH 45433.

13. Ruden, P.: Investigation of Single Stage Axial Fans. NACA RM No. 1062, April 1944.

14. Johnson, J. P.: A Wall-Trace Flow Visualization Technique for Rotating Surfaces in Air. Trans. ASME, J. Basic Eng., p. 907, December 1964.

15. Dring, R. P. and H. D. Joslyn: Measurements of Turbine Rotor Blade Flows. ASME J. of Eng. for P., Vol. 103, No. 2, April 1981.

16. Caspar, J. R., D. E. Hobbs and R. L. Davis: Calculation of Two-Dimensional Potential Cascade Flow Using Finite Area Methods. AIAA Journal, Vol. 18, No. 1, January 1980, pp. 103-109.

TABLE I

ROTOR AIRFOIL GEOMETRY

Contour - NACA 65 Series
Chord (B) - 6 ins. (0.1524 m.)
Camber - Circular Arc
No. of Airfoils - 28

Span (%)	0	25	50	75	100
θ_1^*, deg.	64.63	58.20	59.45	61.55	64.97
θ_2^*, deg.	-14.77	4.25	11.50	15.55	15.53
t/B	0.0900	0.0825	0.0750	0.0675	0.0600
Radius, ins. (m.)	24.0 (0.61)	25.5 (0.65)	27.0 (0.69)	28.5 (0.72)	30.0 (0.76)

TABLE I Cont'd

SPAN: 0%

STAGGER: 24.93°

X	Y SUCT.	Y PRES.
-.00762	.02122	.02122
-.00511	.03357	.00854
-.00261	.03965	.00363
-.00010	.04594	.00012
.00240	.05161	-.00262
.00491	.05749	-.00484
.00742	.06296	-.00666
.00993	.06822	-.00815
.01243	.07328	-.00937
.01493	.07814	-.01034
.01744	.08279	-.01109
.01994	.08724	-.01164
.02245	.09149	-.01198
.04450	.12282	-.01067
.06655	.15088	-.00536
.08860	.17712	.00143
.11064	.20165	.00970
.13269	.22550	.01896
.15474	.24847	.02897
.17679	.27096	.03927
.19884	.29298	.04983
.22089	.31455	.06053
.24294	.33567	.07132
.26499	.35634	.08219
.28704	.37657	.09309
.30908	.39637	.10401
.33113	.41575	.11491
.35318	.43474	.12578
.50437	.55603	.19964
.65557	.66449	.26934
.80676	.76175	.33572
.95795	.84930	.39807
1.10914	.92831	.45605
1.26033	.99956	.50939
1.41153	1.06347	.55791
1.56272	1.12005	.60211
1.71391	1.16960	.64226
1.86510	1.21274	.67826
2.01629	1.24978	.71006
2.16749	1.28072	.73772
2.31868	1.30554	.76139
2.46987	1.32430	.78133
2.62106	1.33707	.79708
2.77225	1.34392	.81042
2.92344	1.34491	.81952
3.07464	1.34013	.82495
3.22583	1.32956	.82608
3.37702	1.31313	.82466
3.52821	1.29074	.81868
3.67940	1.26233	.80927
3.83059	1.22791	.79561
3.98179	1.18758	.77750
4.13298	1.14147	.75457
4.28417	1.08968	.72643
4.43536	1.03214	.69287
4.58655	.96868	.65365
4.73774	.89909	.60918
4.88894	.82319	.55863
5.04013	.74060	.50237
5.19132	.65079	.43924
5.34251	.55327	.36866
5.49370	.44754	.29074
5.64489	.33339	.20470
5.66694	.31604	.19149
5.68899	.29851	.17811
5.71104	.28060	.16457
5.73309	.26291	.15065
5.75513	.24485	.13647
5.77718	.22660	.12292
5.79923	.20816	.10870
5.82128	.18957	.09452
5.84333	.17079	.07976
5.86537	.15183	.06504
5.88742	.13269	.05015
5.90947	.11337	.03509
5.93152	.09367	.01966
5.95357	.07419	.00446
5.97561	.05434	-.00856
5.97812	.05207	-.00895
5.98063	.04980	-.00908
5.98313	.04753	-.00897
5.98564	.04525	-.00860
5.98814	.04298	-.00796
5.99065	.04070	-.00703
5.99315	.03842	-.00577
5.99566	.03613	-.00413
5.99816	.03383	-.00199
6.00067	.03099	.00065
6.00317	.02692	.00492
6.00572	.01592	.01592

TABLE I Cont'd

SPAN: 25%

STAGGER: 31.2°

X	Y SUCT.	Y PRES.
-.00301	.01259	.01259
-.00051	.02370	.00105
.00200	.02653	-.00334
.00450	.03319	-.00643
.00700	.03768	-.00874
.00950	.04199	-.01065
.01201	.04614	-.01212
.01451	.05012	-.01317
.01701	.05393	-.01413
.01951	.05756	-.01486
.02201	.06103	-.01553
.02452	.06433	-.01615
.02702	.06745	-.01671
.04904	.08988	-.01937
.07106	.10955	-.01856
.09308	.12771	-.01599
.11510	.14466	-.01233
.13712	.16076	-.00790
.15914	.17641	-.00294
.18116	.19180	.00230
.20318	.20693	.00772
.22520	.22179	.01328
.24722	.23638	.01896
.26924	.25070	.02474
.29126	.26473	.03059
.31328	.27848	.03648
.33530	.29195	.04240
.35732	.30516	.04834
.50832	.39002	.08923
.65931	.46671	.12968
.81031	.53604	.16862
.96130	.59989	.20635
1.11229	.65601	.24190
1.26329	.70797	.27466
1.41428	.75493	.30508
1.56528	.79663	.33298
1.71627	.83315	.35874
1.86727	.86497	.38211
2.01826	.89233	.40295
2.16925	.91516	.42129
2.32025	.93341	.43723
2.47124	.94708	.45090
2.62224	.95616	.46238
2.77323	.96071	.47165
2.92423	.96075	.47868

X	Y SUCT.	Y PRES.
3.07522	.95634	.48345
3.22621	.94747	.48593
3.37721	.93411	.48610
3.52820	.91621	.48394
3.67920	.89373	.47943
3.83019	.86676	.47238
3.98119	.83550	.46248
4.13218	.80013	.44945
4.28317	.76085	.43299
4.43417	.71768	.41297
4.58516	.67056	.38939
4.73616	.61939	.36219
4.88715	.56409	.33140
5.03815	.50461	.29683
5.18914	.44090	.25830
5.34013	.37291	.21556
5.49113	.30060	.16844
5.64212	.22394	.11687
5.66414	.21240	.10897
5.68616	.20077	.10098
5.70818	.18904	.09290
5.73020	.17722	.08472
5.75222	.16531	.07645
5.77424	.15331	.06808
5.79626	.14122	.05962
5.81828	.12903	.05106
5.84030	.11675	.04241
5.86232	.10438	.03367
5.88434	.09191	.02482
5.90636	.07936	.01589
5.92838	.06671	.00686
5.95039	.05397	-.00227
5.97241	.04113	-.01141
5.97492	.03967	-.01207
5.97742	.03820	-.01245
5.97992	.03674	-.01255
5.98242	.03527	-.01237
5.98492	.03380	-.01191
5.98742	.03233	-.01116
5.98992	.03086	-.01007
5.99243	.02934	-.00860
5.99493	.02737	-.00668
5.99743	.02472	-.00398
5.99993	.02087	-.00013
6.00248	.01037	.01037

TABLE I Cont'd

SPAN: 50%

STAGGER: 35.5°

X	Y SUCT.	Y PRES.
-.00195	.00922	.00922
.00055	.01928	-.00116
.00305	.02365	-.00503
.00556	.02786	-.00769
.00806	.03192	-.00965
.01056	.03582	-.01112
.01306	.03956	-.01221
.01556	.04315	-.01311
.01806	.04657	-.01395
.02057	.04984	-.01473
.02307	.05296	-.01544
.02557	.05591	-.01610
.02807	.05871	-.01670
.05008	.07864	-.01932
.07210	.09611	-.01864
.09411	.11218	-.01645
.11612	.12709	-.01331
.13814	.14122	-.00948
.16015	.15496	-.00520
.18217	.16849	-.00070
.20418	.18180	.00396
.22619	.19490	.00876
.24821	.20778	.01366
.27022	.22043	.01866
.29223	.23283	.02371
.31425	.24499	.02881
.33626	.25691	.03392
.35827	.26861	.03905
.50923	.34389	.07445
.66018	.41209	.10957
.81113	.47361	.14374
.96208	.52985	.17663
1.11303	.58090	.20782
1.26398	.62748	.23673
1.41493	.66972	.26319
1.56588	.70726	.28769
1.71683	.74013	.31038
1.86778	.76876	.33101
2.01873	.79338	.34946
2.16968	.81394	.36571
2.32063	.83040	.37984
2.47158	.84275	.39195
2.62253	.85100	.40209
2.77348	.85515	.41027
2.92443	.85524	.41647
3.07538	.85127	.42069
3.22633	.84324	.42292
3.37728	.83114	.42314
3.52823	.81494	.42132
3.67919	.79461	.41743
3.83014	.77026	.41130
3.98109	.74206	.40269
4.13204	.71022	.39131
4.28299	.67490	.37692
4.43394	.63616	.35941
4.58489	.59393	.33877
4.73584	.54814	.31501
4.88679	.49871	.28810
5.03774	.44564	.25793
5.18869	.38892	.22432
5.33964	.32857	.18709
5.49059	.26461	.14606
5.64154	.19702	.10119
5.66355	.18687	.09433
5.68557	.17663	.08738
5.70758	.16632	.08035
5.72960	.15593	.07324
5.75161	.14546	.06604
5.77362	.13492	.05877
5.79564	.12430	.05141
5.81765	.11361	.04397
5.83966	.10283	.03645
5.86168	.09198	.02885
5.88369	.08106	.02117
5.90570	.07005	.01340
5.92772	.05897	.00555
5.94973	.04781	-.00236
5.97175	.03658	-.01039
5.97425	.03530	-.01130
5.97675	.03401	-.01198
5.97925	.03273	-.01234
5.98175	.03145	-.01239
5.98425	.03016	-.01214
5.98675	.02887	-.01158
5.98926	.02759	-.01068
5.99176	.02624	-.00938
5.99426	.02446	-.00760
5.99676	.02200	-.00513
5.99926	.01836	-.00150
6.00178	.00843	.00843

TABLE I Cont'd

SPAN: 75%

STAGGER: 38.5°

X	Y SUCT.	Y PRES.
-.00144	.00712	.00712
.00106	.01610	-.00212
.00356	.02017	-.00546
.00606	.02409	-.00766
.00856	.02787	-.00920
.01107	.03149	-.01026
.01357	.03497	-.01115
.01607	.03831	-.01196
.01857	.04149	-.01275
.02107	.04452	-.01345
.02357	.04741	-.01409
.02607	.05015	-.01466
.02857	.05274	-.01517
.05058	.07121	-.01694
.07200	.08752	-.01571
.09461	.10252	-.01317
.11662	.11640	-.00977
.13863	.12955	-.00576
.16064	.14233	-.00136
.18265	.15494	.00323
.20466	.16737	.00796
.22667	.17962	.01281
.24868	.19167	.01774
.27069	.20352	.02275
.29270	.21516	.02761
.31471	.22657	.03290
.33672	.23777	.03800
.35873	.24876	.04310
.50966	.31968	.07811
.66059	.38407	.11206
.81153	.44237	.14625
.96246	.49537	.17855
1.11339	.54376	.20911
1.26432	.58804	.23734
1.41525	.62828	.26312
1.56618	.66409	.28694
1.71711	.69544	.30900
1.86804	.72276	.32905
2.01897	.74627	.34697
2.16990	.76592	.36273
2.32083	.78172	.37637
2.47176	.79365	.38798
2.62269	.80173	.39756
2.77362	.80594	.40521
2.92455	.80628	.41066

X	Y SUCT.	Y PRES.
3.07546	.80276	.41458
3.22641	.79536	.41634
3.37734	.78408	.41613
3.52827	.76890	.41396
3.67920	.74982	.40963
3.83013	.72693	.40317
3.98106	.70041	.39427
4.13199	.67042	.38272
4.28292	.63713	.36627
4.43385	.60058	.35065
4.56478	.56069	.33044
4.73571	.51740	.30716
4.88665	.47064	.28071
5.03758	.42040	.25126
5.16851	.36670	.21854
5.33944	.30958	.18239
5.49037	.24907	.14262
5.64130	.18517	.09919
5.66331	.17557	.09254
5.68532	.16590	.08563
5.70733	.15615	.07903
5.72934	.14634	.07216
5.75135	.13645	.06520
5.77336	.12649	.05817
5.79537	.11645	.05106
5.81738	.10635	.04368
5.83939	.09617	.03661
5.86140	.08592	.02927
5.88341	.07560	.02165
5.90542	.06521	.01435
5.92743	.05475	.00678
5.94944	.04421	-.00088
5.97145	.03360	-.00861
5.97395	.03239	-.00949
5.97645	.03118	-.01038
5.97895	.02997	-.01108
5.98145	.02876	-.01142
5.98395	.02754	-.01142
5.98645	.02633	-.01109
5.98895	.02511	-.01040
5.99145	.02389	-.00931
5.99395	.02231	-.00773
5.99645	.02006	-.00548
5.99895	.01669	-.00210
6.00147	.00729	.00729

TABLE I Cont'd

SPAN: 100%

STAGGER: 40.25°

X	Y SUCT.	Y PRES.
-.00157	.00697	.00697
.00097	.01575	-.00161
.00348	.01888	-.00493
.00598	.02089	-.00695
.00848	.02239	-.00851
.01098	.02385	-.00917
.01348	.02532	-.00961
.01598	.02678	-.00968
.01848	.02825	-.00936
.02098	.02971	-.00865
.02349	.03117	-.00761
.02599	.03263	-.00698
.02849	.03408	-.00614
.05050	.04683	.00119
.07251	.05947	.00845
.09452	.07198	.01565
.11653	.08437	.02280
.13854	.09665	.02969
.16055	.10881	.03691
.18257	.12084	.04368
.20458	.13276	.05079
.22659	.14456	.05764
.24860	.15624	.06443
.27061	.16781	.07116
.29262	.17925	.07764
.31463	.19057	.08445
.33664	.20178	.09100
.35866	.21287	.09750
.50959	.28561	.14046
.66052	.35354	.18071
.81146	.41630	.21829
.96239	.47423	.25322
1.11332	.52749	.28554
1.26426	.57620	.31527
1.41519	.62050	.34244
1.56612	.66046	.36708
1.71706	.69618	.38919
1.86799	.72775	.40860
2.01892	.75524	.42592
2.16986	.77870	.44058
2.32079	.79817	.45277
2.47172	.81371	.46251
2.62265	.82534	.46982
2.77359	.83307	.47468
2.92452	.83693	.47711

X	Y SUCT.	Y PRES.
3.07545	.83693	.47711
3.22639	.83307	.47468
3.37732	.82534	.46982
3.52825	.81371	.46252
3.67919	.79818	.45277
3.83012	.77871	.44058
3.98105	.75525	.42593
4.13199	.72776	.40860
4.28292	.69619	.38919
4.43385	.66046	.36708
4.58479	.62050	.34245
4.73572	.57621	.31528
4.88665	.52750	.28554
5.03759	.47424	.25323
5.18852	.41631	.21829
5.33945	.35355	.18072
5.49039	.28582	.14047
5.64132	.21288	.09750
5.66333	.20179	.09100
5.68534	.19058	.08445
5.70735	.17926	.07763
5.72936	.16781	.07116
5.75137	.15625	.06443
5.77339	.14457	.05763
5.79540	.13277	.05076
5.81741	.12085	.04367
5.83942	.10881	.03691
5.86143	.09665	.02968
5.88344	.08437	.02279
5.90545	.07198	.01564
5.92746	.05946	.00844
5.94947	.04683	.00117
5.97148	.03408	-.00615
5.97398	.03262	-.00699
5.97648	.03116	-.00762
5.97898	.02970	-.00806
5.96148	.02824	-.00937
5.96398	.02678	-.00969
5.96649	.02532	-.00963
5.98899	.02385	-.00919
5.99149	.02238	-.00834
5.99399	.02089	-.00699
5.99649	.01888	-.00498
5.99899	.01578	-.00167
6.00152	.00695	.00695

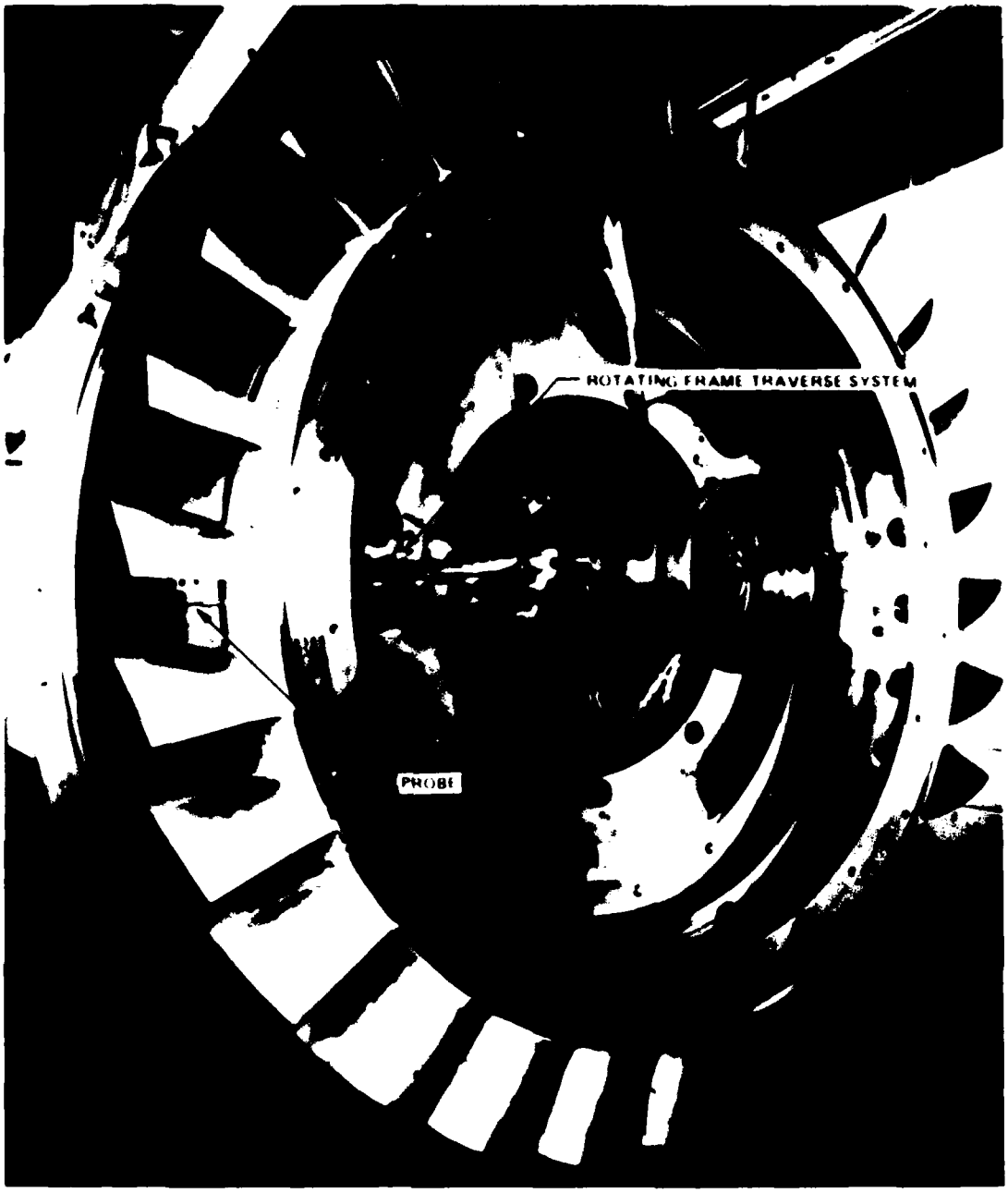

Figure 1. Isolated Compressor Rotor with Rotating Frame Traverse System

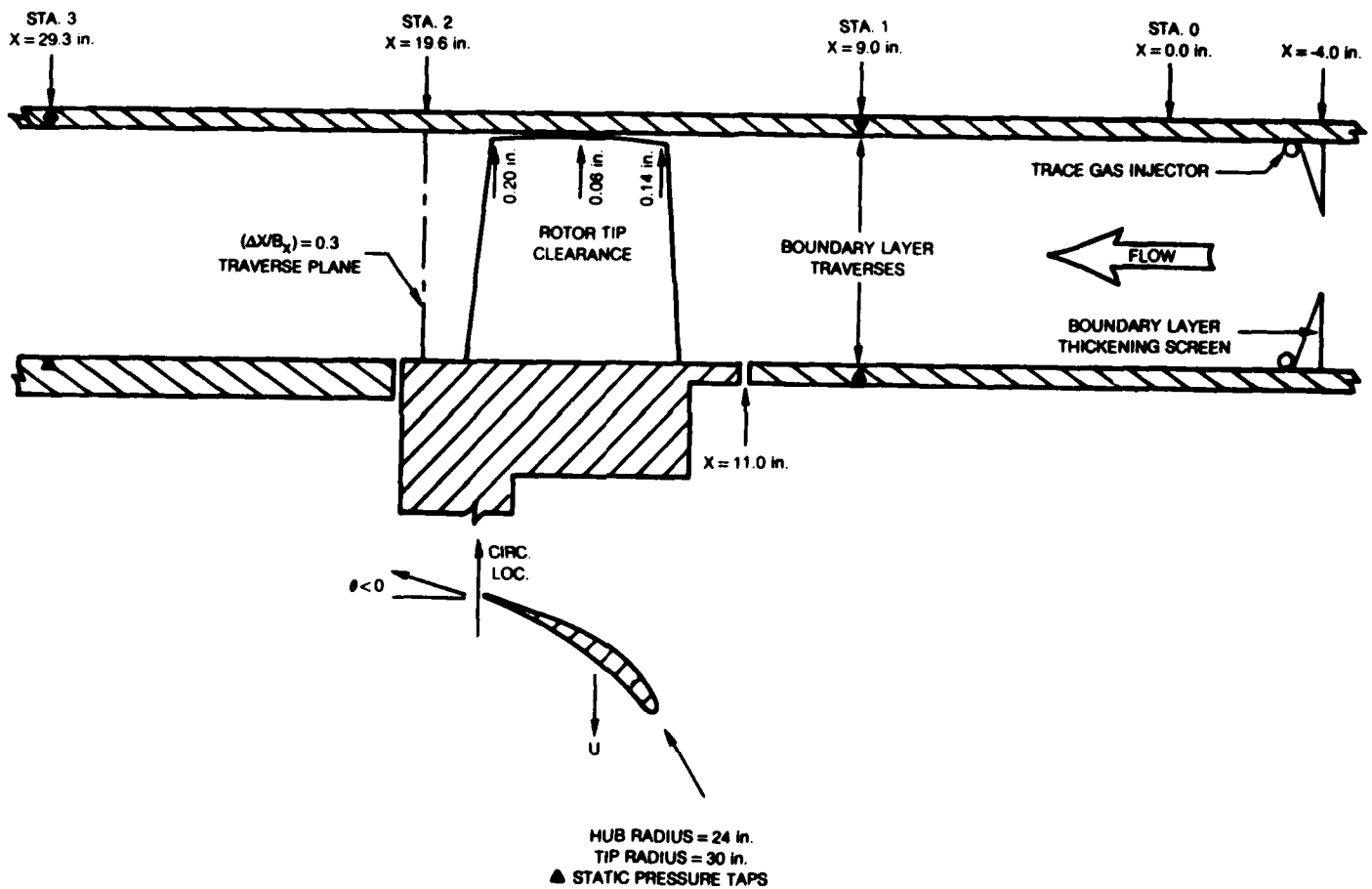

Figure 2. Flow Path Schematic

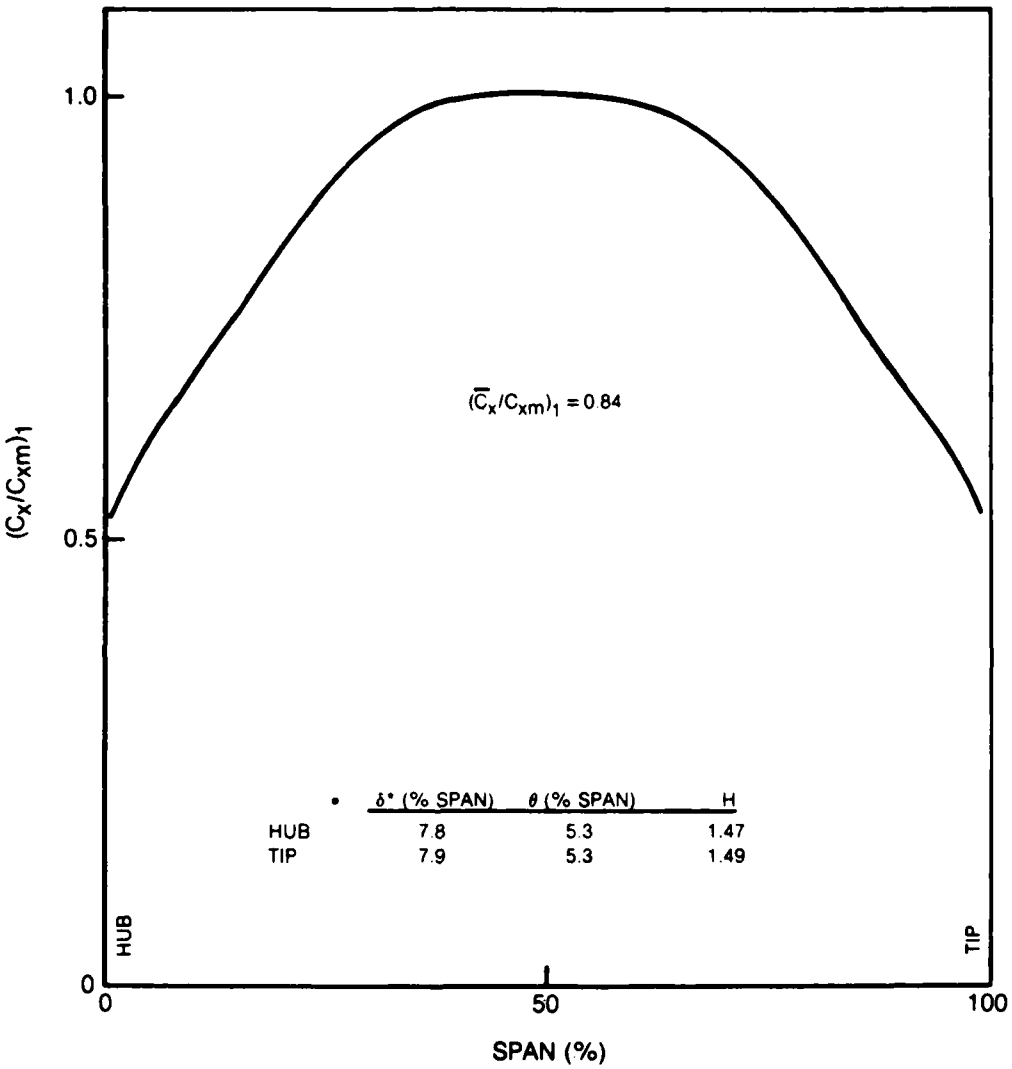

Figure 3. Inlet Velocity Profile at Sta. 1

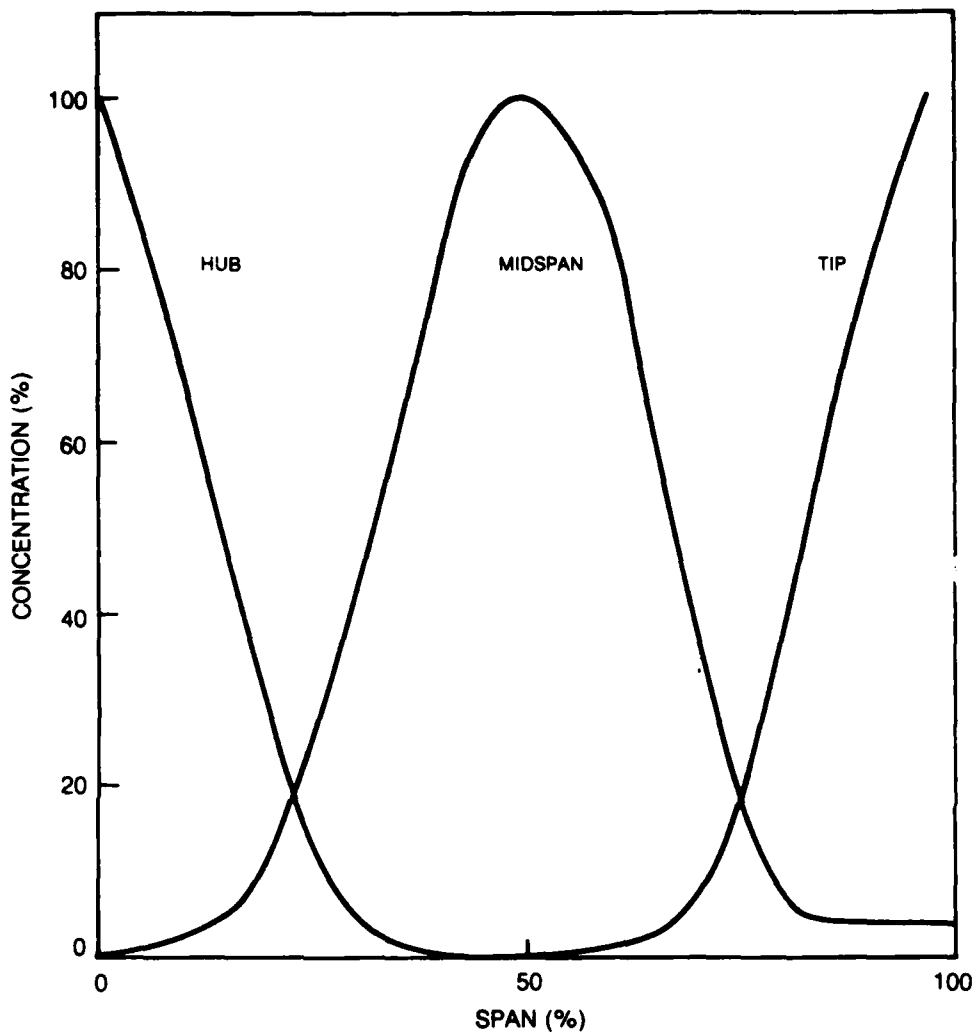

Figure 4. Inlet Trace Gas Concentration Profiles at Sta. 1

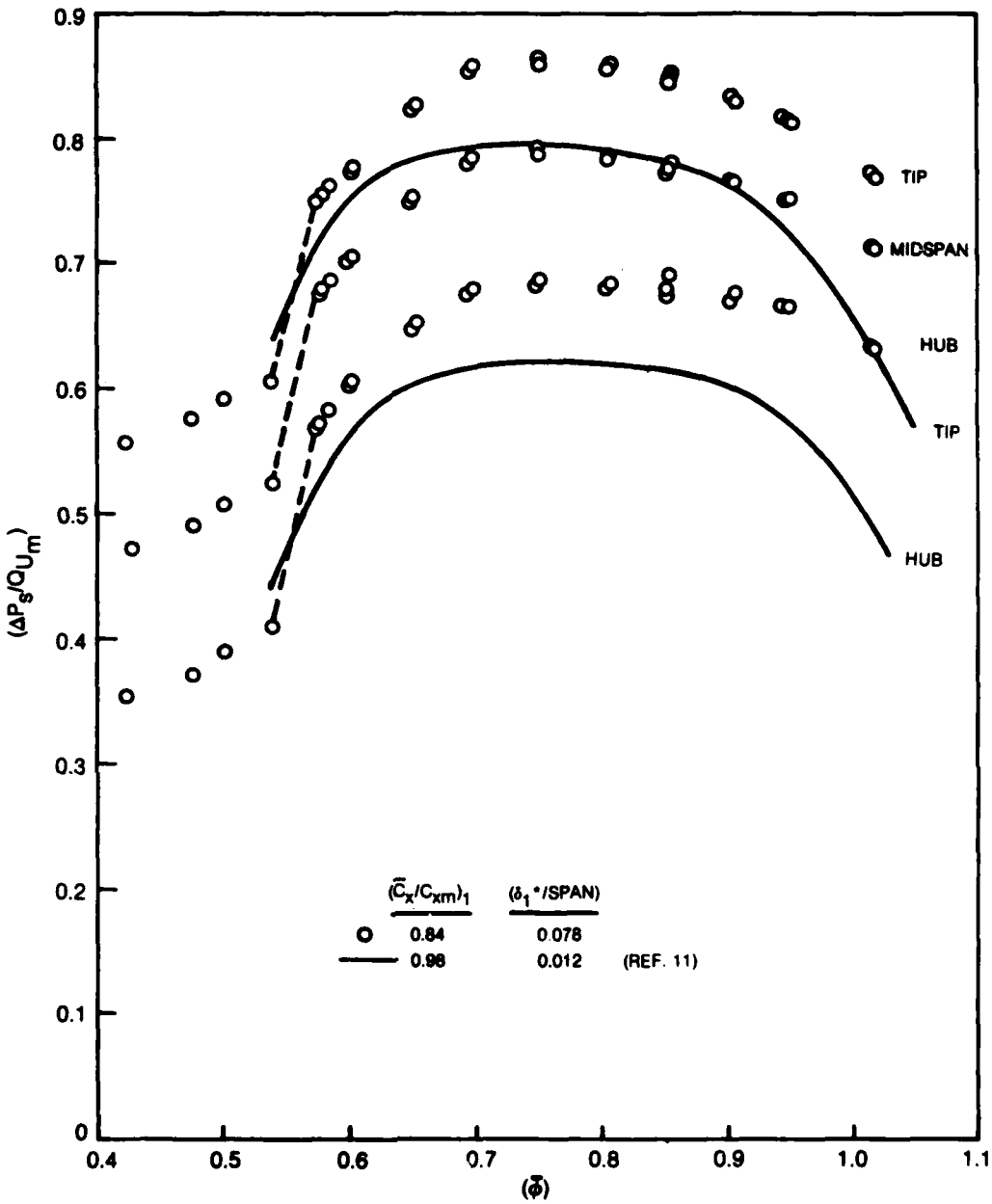

Figure 5. Rotor Static Pressure Rise Characteristic

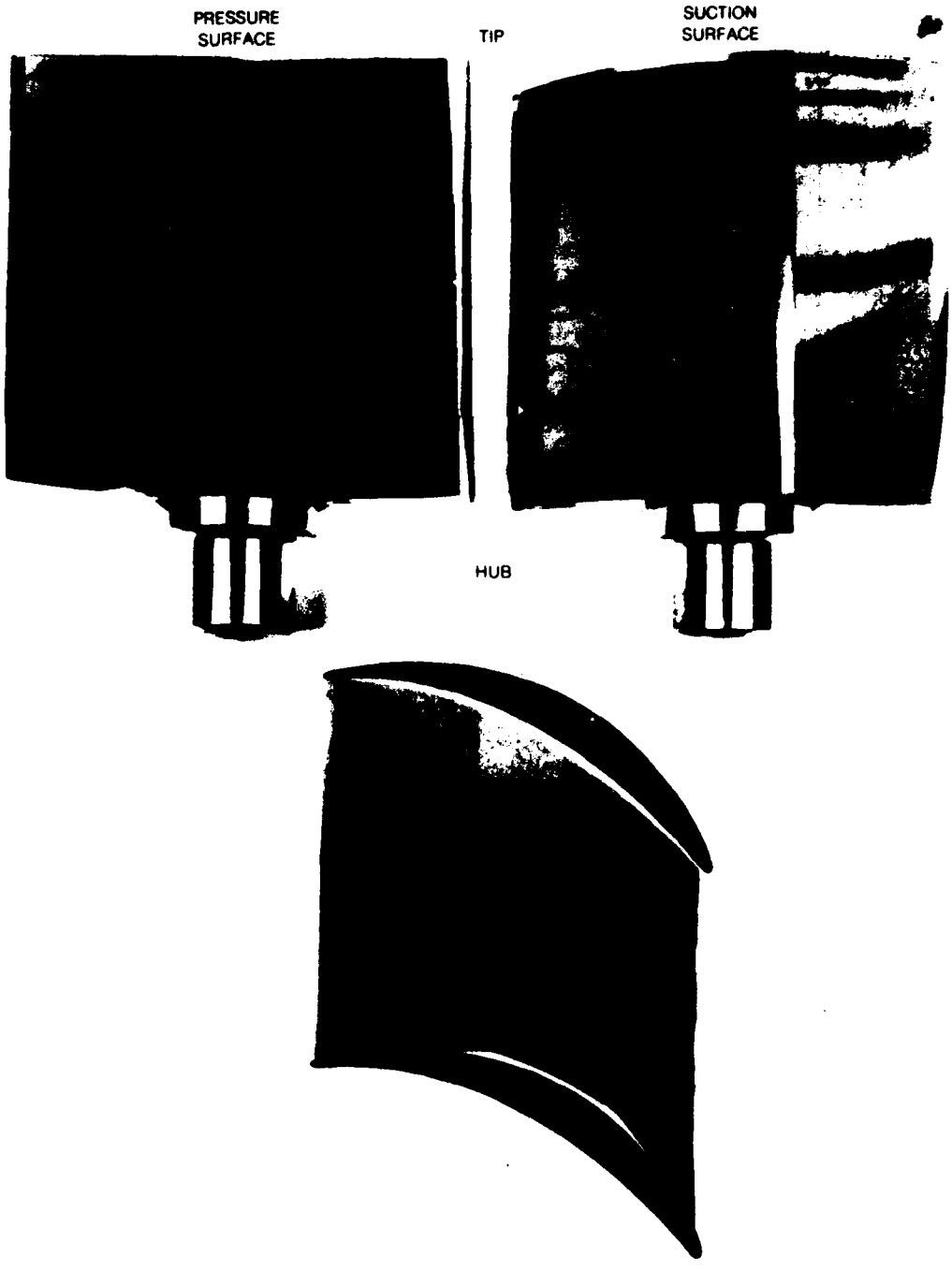

Figure 6. Airfoil Passage Flow Visualization, $\bar{\phi}$ = 0.95

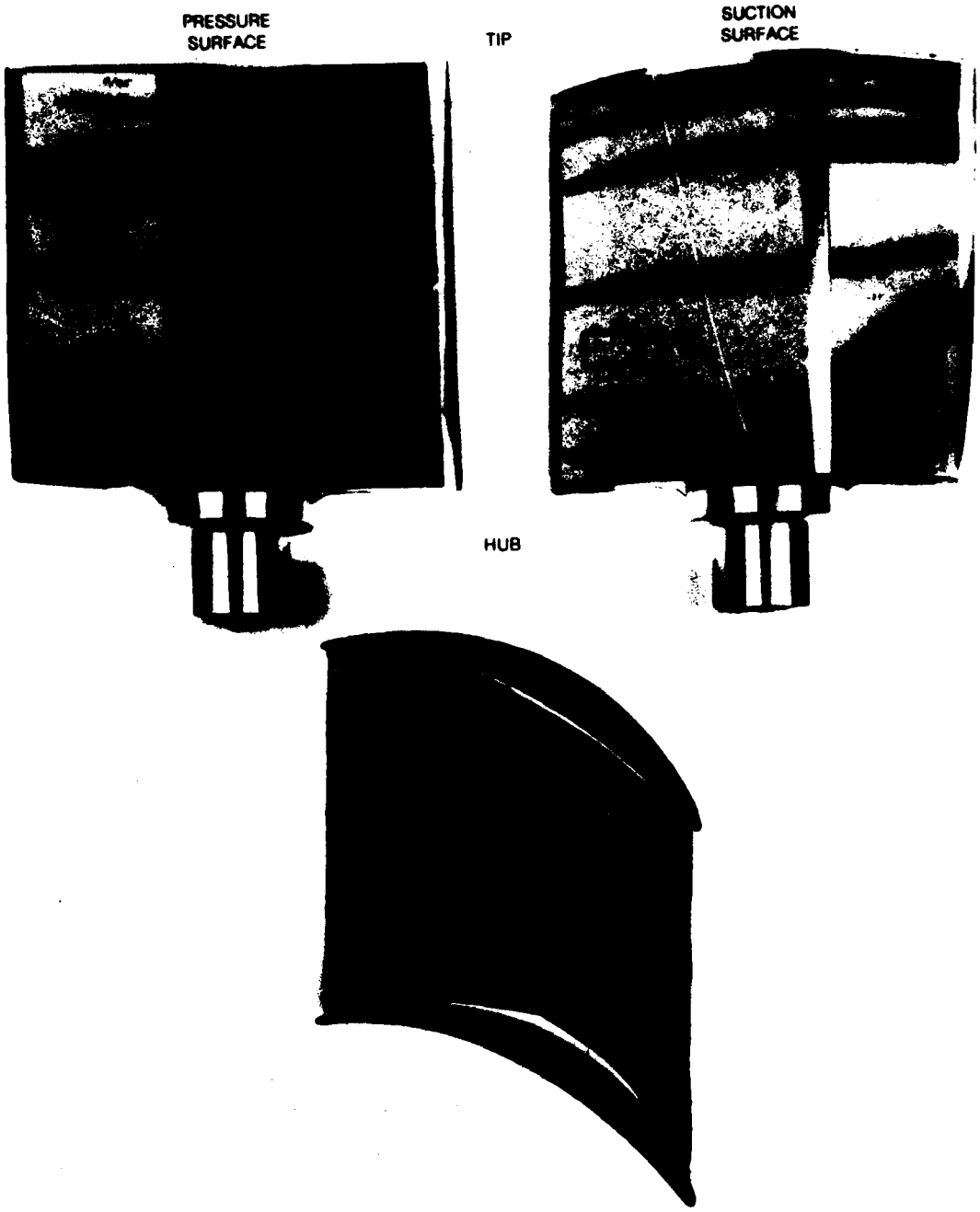

Figure 7. Airfoil Passage Flow Visualization, $\bar{\phi}$ = 0.85

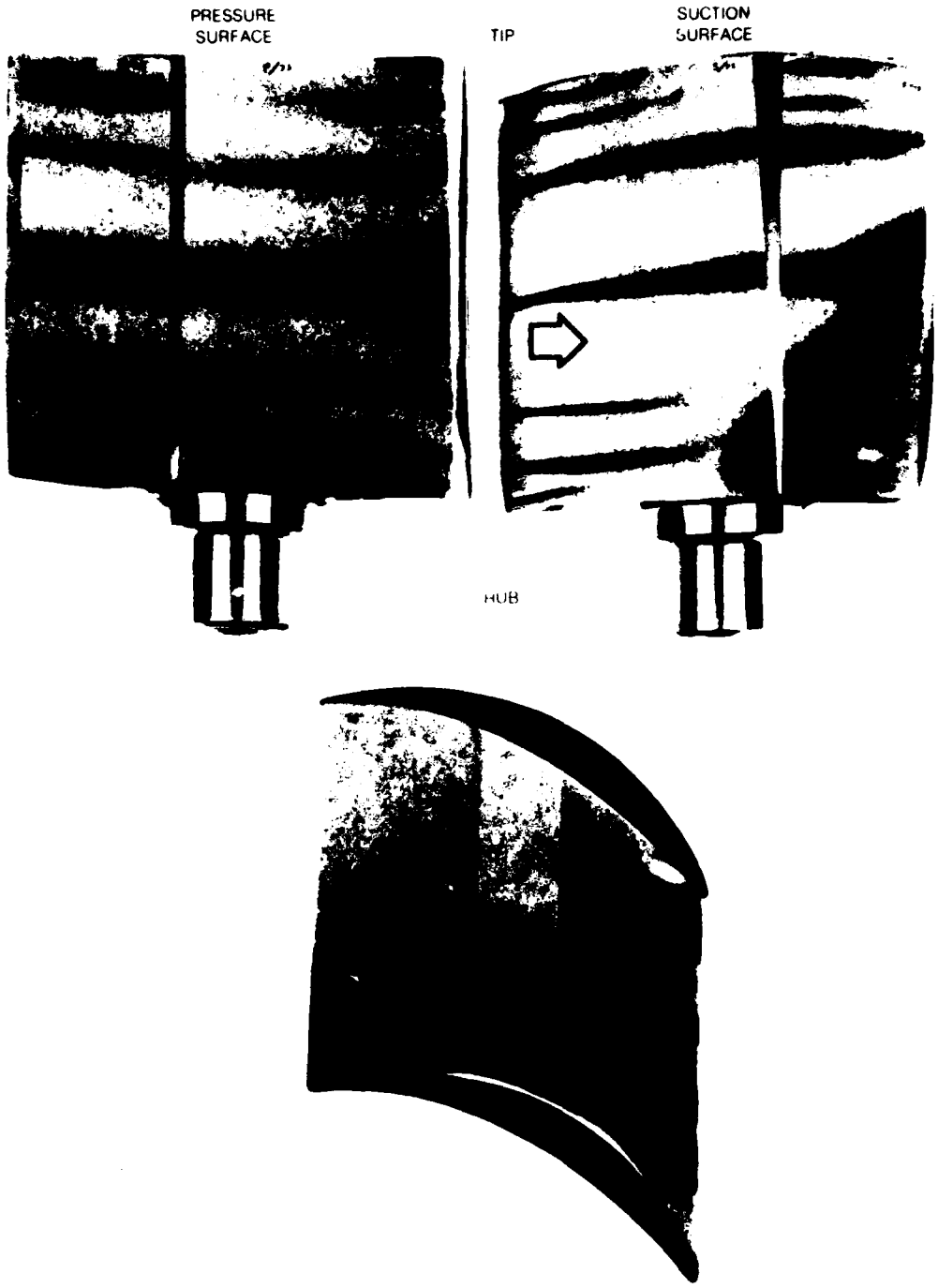

Figure 8. Airfoil Passage Flow Visualization, $\bar{\phi}$ = 0.75

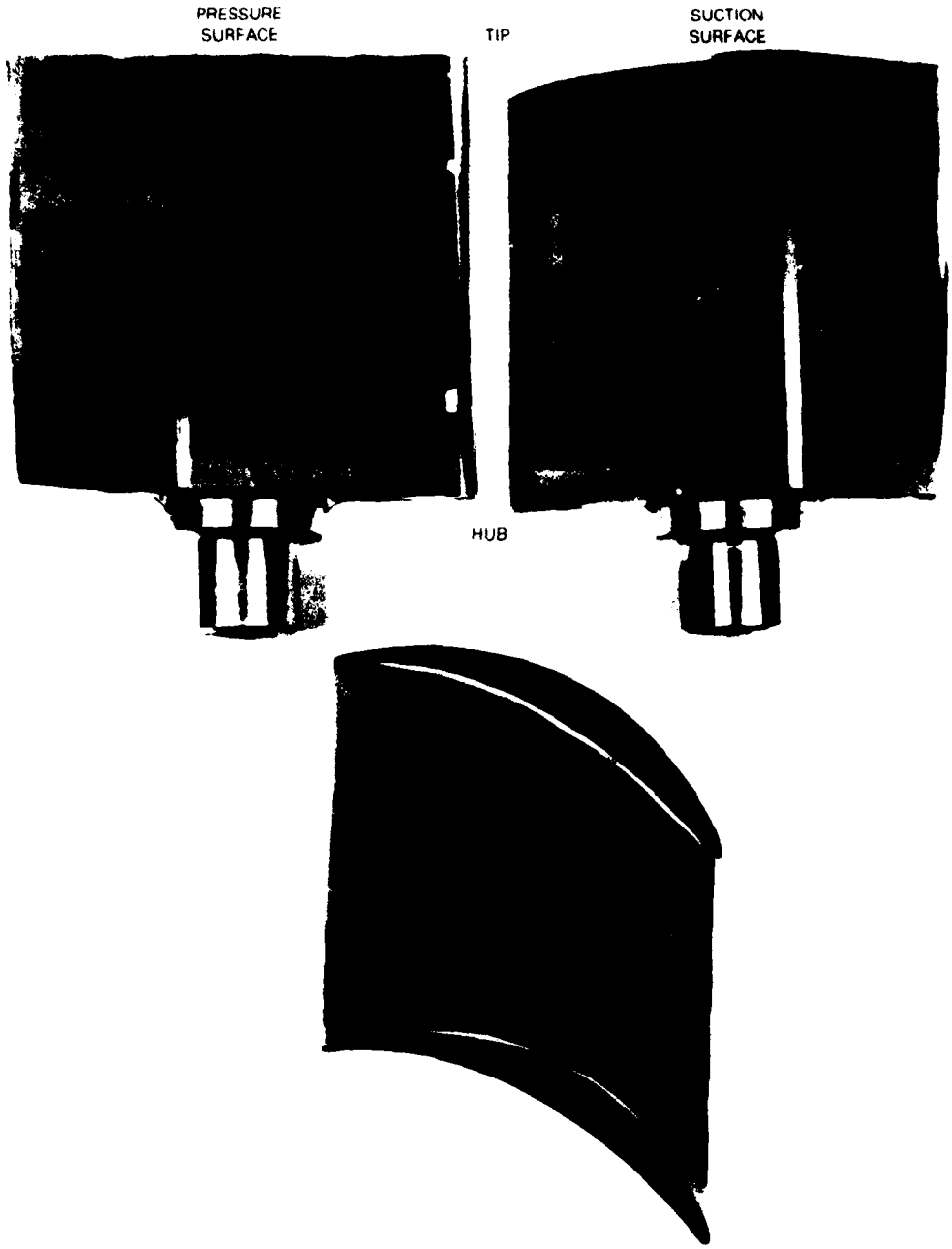

Figure 9. Airfoil Passage Flow Visualization, $\bar{\phi}$ = 0.65

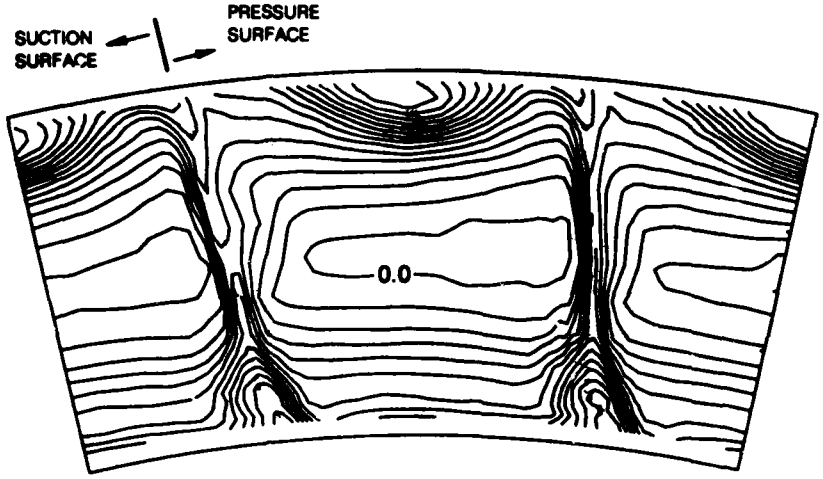

a) ROTARY TOTAL PRESSURE
CONTOUR INCREMENT: $\Delta C_{PT} = 0.1$

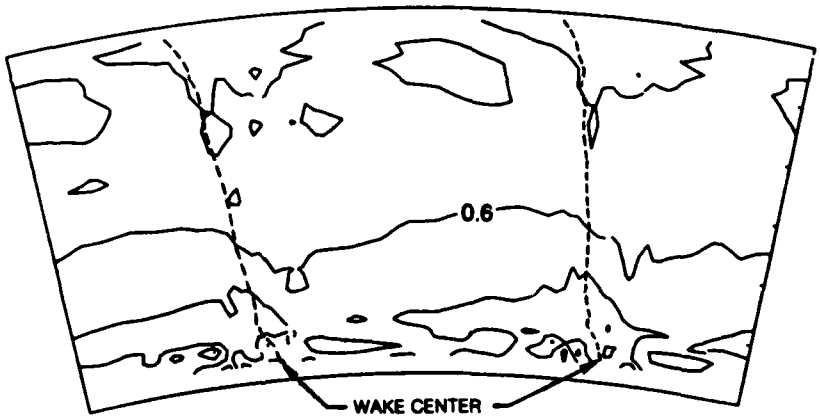

b) STATIC PRESSURE
CONTOUR INCREMENT: $\Delta C_{PS} = 0.05$

Figure 10. Relative Total and Static Pressure Contours, $\bar{\phi}$ = 0.95

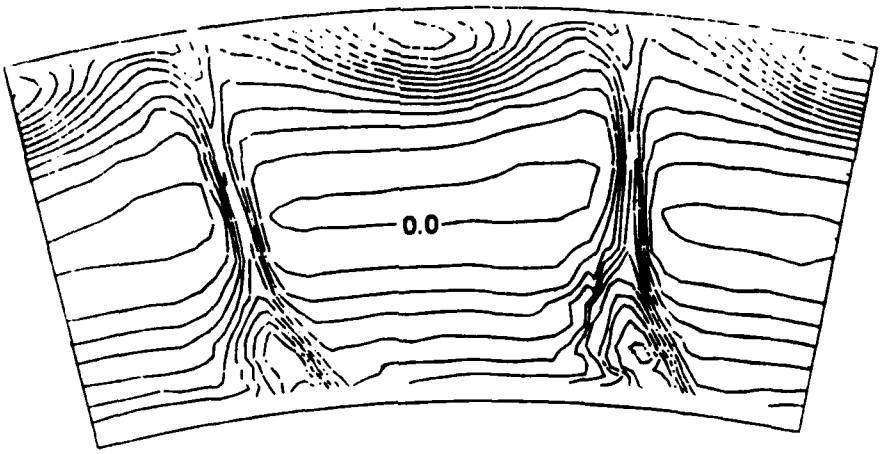

a) ROTARY TOTAL PESSURE
CONTOUR INCREMENT: $\Delta C_{PT} = 0.1$

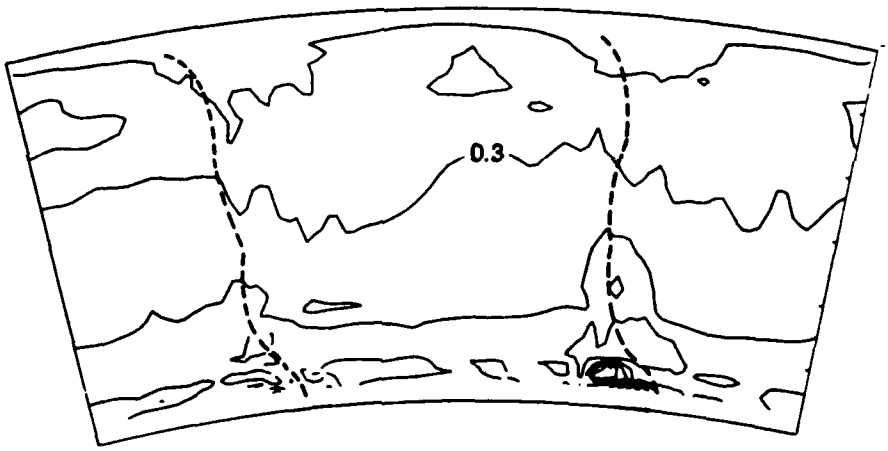

b) STATIC PRESSURE
CONTOUR INCREMENT: $\Delta C_{PS} = 0.05$

Figure 11. Relative Total and Static Pressure Contours, $\bar{\phi}$ = 0.85

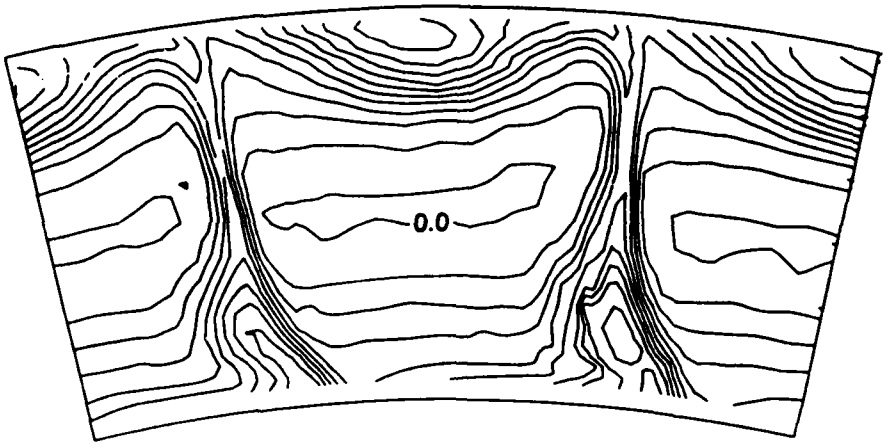

a) ROTARY TOTAL PRESSURE
CONTOUR INCREMENT: $\Delta C_{PT} = 0.1$

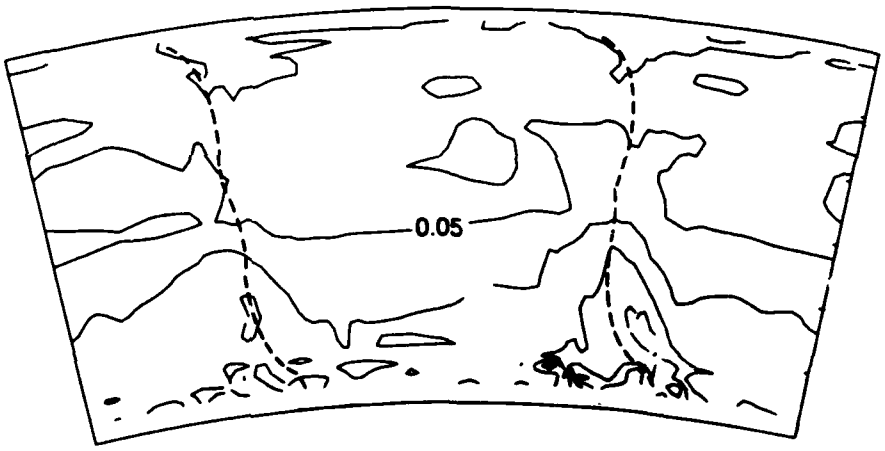

b) STATIC PRESSURE
CONTOUR INCREMENT: $\Delta C_{PS} = 0.05$

Figure 12. Relative Total and Static Pressure Contours, $\bar{\phi} = 0.75$

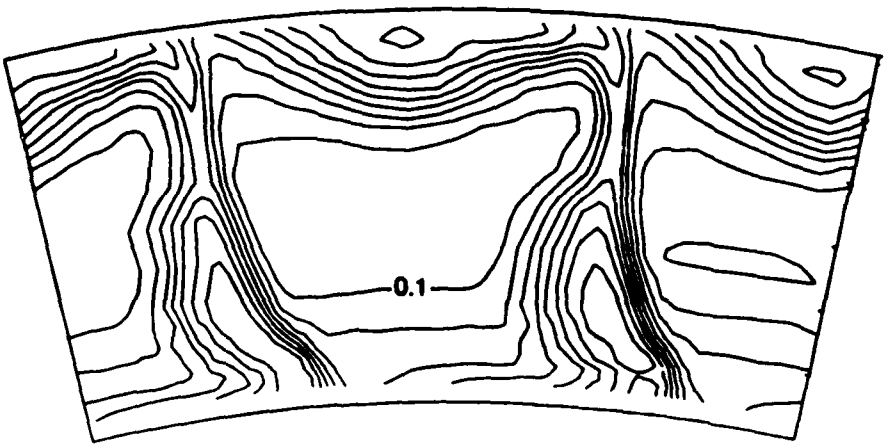

a) ROTARY TOTAL PRESSURE
CONTOUR INCREMENT: $\Delta C_{PT} = 0.1$

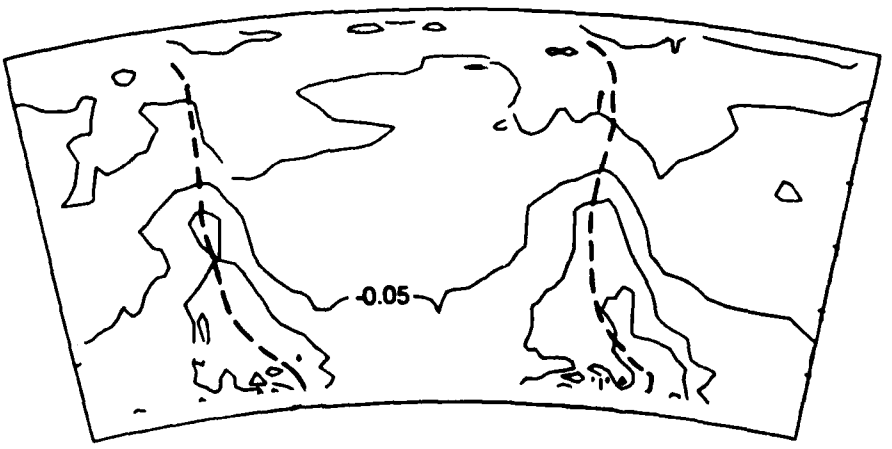

b) STATIC PRESSURE
CONTOUR INCREMENT: $\Delta C_{PS} = 0.05$

Figure 13. Relative Total and Static Pressure Contours, $\bar{\phi}$ = 0.65

1.32 PITCHES

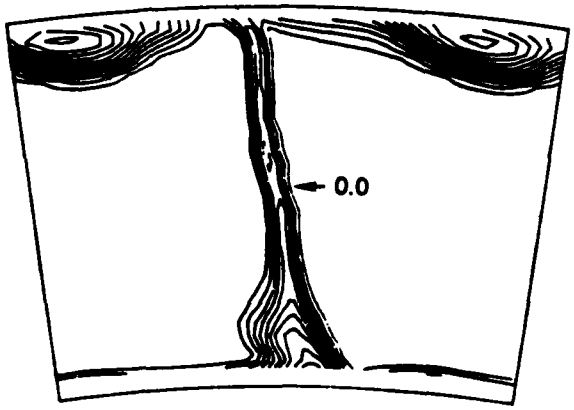

a) ROTARY TOTAL PRESSURE CONTOUR
INCREMENT: $\Delta C_{PT} = 0.1$

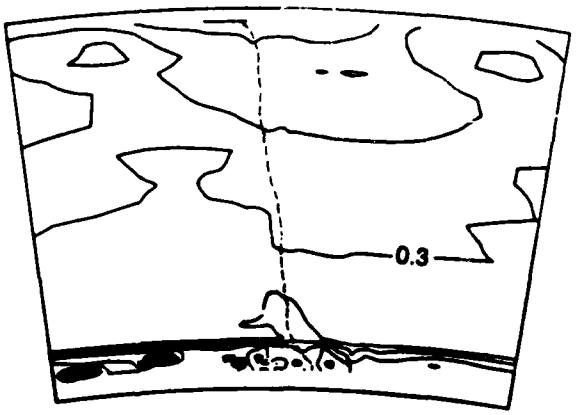

b) STATIC PRESSURE CONTOUR
INCREMENT: $\Delta C_{PS} = 0.05$

Figure 14. Relative Total and Static Pressure Contours, ϕ = 0.95

1.32 PITCHES

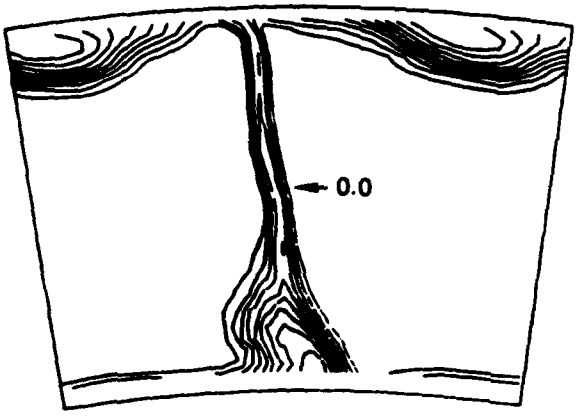

a) ROTARY TOTAL PRESSURE CONTOUR
INCREMENT: $\Delta C_{PT} = 0.1$

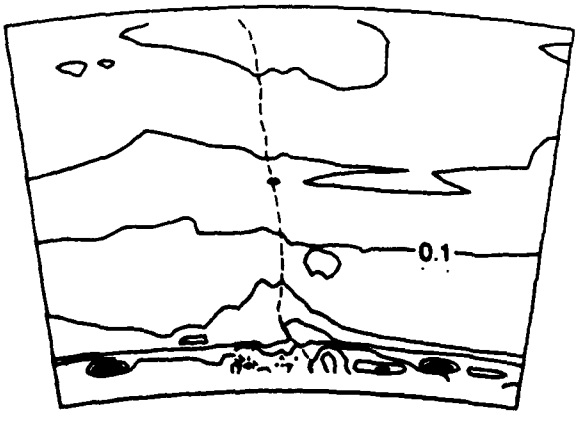

b) STATIC PRESSURE CONTOUR
INCREMENT: $\Delta C_{PS} = 0.05$

Figure 15. Relative Total and Static Pressure Contours, ϕ = 0.85

1.32 PITCHES

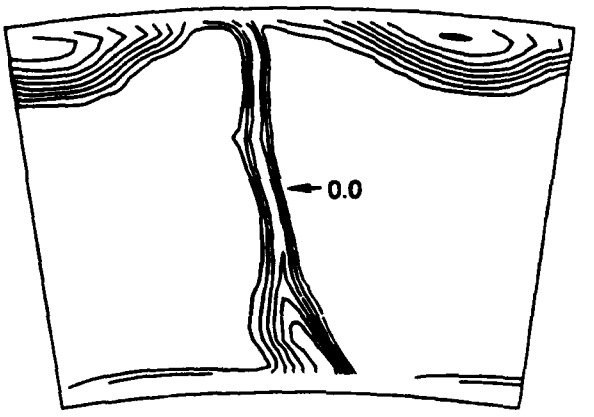

a) ROTARY TOTAL PRESSURE CONTOUR
INCREMENT: $\Delta C_{PT} = 0.1$

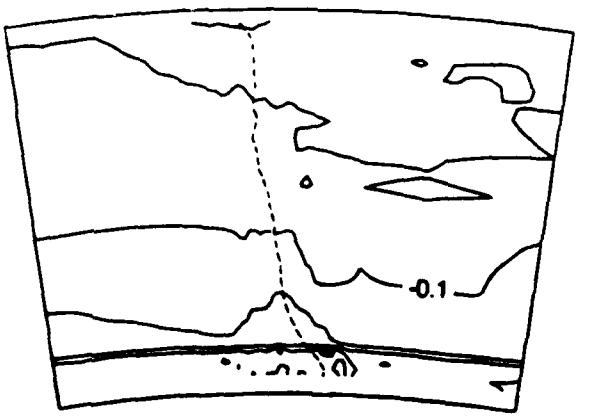

b) STATIC PRESSURE CONTOUR
INCREMENT: $\Delta C_{PS} = 0.05$

Figure 16. Relative Total and Static Pressure Contours, ϕ = 0.75

1.32 PITCHES

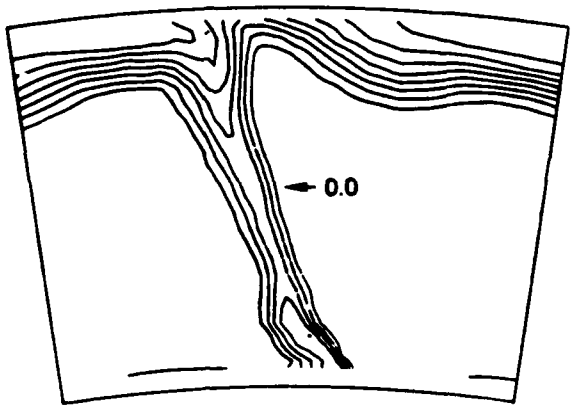

a) ROTARY TOTAL PRESSURE CONTOUR
INCREMENT: $\Delta C_{PT} = 0.1$

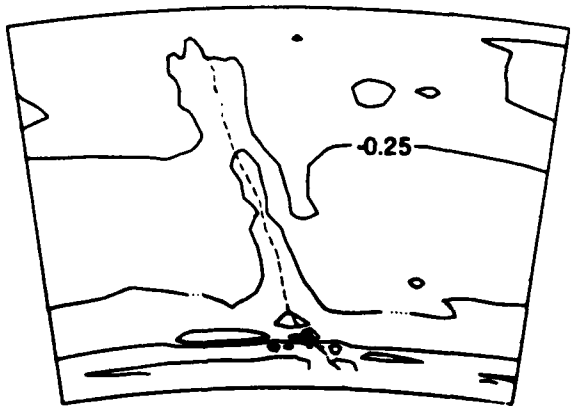

b) STATE PRESSURE CONTOUR
INCREMENT: $\Delta C_{PS} = 0.05$

Figure 17. Relative Total and Static Pressure Contours, ϕ = 0.65

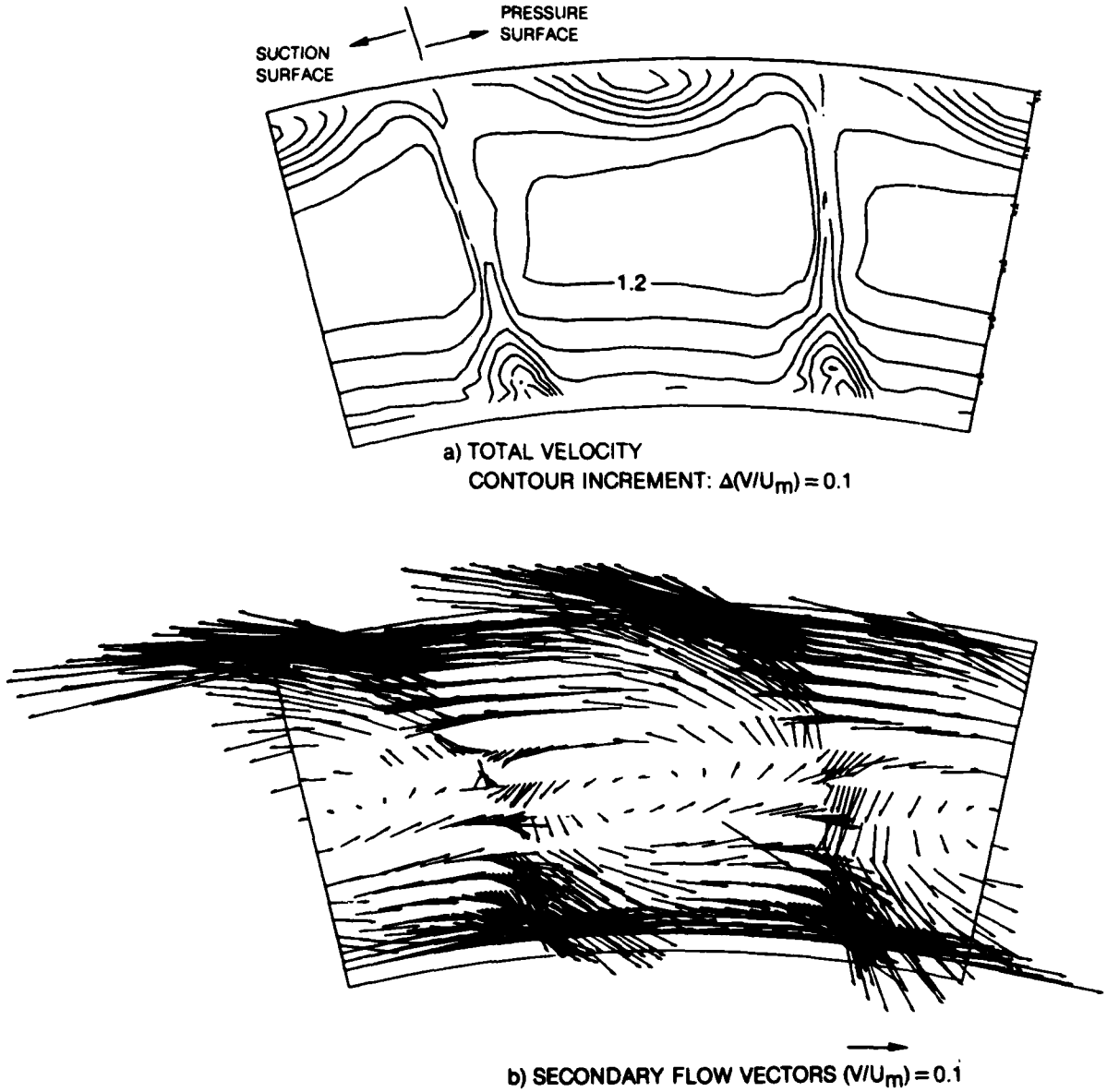

Figure 18. Relative Flow Speed Contours and Secondary Flow Vectors Relative to Core Flow, $\bar{\phi}$ = 0.95

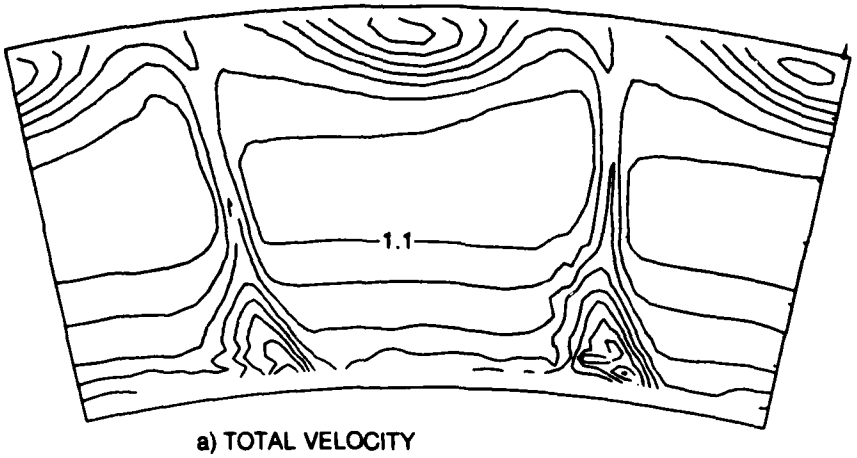

a) TOTAL VELOCITY
CONTOUR INCREMENT: $\Delta\ (V/U_m) = 0.1$

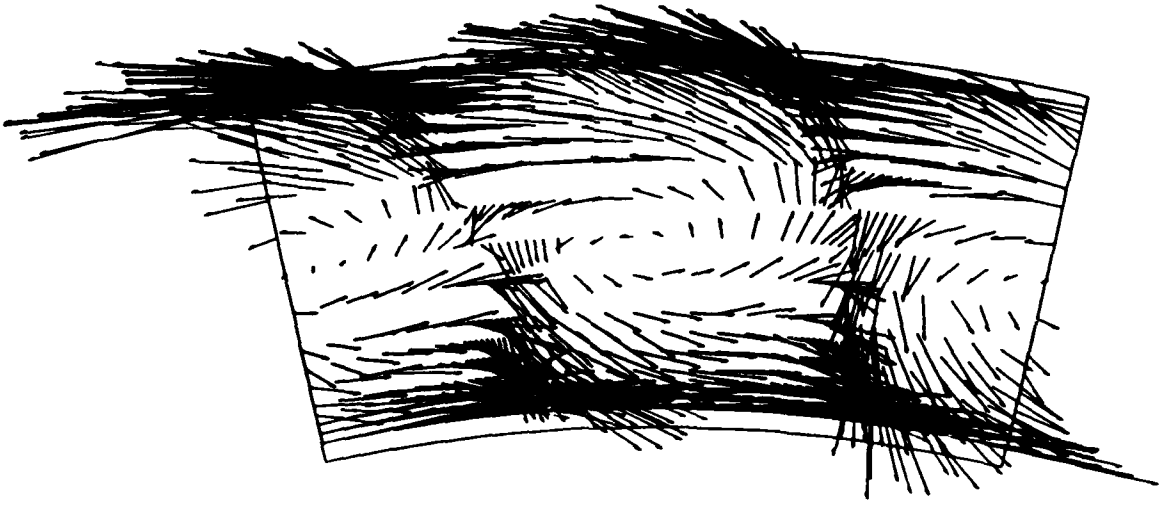

b) SECONDARY FLOW VECTORS $(V/U_m) = 0.1$

Figure 19. Relative Flow Speed Contours and Secondary Flow Vectors Relative to Core Flow, $\bar{\phi} = 0.85$

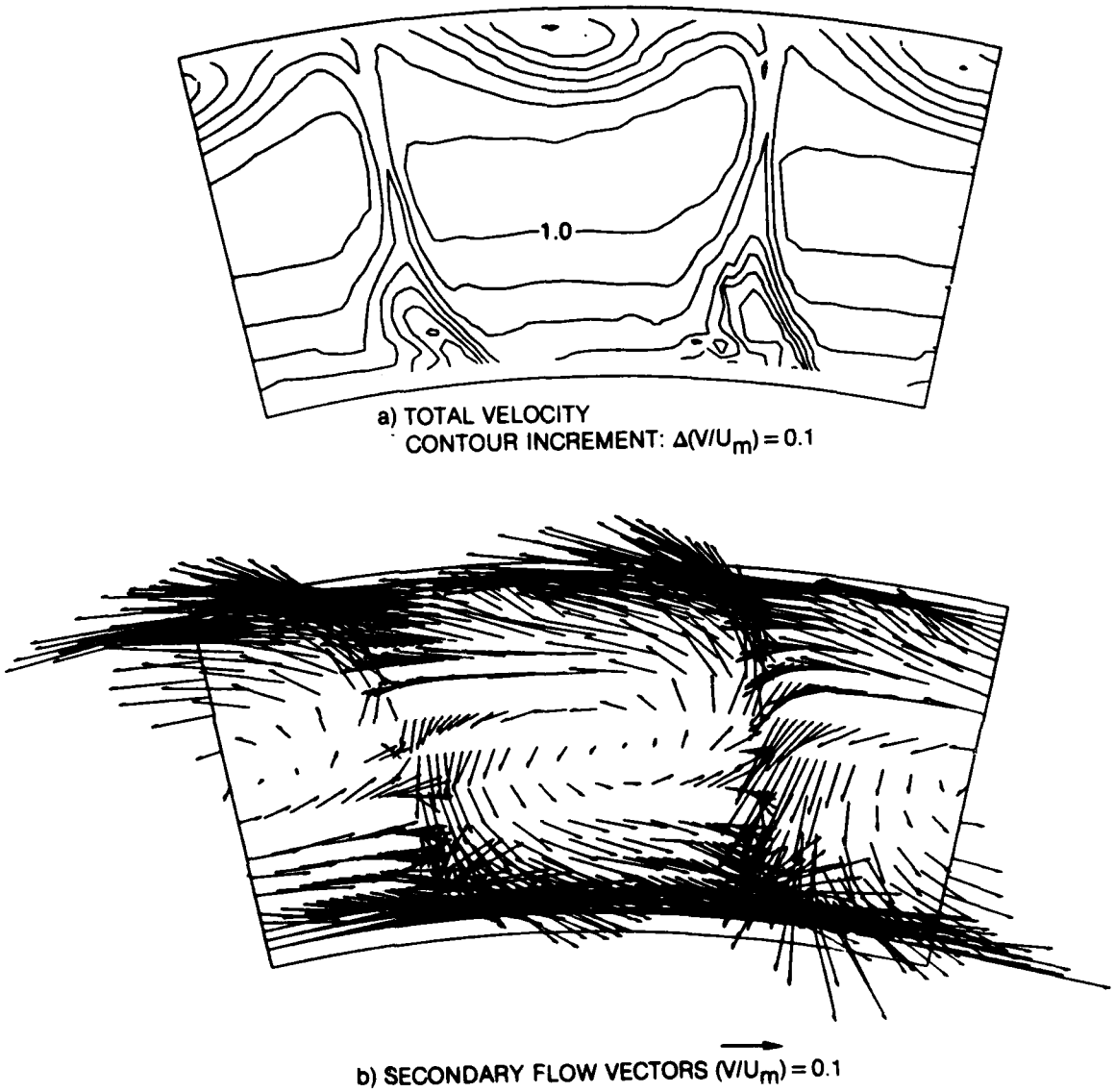

Figure 20. Relative Flow Speed Contours and Secondary Flow Vectors Relative to Core Flow, $\bar{\phi} = 0.75$

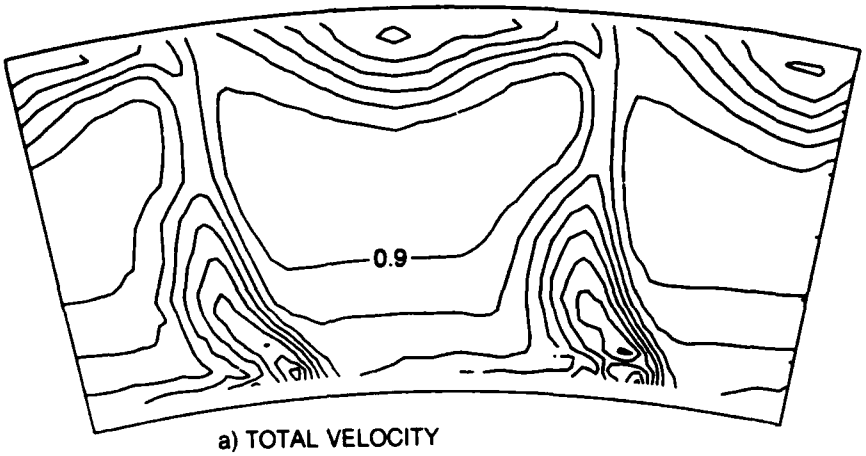

a) TOTAL VELOCITY
CONTOUR INCREMENT: $\Delta(V/U_m) = 0.1$

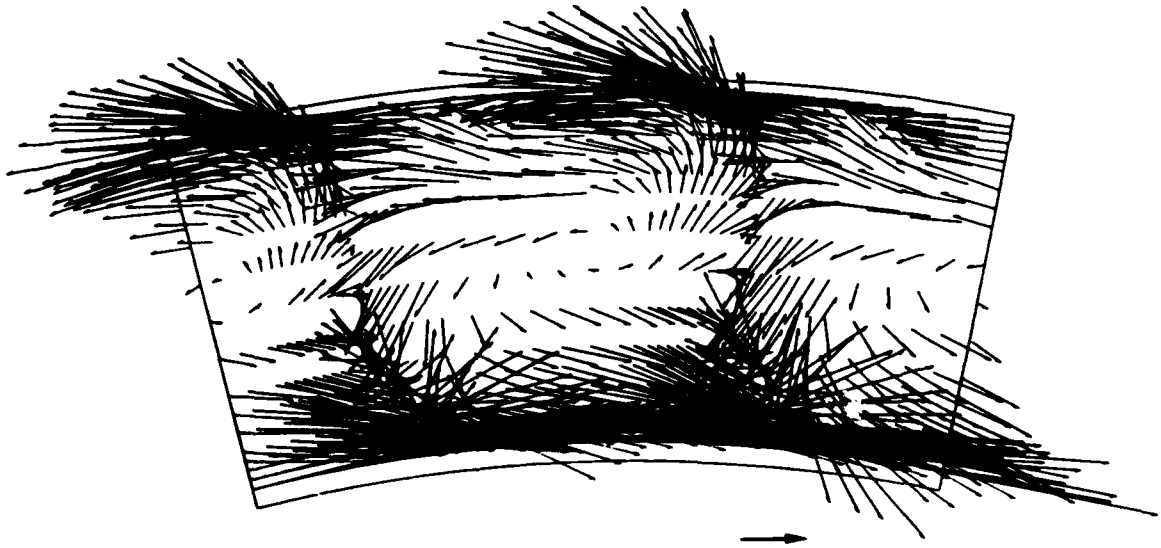

b) SECONDARY FLOW VECTORS $(V/U_m) = 0.1$

Figure 21. Relative Flow Speed Contours and Secondary Flow Vectors Relative to Core Flow, $\bar{\phi}$ = 0.65

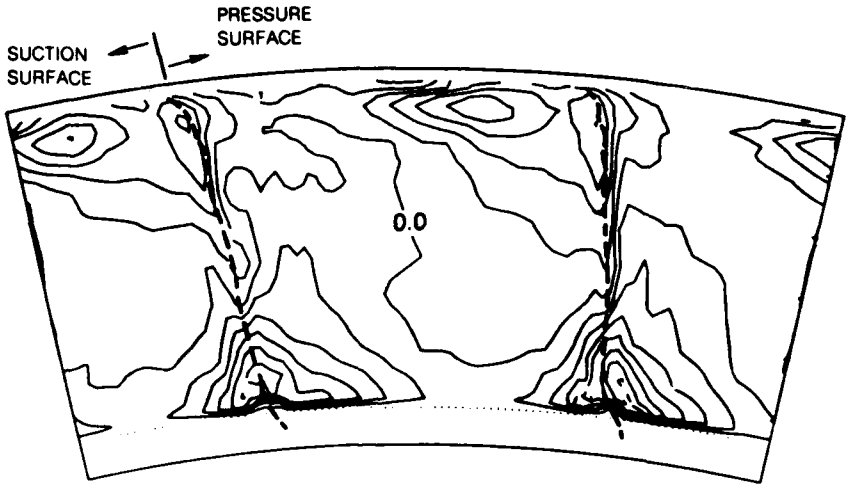

a) PITCH
CONTOUR INCREMENT: $\Delta\phi = 1°$

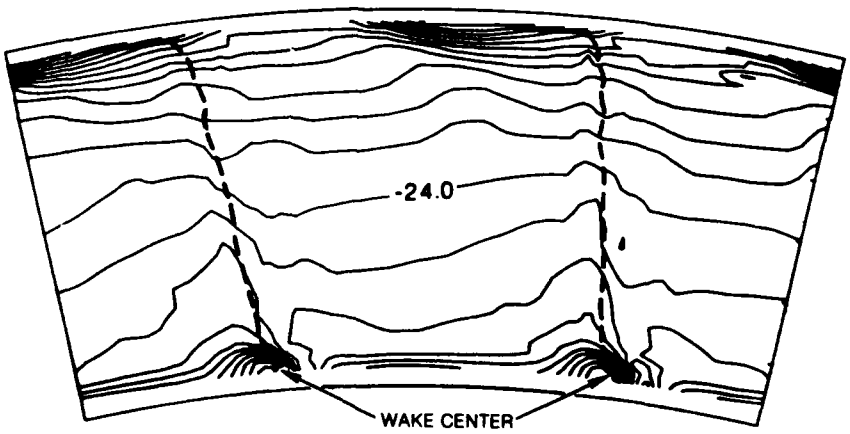

b) YAW
CONTOUR INCREMENT: $\Delta\theta = 2°$

Figure 22. Pitch and Relative Yaw Angle Contours, $\bar{\phi}$ = 0.95

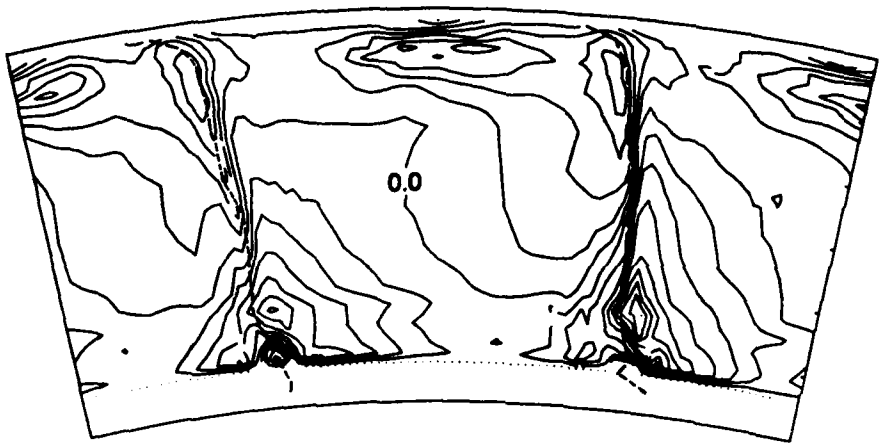

a) PITCH
CONTOUR INCREMENT: $\Delta\phi = 1°$

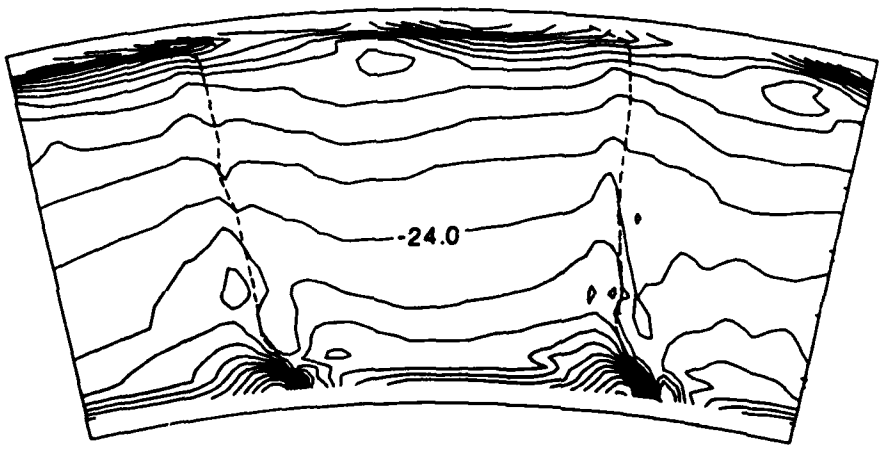

b) YAW
CONTOUR INCREMENT: $\Delta\theta = 2°$

Figure 23. Pitch and Relative Yaw Angle Contours, $\bar{\phi}$ = 0.85

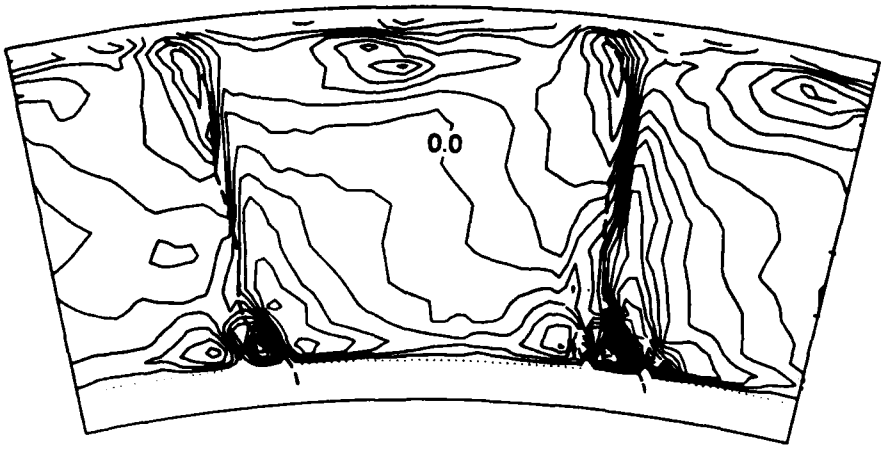

a) PITCH
CONTOUR INCREMENT: $\Delta\phi = 1°$

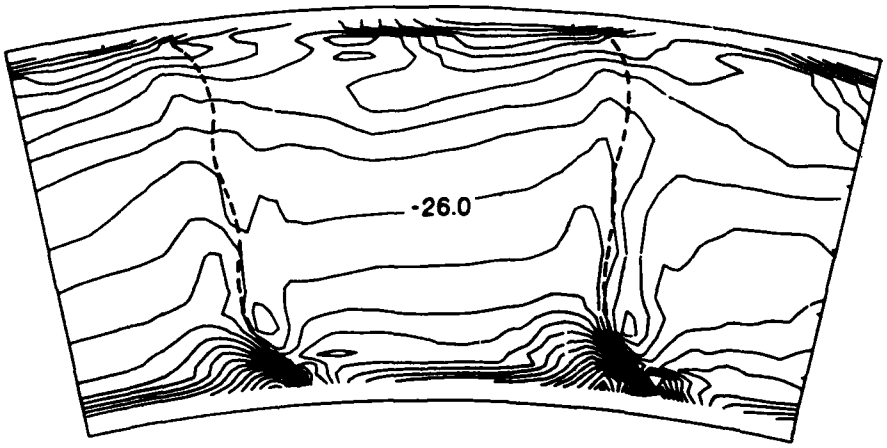

b) YAW
CONTOUR INCREMENT: $\Delta\theta = 2°$

Figure 24. Pitch and Relative Yaw Angle Contours, $\bar{\phi}$ = 0.75

a) PITCH
CONTOUR INCREMENT: $\Delta\phi = 1°$

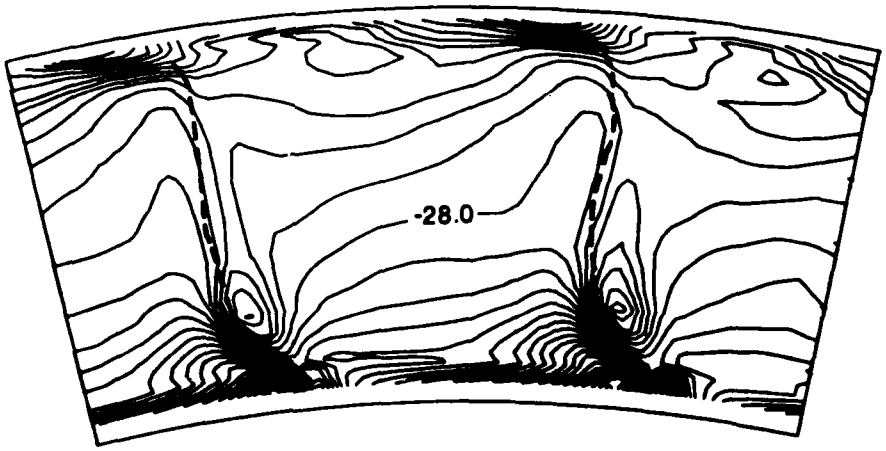

b) YAW
CONTOUR INCREMENT: $\Delta\theta = 2°$

Figure 25. Pitch and Relative Yaw Angle Contours, $\bar{\phi}$ = 0.65

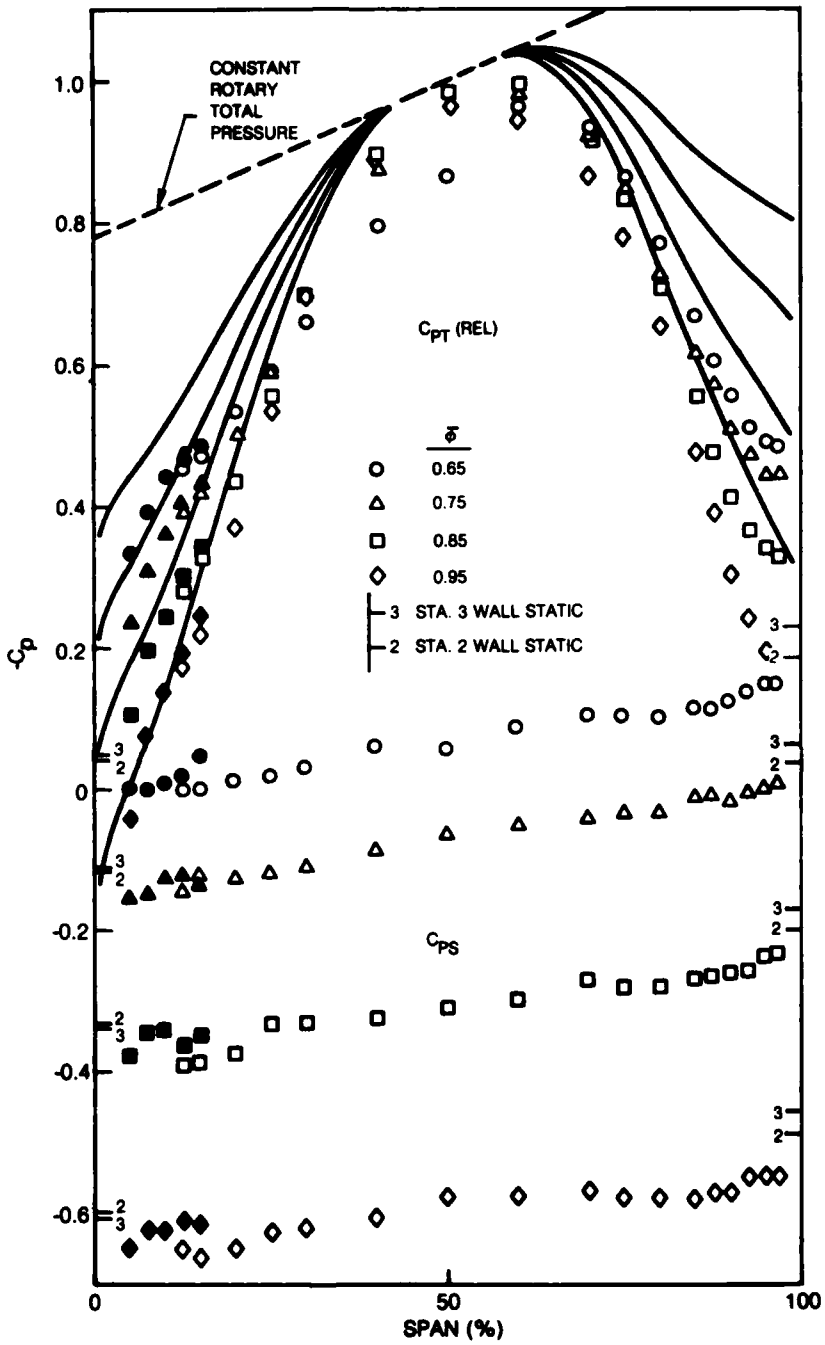

Figure 26. Spanwise Distributions of Relative Total and Static Pressure

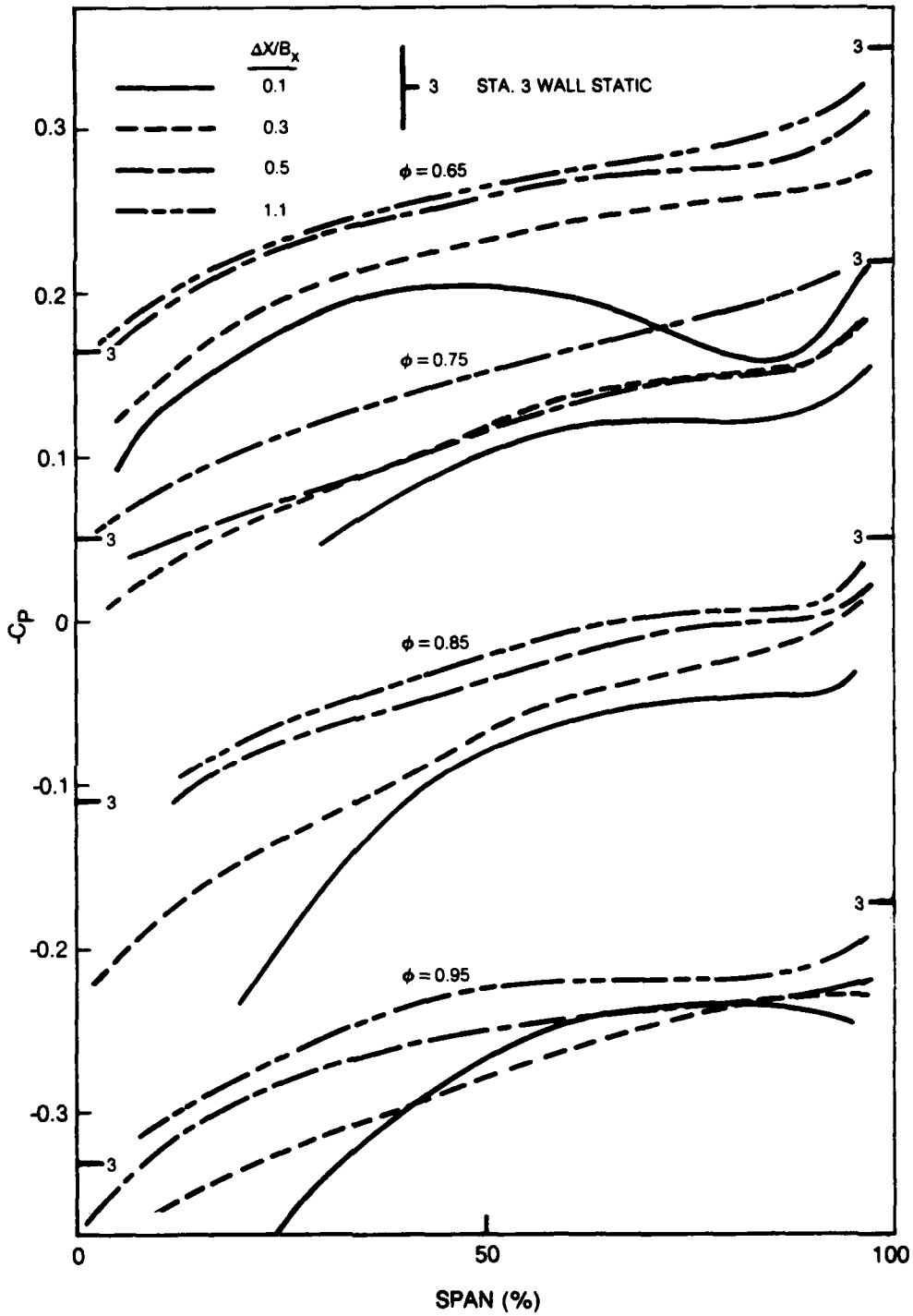

Figure 27. Spanwise Distributions of Static Pressure

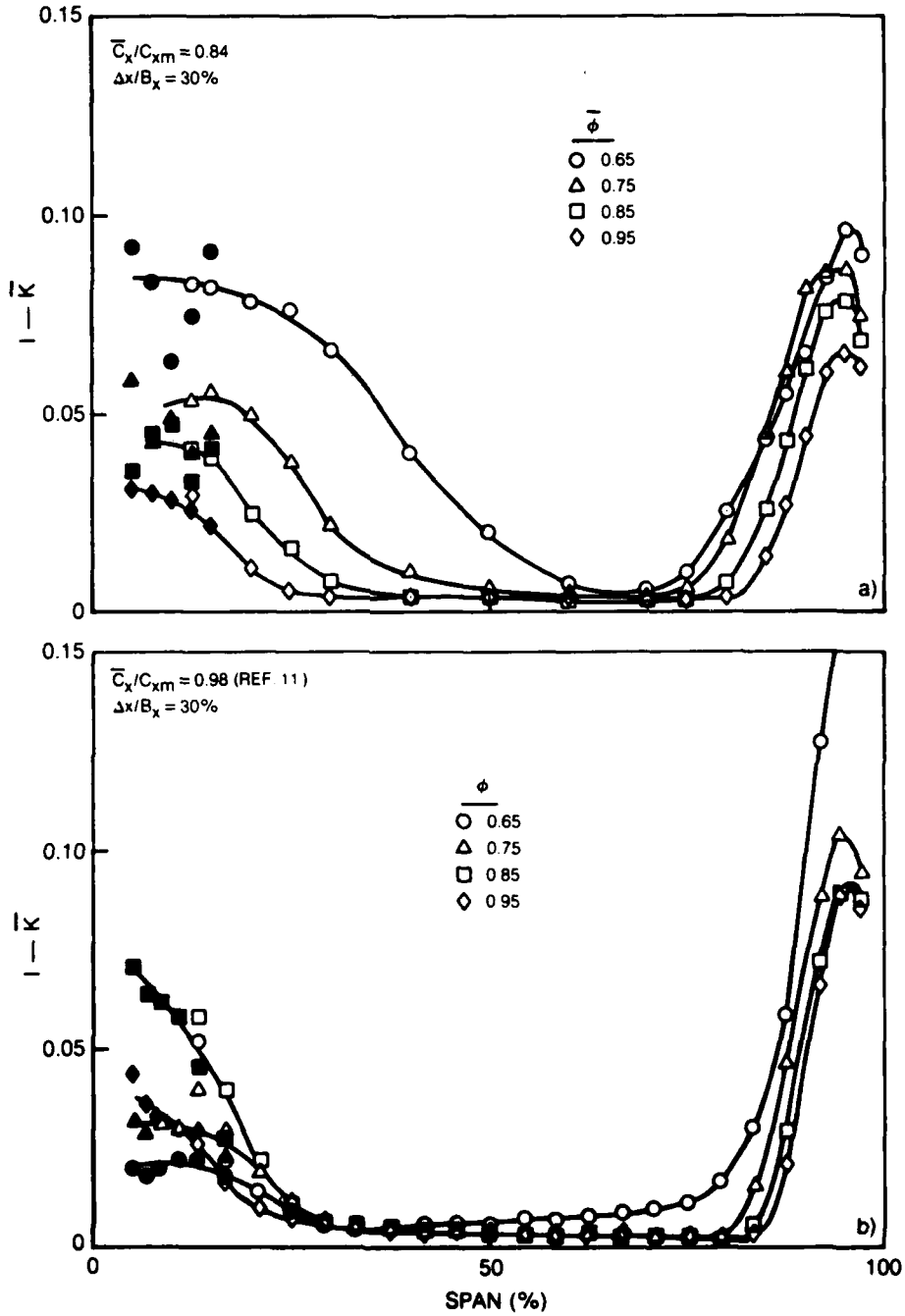

Figure 28. Spanwise Distributions of Blockage

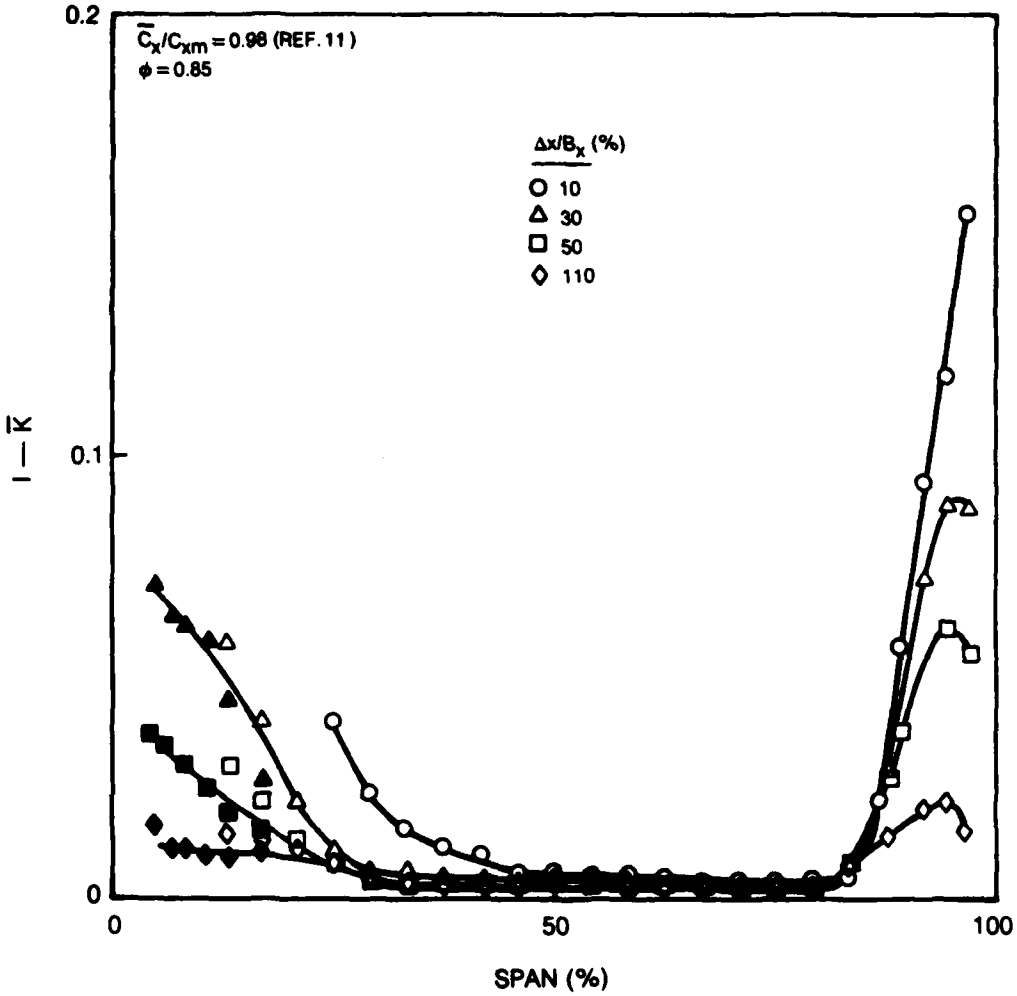

Figure 29. Spanwise Distributions of Blockage, ϕ = 0.85

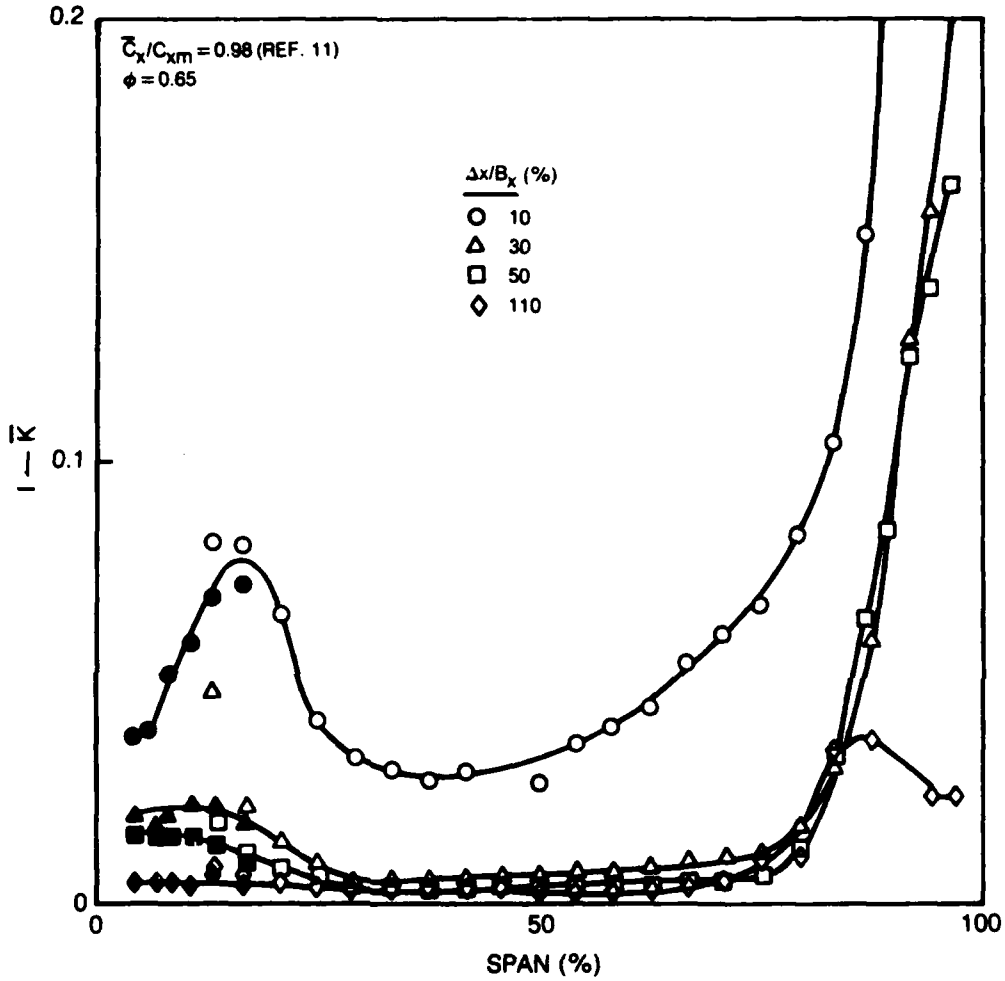

Figure 30. Spanwise Distributions of Blockage, ϕ = 0.65

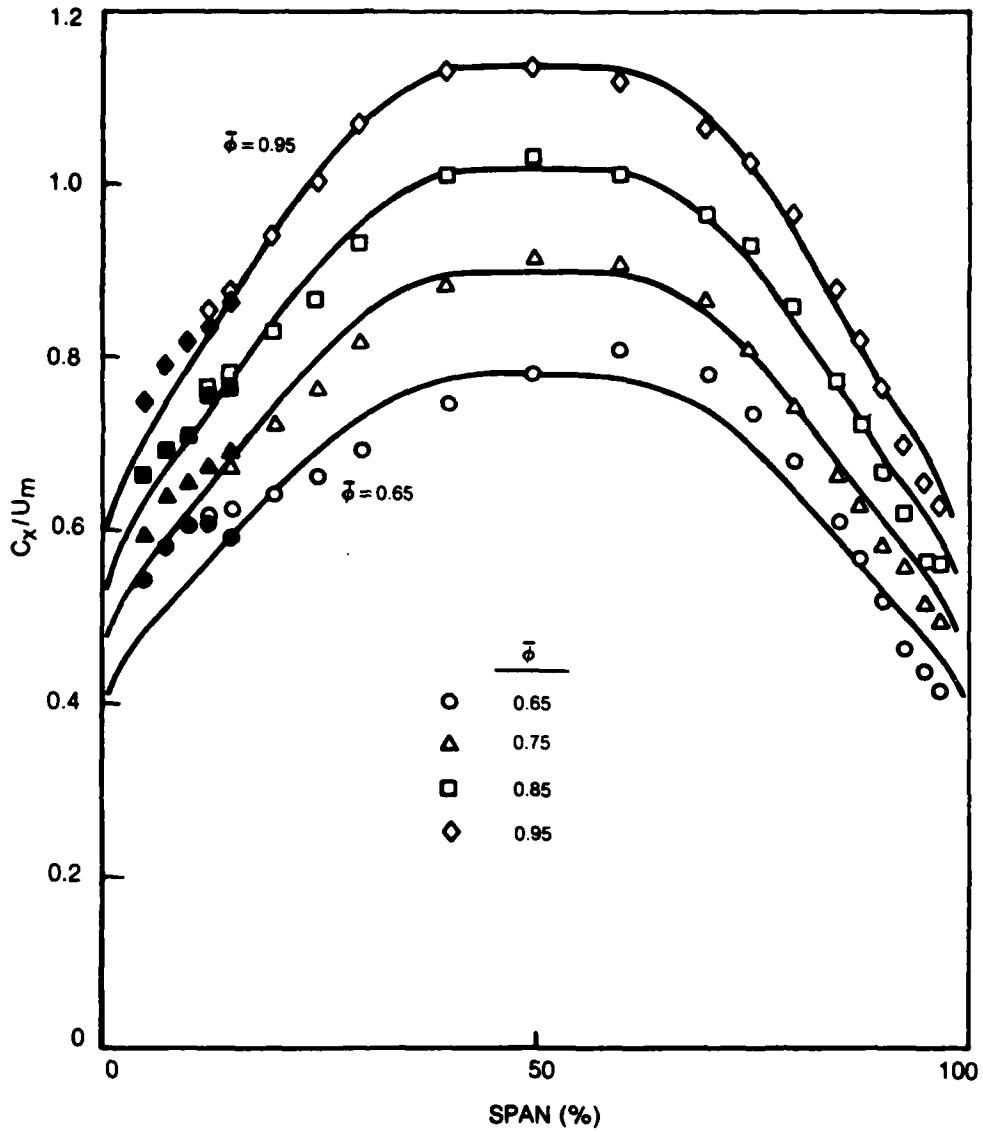

Figure 31. Spanwise Distributions of Axial Flow Speed

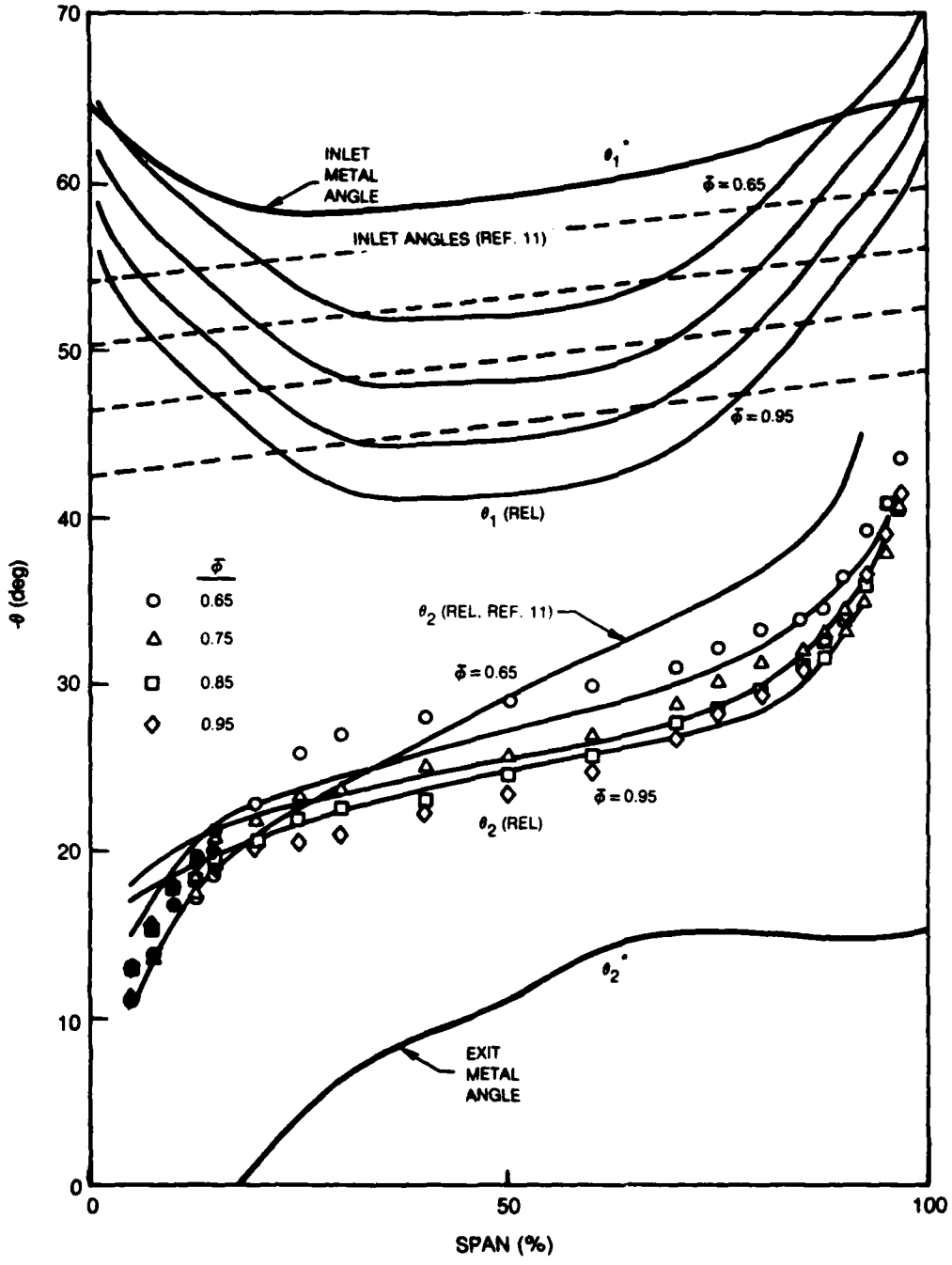

Figure 32. Spanwise Distributions of Inlet and Exit Yaw Angles

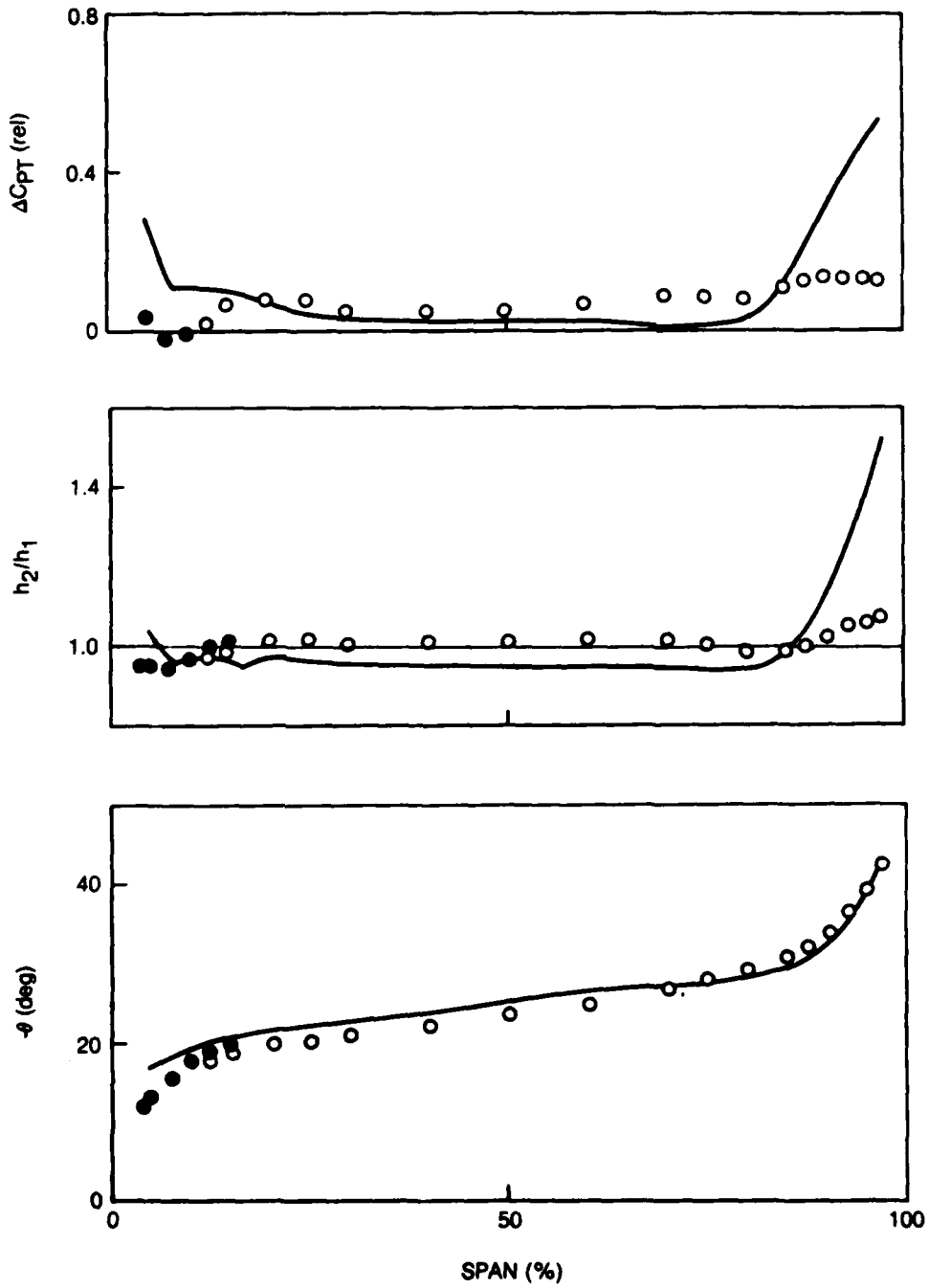

Figure 33. Spanwise Distribution of Loss, Stream Tube Contraction, and Rotor Exit Flow Angle, $\bar{\phi}$ = 0.95

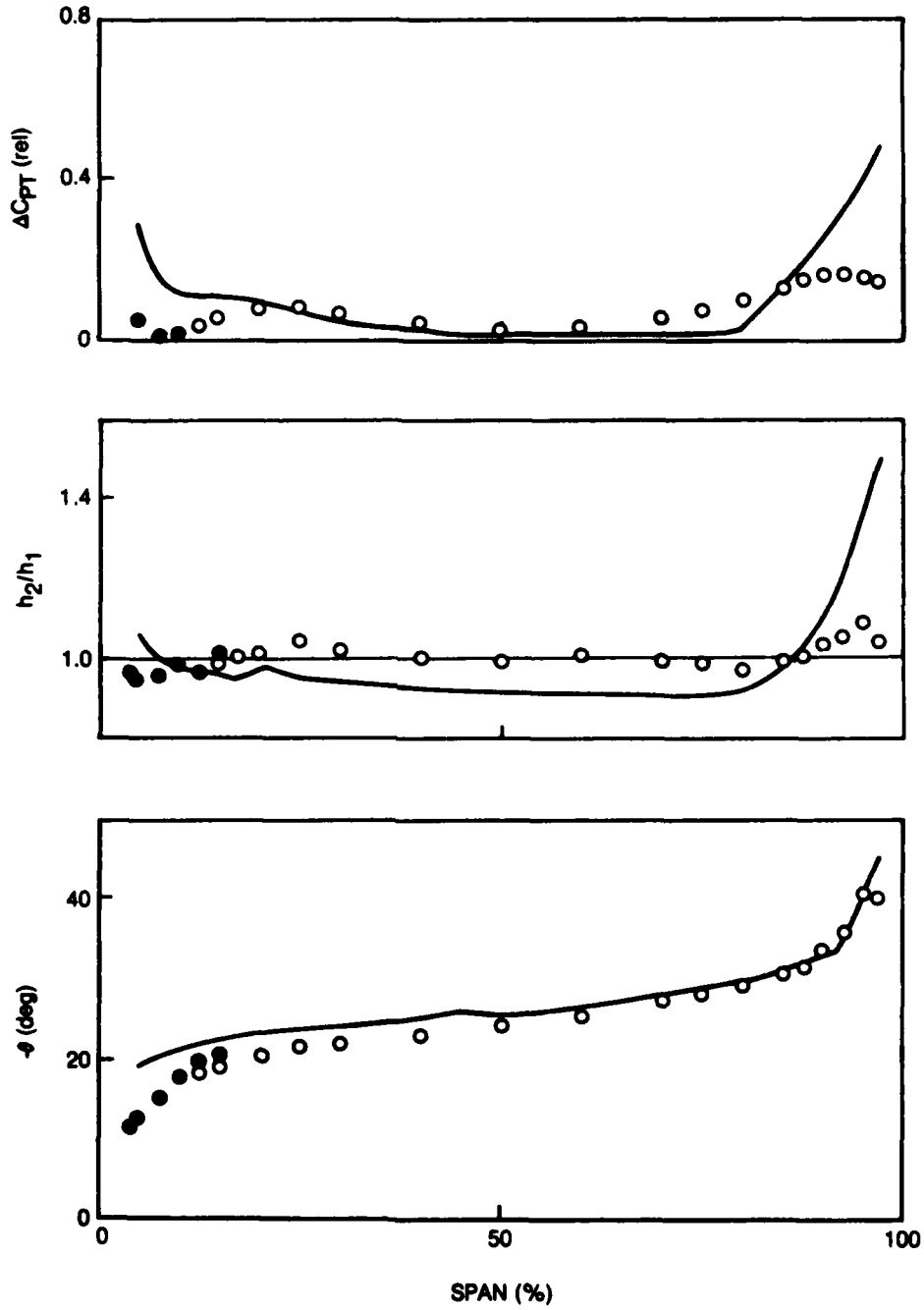

Figure 34. Spanwise Distribution of Loss, Stream Tube Contraction, and Rotor Exit Flow Angle, $\bar{\phi}$ = 0.85

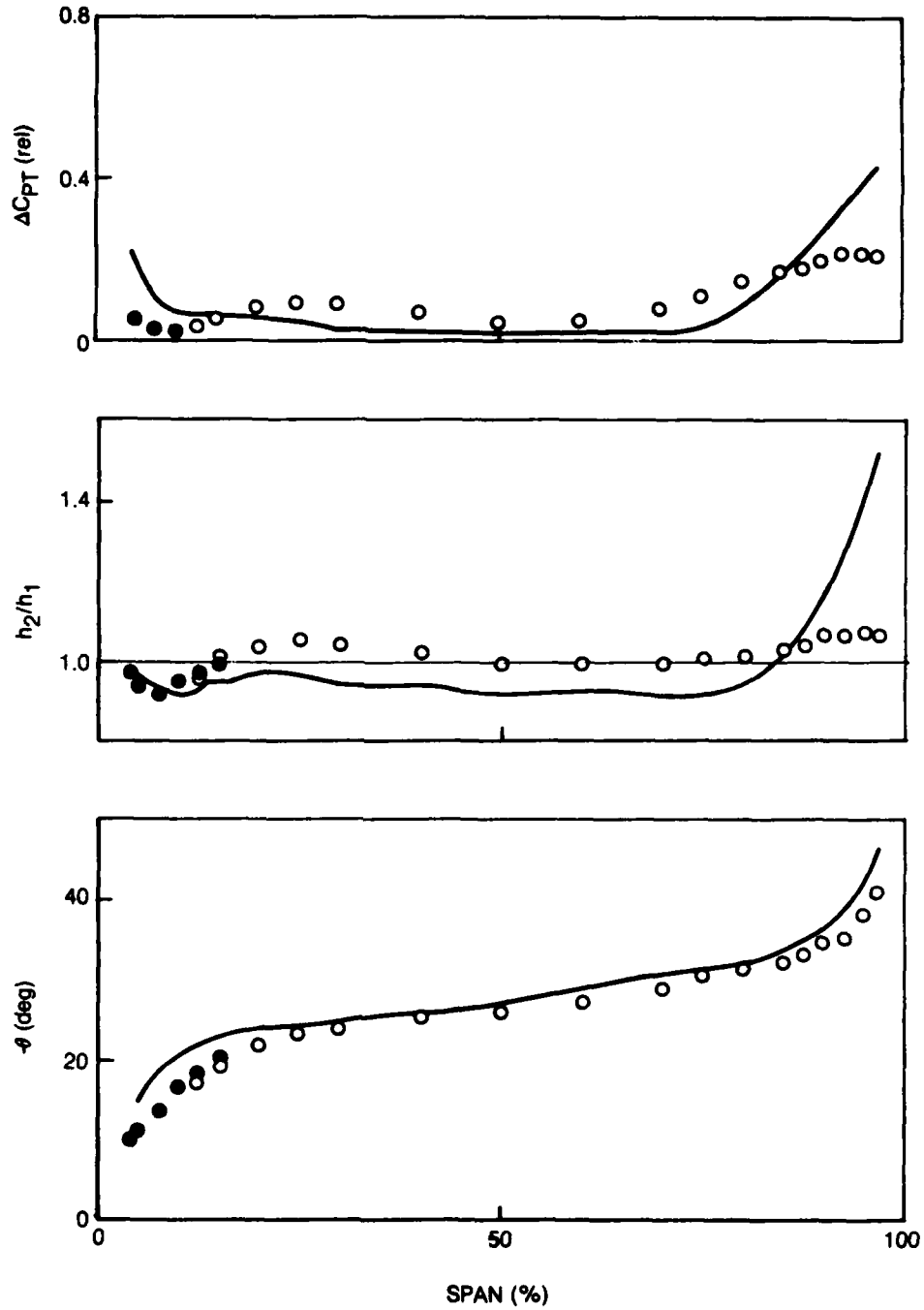

Figure 35. Spanwise Distribution of Loss, Stream Tube Contraction, and Rotor Exit Flow Angle, $\bar{\phi}$ = 0.75

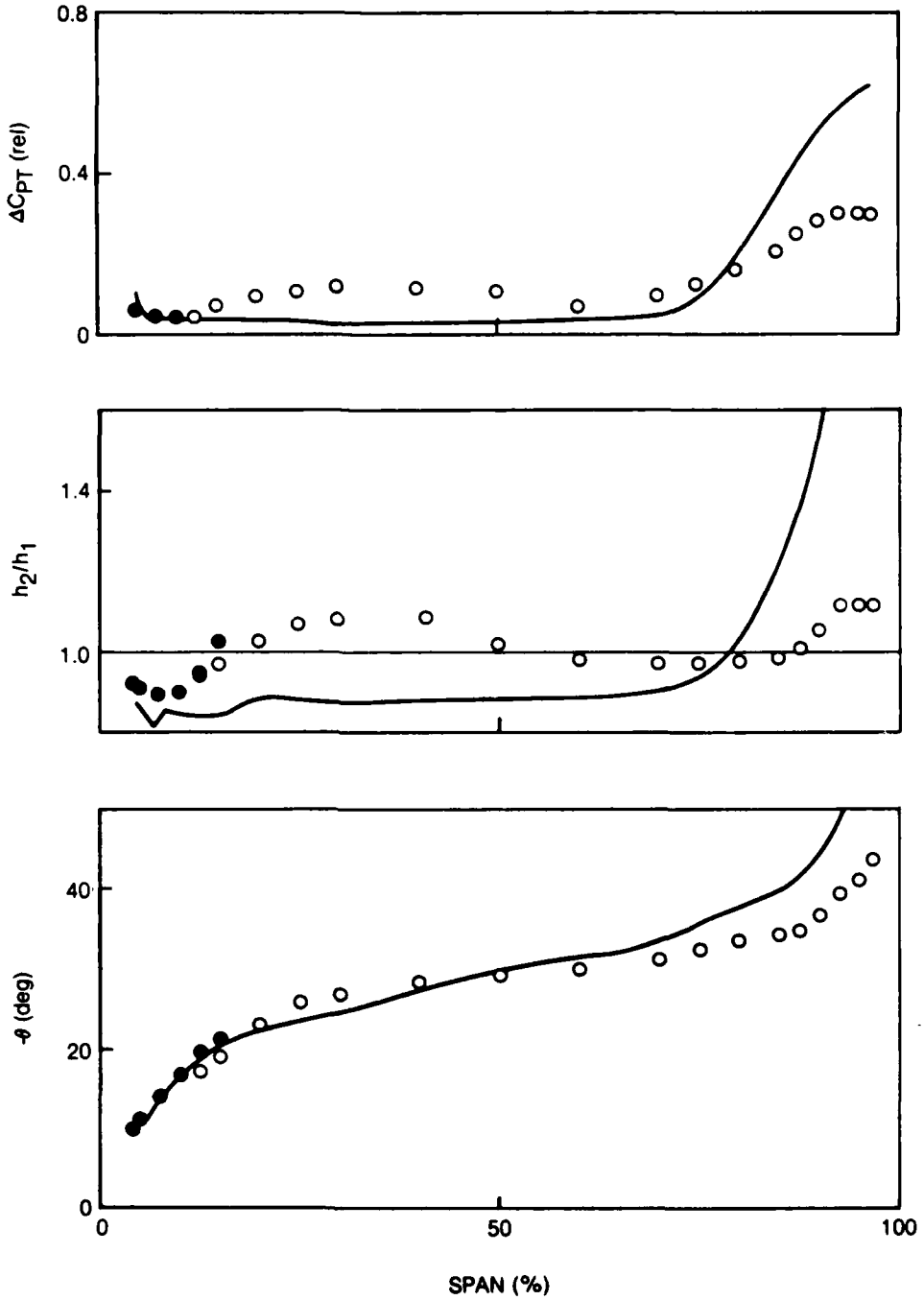

Figure 36. Spanwise Distribution of Loss, Stream Tube Contraction, and Rotor Exit Flow Angle, $\bar{\Phi}$ = 0.65

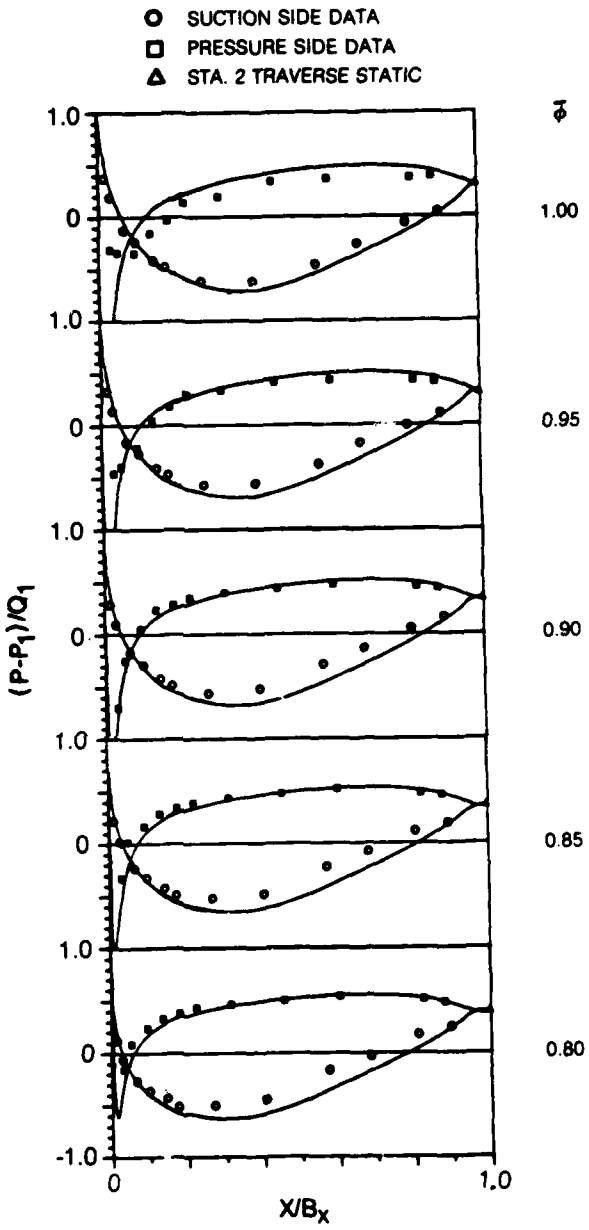

Figure 37. Midspan Airfoil Pressure Distributions

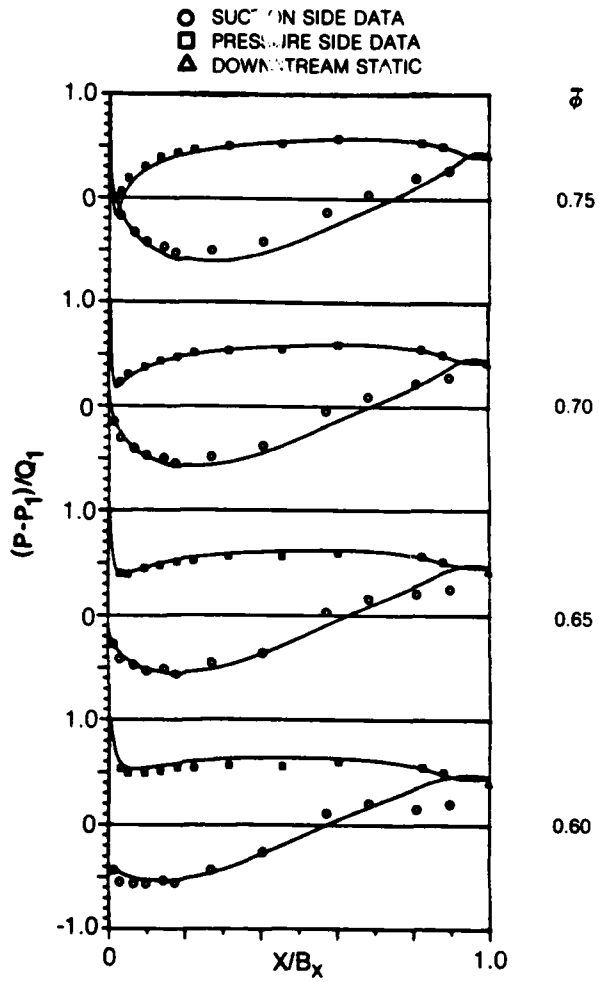

Figure 37. Midspan Airfoil Pressure Distributions

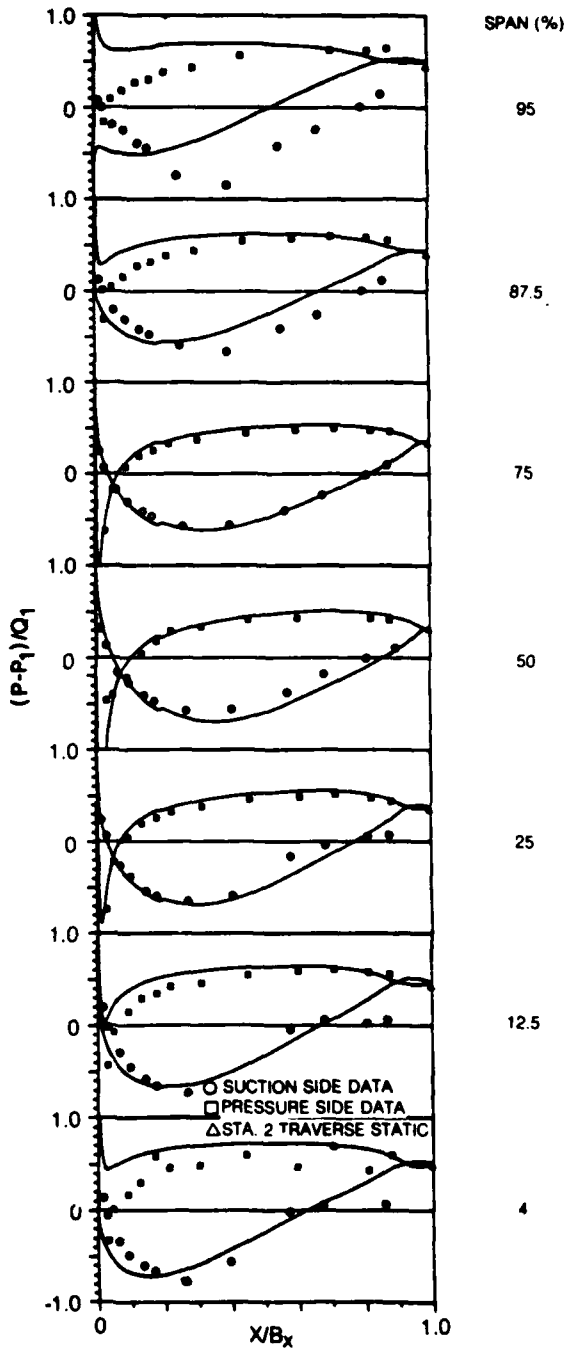

Figure 38. Fullspan Airfoil Pressure Distributions, $\bar{\phi}$ = 0.95

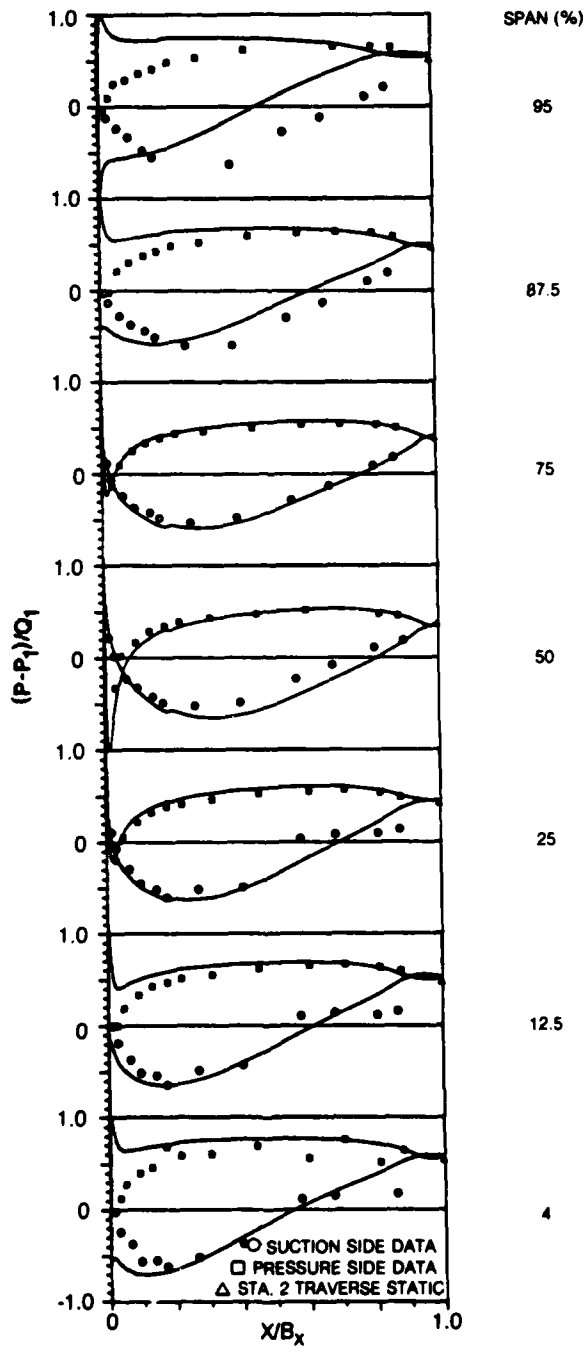

Figure 39. Fullspan Airfoil Pressure Distributions, $\bar{\phi}$ = 0.85

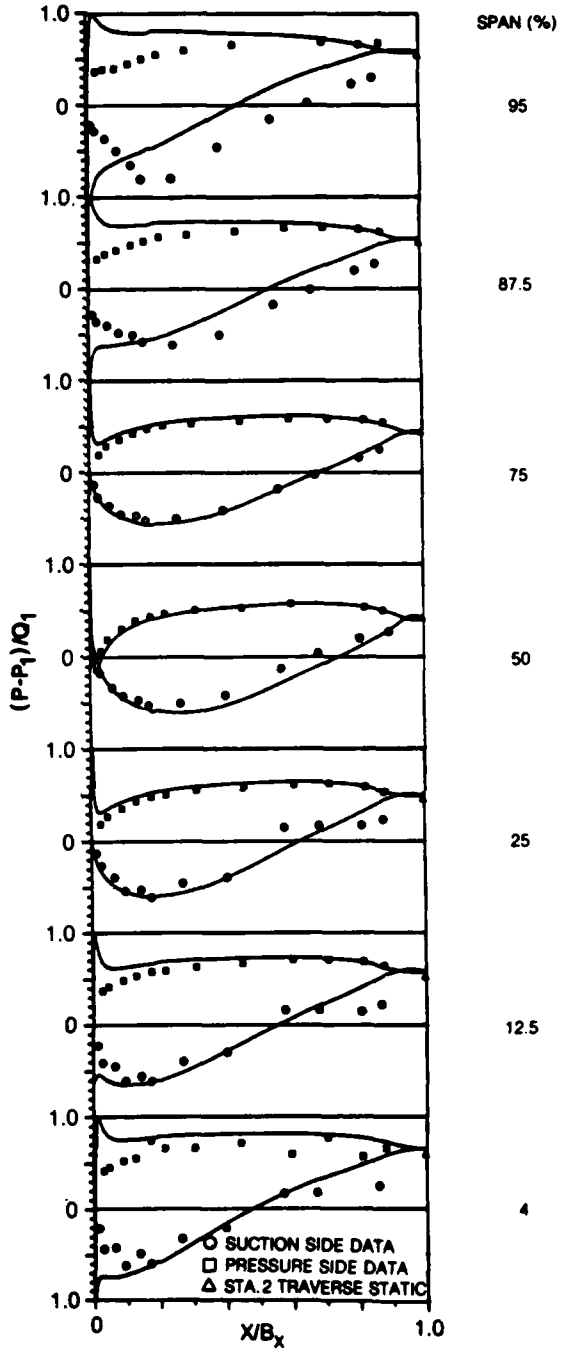

Figure 40. Fullspan Airfoil Pressure Distributions, $\bar{\phi}$ = 0.75

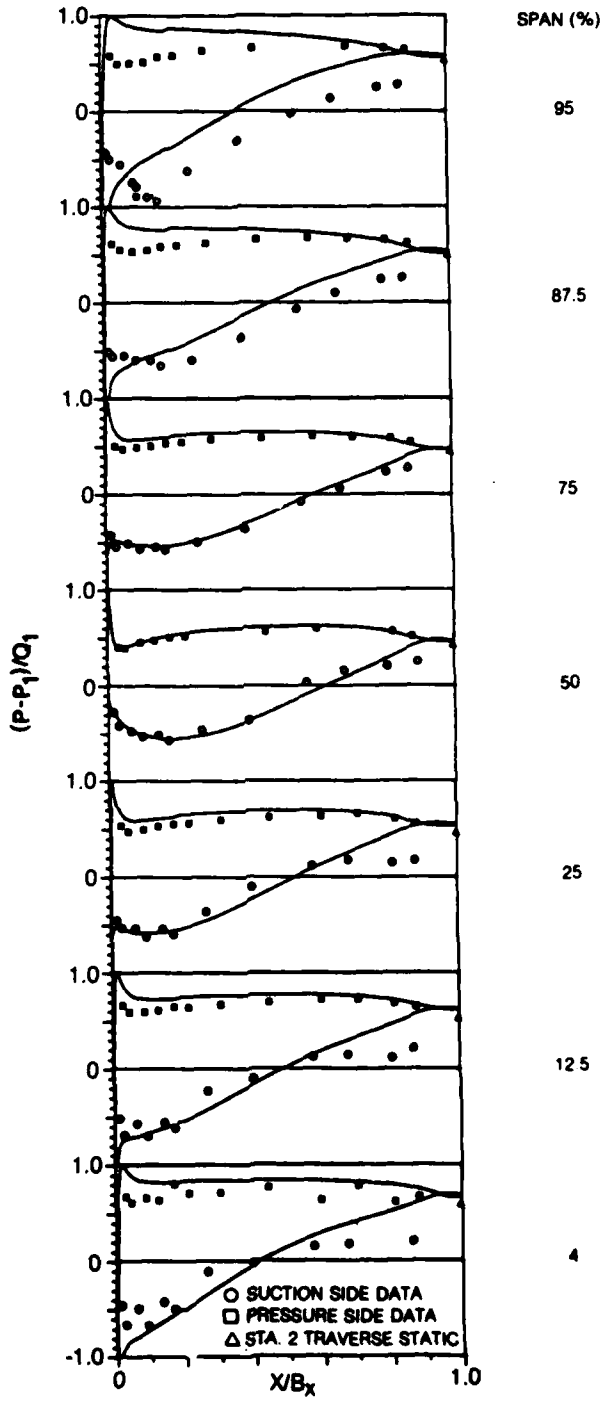

Figure 41. Fullspan Airfoil Pressure Distributions, $\bar{\phi}$ = 0.65

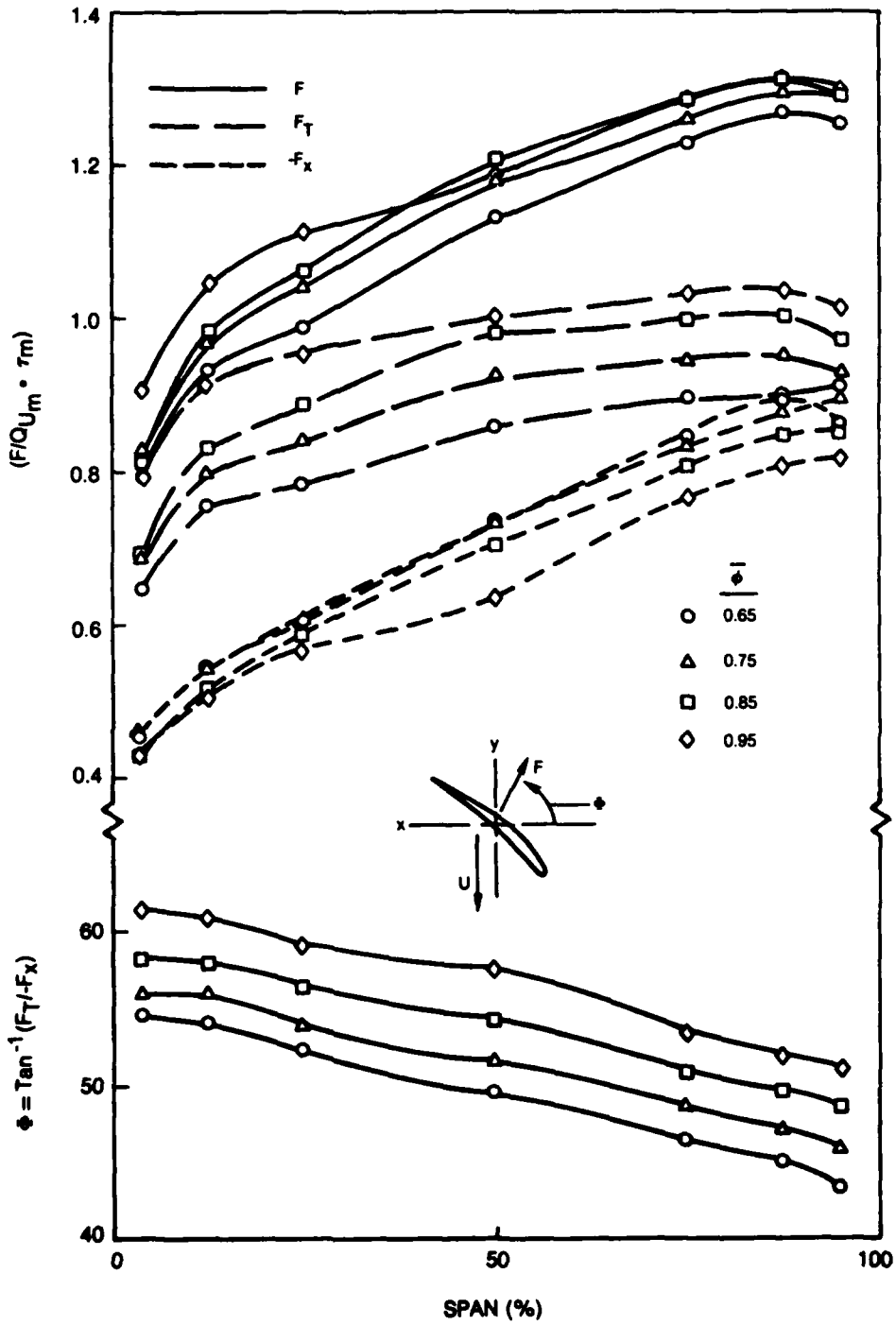

Figure 42. Spanwise Distributions of Rotor Pressure Force

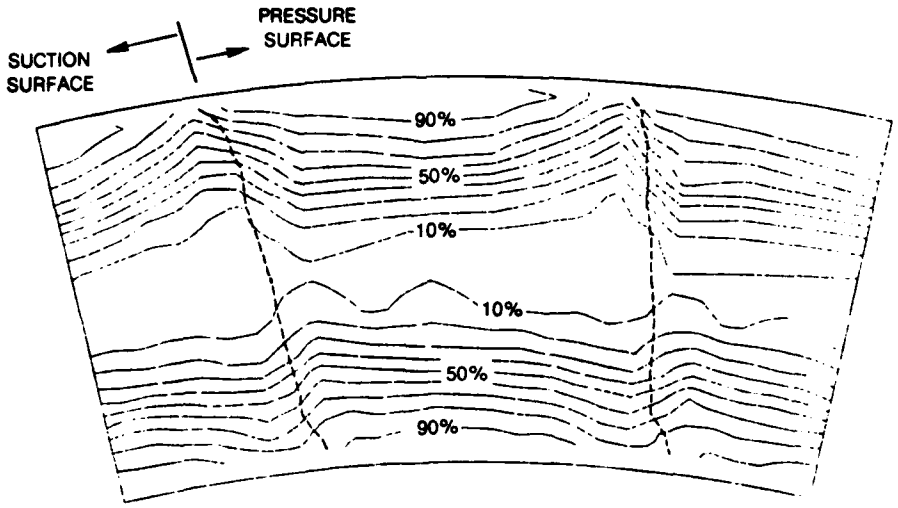

a) TIP AND HUB

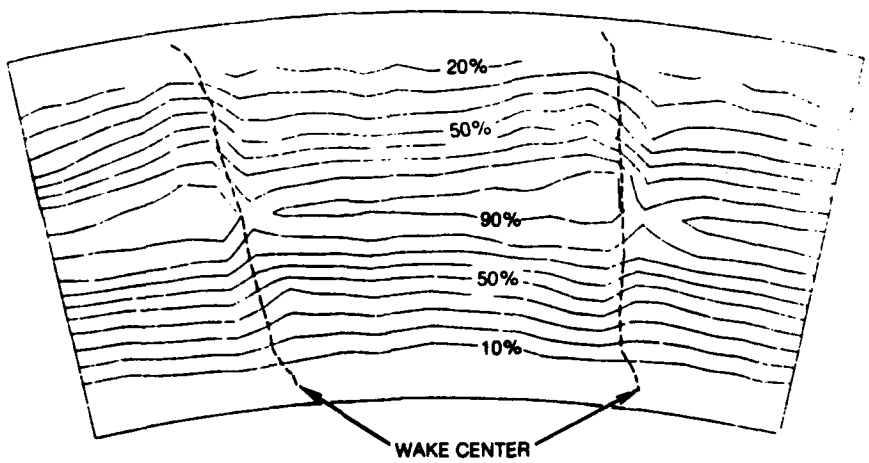

b) MIDSPAN

Figure 43. Trace Gas Concentration Contours, $\bar{\phi}$ = 0.95

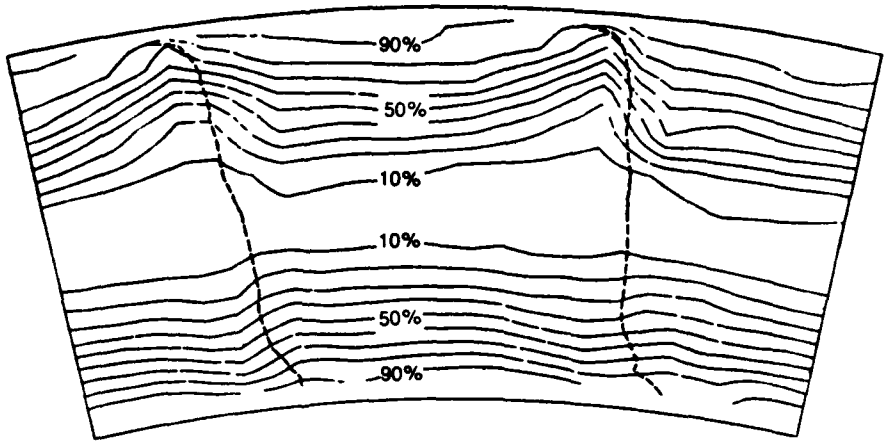

a) TIP AND HUB

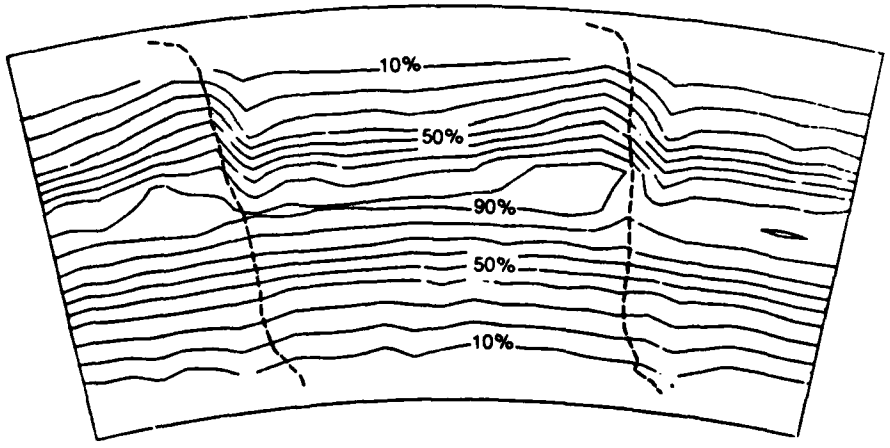

b) MIDSPAN

Figure 44. Trace Gas Concentration Contours, $\bar{\phi}$ = 0.85

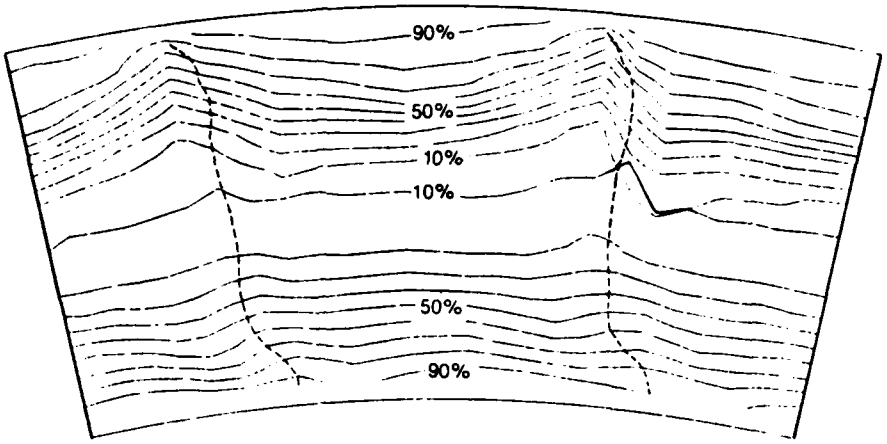

a) TIP AND HUB

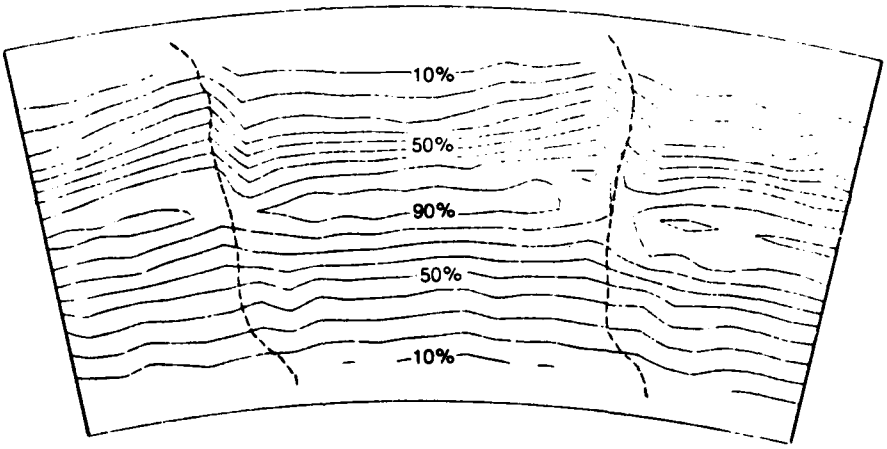

b) MIDSPAN

Figure 45. Trace Gas Concentration Contours, $\bar{\phi}$ = 0.75

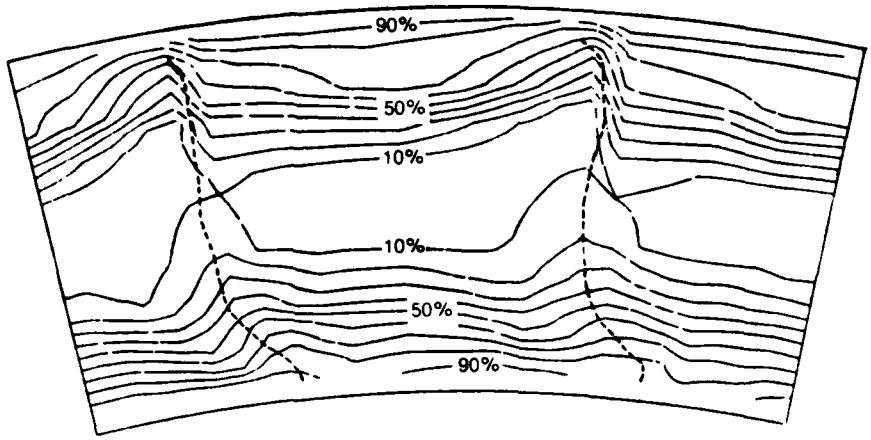

a) TIP AND HUB

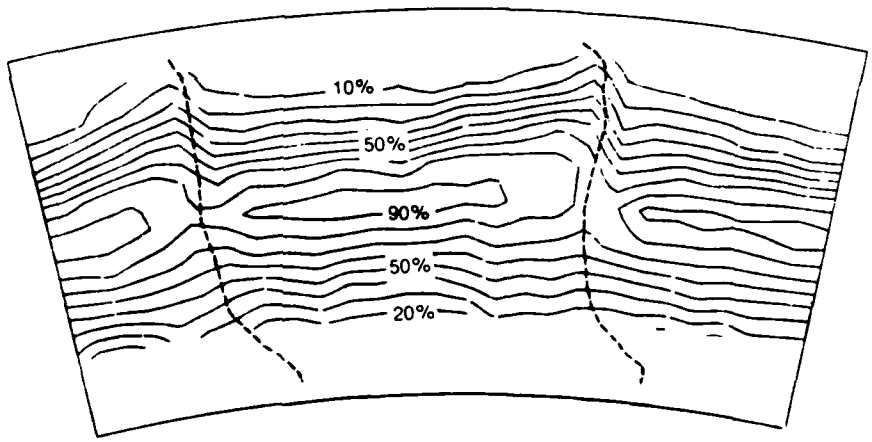

b) MIDSPAN

Figure 46. Trace Gas Concentration Contours, $\bar{\phi}$ = 0.65

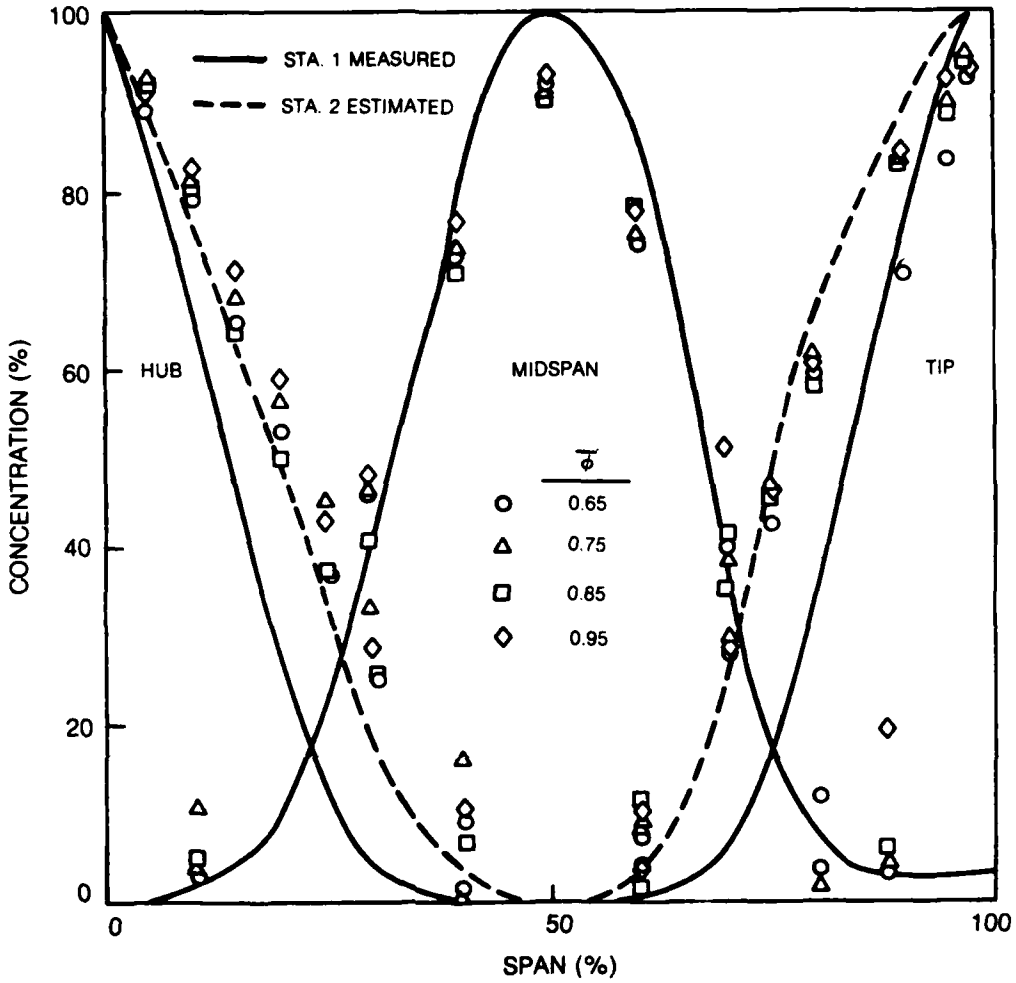

Figure 47. Exit Trace Gas Concentration Profiles at Sta. 2

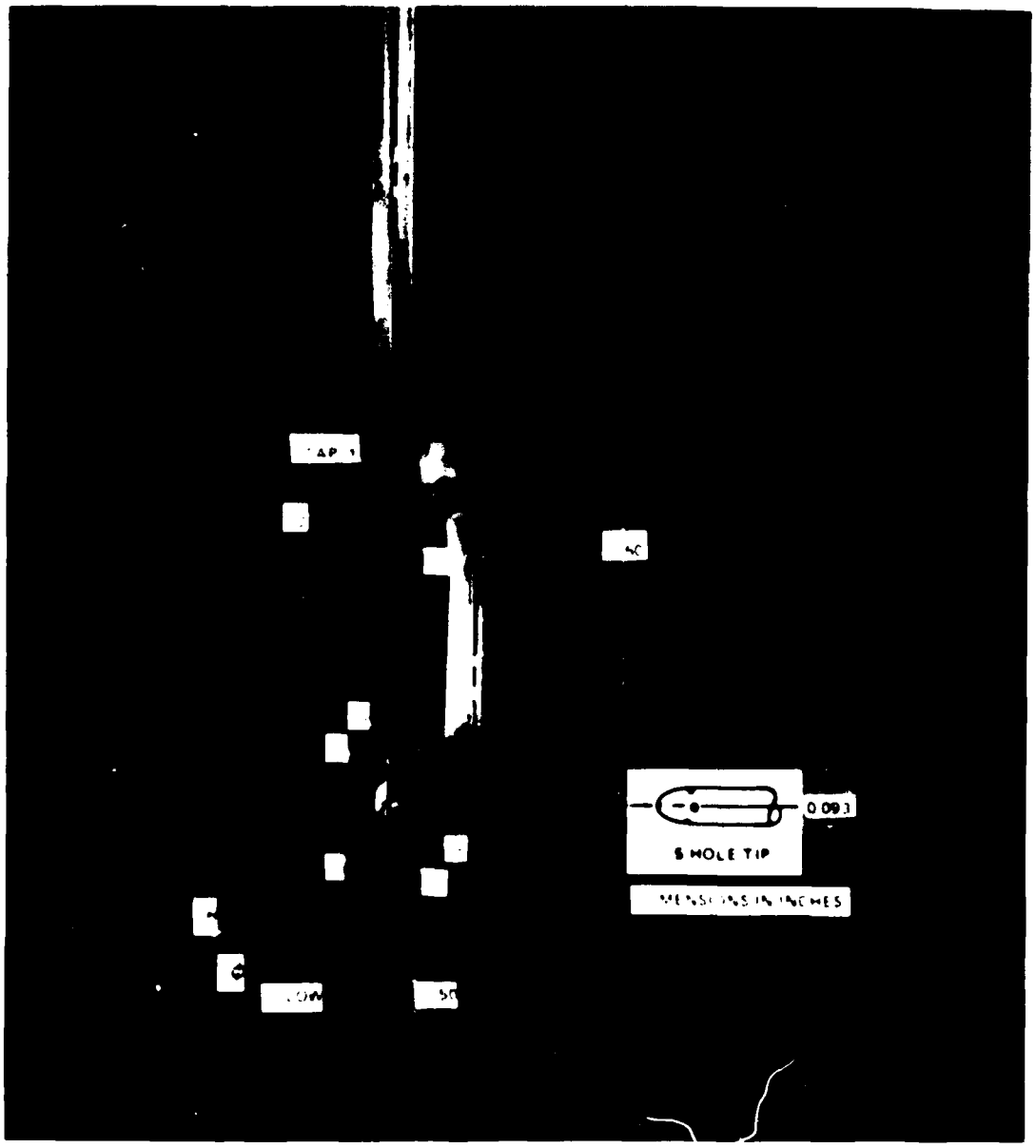

Figure 48. Combination Five Hole/Cobra Probe

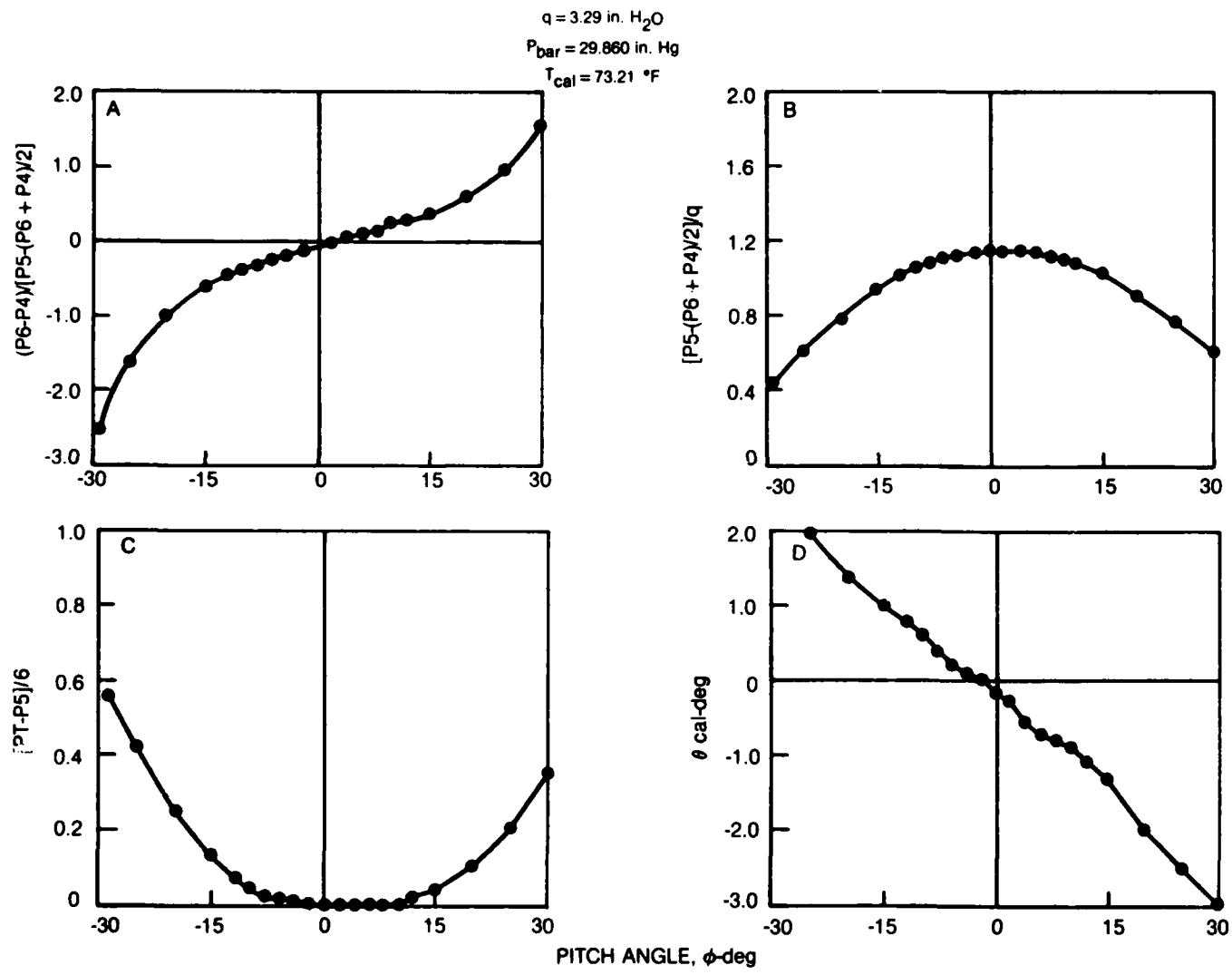

Figure 49. Typical Five Hole Probe Calibration

AD-A130 659 AXIAL COMPRESSOR MIDDLE STAGE SECONDARY FLOW STUDY(U) 2/2
UNITED TECHNOLOGIES RESEARCH CENTER EAST HARTFORD CT
J H WAGNER ET AL. JUL 83 NASA-CR-3701 NAS3-23157

UNCLASSIFIED F/G 21/5 NL

END
DATE
FILMED
DTIC

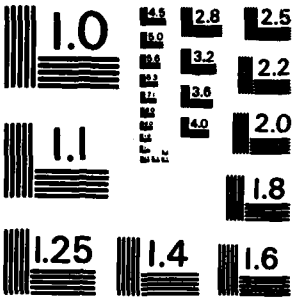

MICROCOPY RESOLUTION TEST CHART
NATIONAL BUREAU OF STANDARDS - 1963 - A

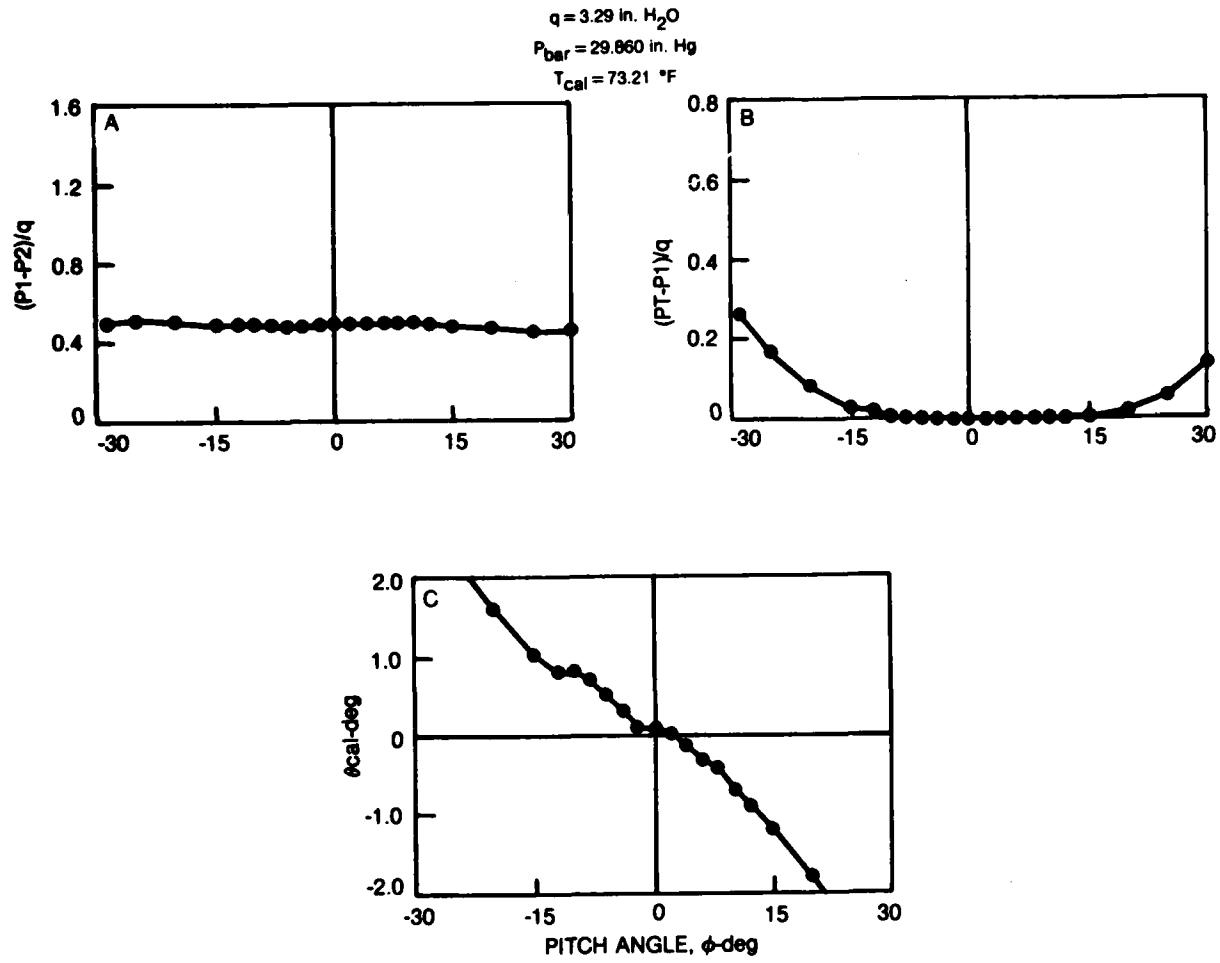

Figure 50. Typical Cobra Probe Calibration

1. Report No.	2. Government Accession No.	3. Recipient's Catalog No.
NASA CR-3701		

4. Title and Subtitle	5. Report Date
Axial Compressor Middle Stage Secondary Flow Study	July 1983
	6. Performing Organization Code
7. Author(s)	8. Performing Organization Report No.
Joel H. Wagner, Robert P. Dring, and H. David Joslyn	None
9. Performing Organization Name and Address	10. Work Unit No.
United Technologies Research Center Silver Lane East Hartford, CT 06108	11. Contract or Grant No. NAS3-23157
12. Sponsoring Agency Name and Address	13. Type of Report and Period Covered
U.S. Army Research & Technology Laboratories (AVRADCOM), Propulsion Laboratory, Lewis Research Center, Cleveland, Ohio 44135 and NASA Lewis Research Center, Cleveland, Ohio 44135	Contractor Report
	14. Sponsoring Agency Code 505-32-33 (E-1678) 1L162209AH76

15. Supplementary Notes

Final report. Project Manager, Michael J. Pierzga, U.S. Army Research and Technology Laboratories (AVRADCOM), Propulsion Laboratory, Lewis Research Center, Cleveland, Ohio 44135.

Abstract

This report describes an experimental investigation of the secondary flow within and aft of an axial compressor model with thick endwall boundary layers. The objective ~~of the study~~ was to obtain detailed aerodynamic and trace gas concentration traverse data aft of a well documented isolated rotor for the ultimate purpose of improving the design phases of compressor development based on an improved physical understanding of secondary flow. It was determined from the flow visualization, aerodynamic, and trace gas concentration results that the relative unloading of the midspan region of the airfoil inhibited a fullspan separation at high loading, preventing the massive radial displacement of the hub corner stall to the tip. Radial distribution of high and low total pressure fluid influenced the magnitude of the spanwise distribution of loss, such that, there was a general decrease in loss near the hub to the extent that, for the least loaded case, a negative loss (increase in total pressure) was observed. The ability to determine the spanwise distribution of blockage was demonstrated. Large blockage was present in the endwall regions due to the corner stall and tip leakage with little blockage in the core flow region. Hub blockage was found to increase rapidly with loading.

17. Key Words (Suggested by Author(s))	18. Distribution Statement
Axial compressors Secondary flow Blockage	Unclassified - unlimited STAR Category 02

19. Security Classif. (of this report)	20. Security Classif. (of this page)	21. No. of Pages	22. Price*
Unclassified	Unclassified	97	A05

* For sale by the National Technical Information Service, Springfield, Virginia 22161

NASA-Langley, 1983

96

END

DATE
FILMED

8 — 83

DTIC